

CHAPTER 1

INTRODUCTION

Piezoelectric ceramics have become an important functional material in micro-electro mechanical systems (MEMS). Quartz is widely used as a piezoelectric material for resonators and sensors [Eer01]. Lead zirconate titanate ($\text{Pb}(\text{Zr},\text{Ti})\text{O}_3$ or PZT) is used for actuation because of its favorable piezoelectric properties and electromechanical coupling coefficients. Microsystems that are based on the ability of PZT to convert electrical energy to mechanical vibrations, and vice-versa, include scanning mirror drives [Asa03], micro-optic devices [Val95, Lin94, Mot94], micro-mixers [Yan00], accelerometers [Yu01], micro-surgery equipment [Ume06, Ezh06] and scanning microscopy probes [Cun94]. This work explores the possibility of using PZT as a material for micro-heaters and its application to biological tissue cauterization. Section 1.1 describes the role of microheaters in microsystems. Section 1.2 provides an introduction to ultrasonic heating and its present applications. Different methods of ultrasound generation are discussed in Section 1.3. Section 1.4 discusses the heat generation in piezoelectric materials and possible advantages of it. Section 1.5 provides the motivation and background for the two applications targeted in this work: cauterization of the needle tract during biopsy procedures and microthermal stimulation for locomotion control in insects. The research challenges addressed in this work are listed in Section 1.6.

1.1. Role of microheaters in microsystems

Microheaters have been widely used as part of sensors and actuators in numerous microsystems. In thermal flow sensors, microheaters are used to heat a thermally isolated region [Tie97, Joh87, Put74, Tab85, Tan86, Qiu95, Tai88]. The cooling caused by the flow is measured using a temperature sensor. The temperature difference measured by the sensor is then used to determine the flow rate and direction.

Microheaters have been used in Pirani sensors for pressure measurements [Lec98, Vol07, Mas91a, Kla97, Bar04, Afr02, Zha06]. The thermal conductivity of the gas depends on the pressure. The pressure is determined by measuring the changes in the thermal isolation of a suspended heater.

Microheaters have also been used for acceleration measurements. Leung *et al.* fabricated a micromachined accelerometer which used a bubble of heated gas as the proof mass [Leu97]. The gas was heated using an on-chip heater. The movement of the bubble due to acceleration was measured using two temperature sensors placed on either side of the heater.

Microheaters are used in gas detector systems [Tia03, Hwa11] to elevate the temperature of the sensing layer, which, in turn, allows for gas chemical reactions to occur in the sensing layer. The sensitivity and response time of the gas sensors are highly dependent on the operating temperature. Hence, microheaters are used to generate uniform and stable temperature throughout the sensing layer.

Microheaters are also used in thermal actuators. Most of these actuators generate displacement from thermal expansion of a beam. The two most common types of actuators are bimorph actuators and bent beam actuators [Wei08, Que01]. The thermal

expansion mismatch between two different materials generates displacement in bimorph actuators. The bent beam actuators generate displacement because of the thermal expansion of a single material beam. These actuators have been used in telerobotics [Suh97], micropositioning [Ata93], thermal micro-relays [Sek97], and rotary microengines [Heo07]. Microheaters have also been used as part of microfluidic systems for assays [Bas07, Shi03, Hen05], chemical reactors [Dem06] and micro-incandescent lamps [Mas91b].

Conventionally, microheaters have used joule heating in thin film resistors that are fabricated from metals or doped semiconductors [Chu04, Ara06, Kim92]. While this is effective and easily implemented, joule heating can present challenges with parasitic heating of leads, particularly as the magnitude of the resistor decreases. Efforts have been directed at developing heaters with high efficiency and low response time. This has resulted in the investigation of different materials for heating elements. For example, the moderate heat conductivity of TiN (15 W/m.K) lowers the conductive losses through the connecting wires, thereby improving efficiency [Cre05]. Microheaters based on a conductive composite of silver microparticles embedded in polydimethylsiloxane (PDMS) have also been reported [Liu06].

1.2. Ultrasonic heat generation

When ultrasound waves travel in a medium, vibrations are dissipated by internal damping of the medium. This dissipated energy results in heating of the absorbing medium. Ultrasound has been used widely in the field of medicine for non-invasive heating of biological tissue for hyperthermia and hemostasis. Fry *et al.* [Fry55, Fry60]

has reported the use of high intensity focused ultrasound (HIFU) for cauterization during brain surgery. Tissue heating by HIFU has been extensively tested and clinically used for treatment of tumors (hyperthermia). In this technique, the temperature of the targeted region is raised to 50-55°C for 1-2 minutes to kill the tumor cells [Bil90, Ko196]. Also, thermal exposure to a temperature of 42-45°C for 30-60 minutes sensitizes the cells to radiation and chemotherapy [Dut90, Ove96]. Ultrasonic interstitial and intracavitary probes [Die90, Lee99] have been developed for more localized heating of targeted tissue. Ultrasonic heating has also been used in treatment of glaucoma and cardiac arrhythmias [Col85, Zim95].

In addition to medical applications discussed above, ultrasonic heating has been used for welding of thermoplastics [Tsu85]. There have also been efforts at developing cooking apparatus based on ultrasonic energy [Ene72]. The next section discusses the common methods of ultrasound generation.

1.3. Ultrasound generation methods

1.3.1 Laser ultrasonics

Laser ultrasonic systems provide a non-contact method to generate ultrasonic waves. The lasers used for ultrasound generation are short pulse – from tens of nanoseconds to femtoseconds – and high power lasers such as solid state Q-switched Nd:YAG and CO₂ gas lasers [Web01]. Ultrasound waves are generated by either thermoelastic expansion or ablation. In the thermoelastic regime, the ultrasound is generated by sudden thermal expansion caused by localized heating of the material surface. In the ablation regime, ultrasound generation is caused by the expansion of the

plasma produced above the material surface. The frequency of the generated ultrasound depends on the frequency of the laser pulses. Femtosecond lasers are used for high frequency ultrasound generation (up to 100 GHz).

1.3.2 *Electromagnetic acoustic transducers (EMATs)*

Another method of ultrasound generation is the use of electromagnetic acoustic transducers (EMATs) (Fig. 1.1) [Web02]. When a wire carrying current at the desired ultrasonic frequency is placed near the surface of a conductor, eddy currents are induced in the region near the surface of the conductor. In the presence of a static magnetic field, these eddy currents experience a Lorentz force given by:

$$F = J \times H \quad (1.1)$$

where F is the body force per unit volume, J is the induced current density, and H is the static magnetic field. This results in ultrasound generation at the frequency of the current flowing through the wire. EMATs do not require any couplant for ultrasound generation. This provides a non-contact method for ultrasound generation at elevated temperatures and in remote locations. However, it has very low efficiency.

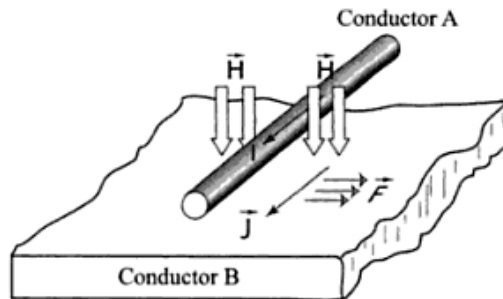


Figure 1.1: Schematic of an elementary EMAT [Shu02].

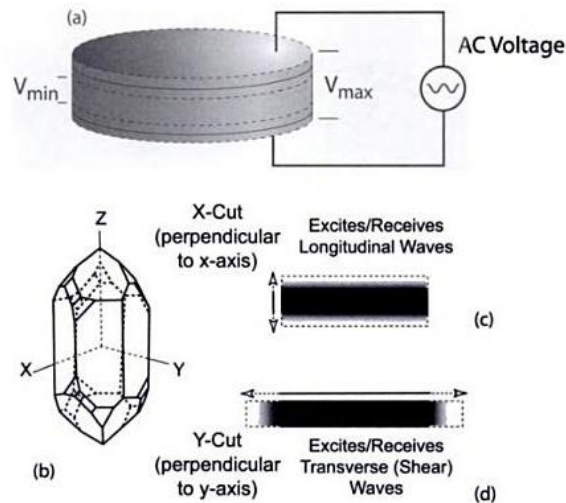


Figure 1.2: Response of a piezoelectric disk to an alternating voltage. (a) Piezoelectric crystal, (b) axis definition and (c) X cut vibrations are longitudinal and (d) Y- cut vibrations are transverse. [Shu02].

1.3.3 Piezoelectric transducers

The most common ultrasound generation technique uses piezoelectric transducers [Web03]. These transducers consist of a piezoelectric ceramic, which is cut into various shapes to produce different wave modes (Fig. 1.2). Before the development of piezoelectric ceramics, quartz crystals and magnetostrictive materials were used. Piezoelectric ceramics have become the dominant material for transducers because of good piezoelectric properties and ease of manufacturing various shapes and sizes. Piezoelectric ceramics also require low drive voltages and can be used up to 300°C . The operating frequency of the piezoelectric devices depends on the thickness of the piezoelectric element. This can be a limiting factor in applications where restrictions on the PZT strip thickness conflict with those necessary to achieve the required frequency. In addition, high frequency and three-dimensional (3D) imaging require closely spaced

and extremely thin piezoelectric elements which are difficult to manufacture using the available macroscale fabrication processes [Gol00, Fos70].

1.3.4 Micromachined ultrasonic transducers (MUTs)

With the development of microfabrication processes, micromachined ultrasonic transducers (MUTs) have emerged as an alternative approach for ultrasound generation and detection, especially for biomedical imaging applications [Aka05]. Micromachined ultrasonic transducers consist of micromachined multilayered membrane resonators that are ten's of micrometers in width or diameter, and a few micrometers in thickness. The kinetic energy stored in the membranes is low because of the negligible mass of these membranes. This results in a higher bandwidth and a lower acoustic impedance mismatch between the transducer and the human body. [Ecc00]. There are two common types of MUTs based on their actuation principle: capacitive MUTs (CMUTs) and piezoelectric MUTs (PMUTs) (Fig. 1.3).

Capacitive MUTs utilize a vibrating membrane that is electrostatically actuated. The performance of CMUTs equals that of the conventional piezoelectric transducers in terms of the bandwidth, the dynamic range, the electromechanical coupling coefficient, and the generated sound pressure [Tor02, Khu00, Erg02]. The coupling coefficient is defined as the ratio of the mechanical energy delivered by the transducer to the total energy stored in the transducer. Imaging results from both one-dimensional (1D) and two-dimensional (2D) CMUT arrays have been reported [Ora03]. Although CMUTs have a high coupling coefficient [Rey01], various operational and fabrication considerations limit the achievable coupling. The voltage bias necessary to achieve the

maximum coupling is near the pull-in voltage of the CMUT elements, making it difficult to operate without causing any collapse of the elements [Ecc00].

Piezoelectric MUTs use the piezoelectric effect to vibrate the membranes. The PMUT consists of multilayered membranes one of which is a piezoelectric film. When a drive voltage is applied, the piezoelectric layer strains and generates the necessary deflection. This, in turn, generates ultrasound waves in the surrounding medium. Unlike conventional transducers, the operating frequency of the PMUT is not determined by the thickness of the piezoelectric layer; it is determined by the size and the material properties of the various layers in the membrane [Osb99]. The acoustic impedance and the coupling coefficient of the PMUTs can also be controlled through the device design [Aka05]. PMUTs also have high sensitivity, large displacement to voltage ratio, large pressure-to-voltage ratio, and large capacitance that cannot be realized with the conventional transducers [Per02]. PMUTs are less sensitive to parasitic capacitances than CMUTs because of the higher capacitance of PMUTs. Moreover, the lower electrical impedance of PMUTs allows a better matching to the readout circuit. Also, PMUTs are less sensitive to fabrication inconsistencies because the operation of PMUTs does not require a DC bias [Ver01].

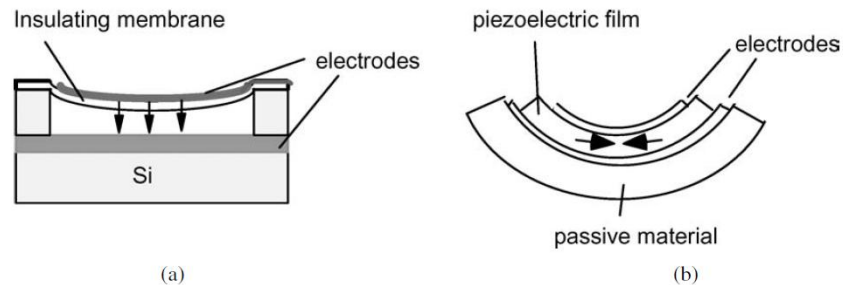


Figure 1.3: Schematic of cross-section of (a) CMUT and (b) PMUT. [Mur04]

Table 1.1: Typical values for the properties of common material used as a microheater

Material	PZT-5A	Au	Si
Thermal conductivity, K (W/m.K)	1.1-1.5	315	150
Density, ρ (Kg/m ³)	7650	19300	2330
Specific heat capacity, c_p (J/Kg.K)	350	130	700
$\rho c_p \times 10^6$ (J/m ³ K)	2.67	2.5	1.6

1.4. Heat generation in PZT devices

The temperature of the PZT element increases while converting the electrical energy to mechanical energy. This is mainly because of dielectric losses in the PZT element and structural damping losses in the PZT element and the surrounding medium. For example, a 27x10x1 mm³ PZT-4S actuator embedded in a 177.8x165.1x5.08 mm³ 50-ply glass epoxy laminate, when excited by 100 V_{rms} at 1000 Hz, has been reported to result in a temperature rise of about 55°C above the ambient temperature [Les96]. Heat generation in multilayered PZT actuators under high frequency excitation has been reported [Zhe96]. The heat generation is attributed primarily to the ferroelectric hysteresis loss in the stress free state. An approach to determine the temperature rise of the PZT element bonded to flat plate structures for sinusoidal voltage actuation has been developed [Zho95]. The internal heat generation in the PZT element is determined by using a coupled electromechanical model and the temperature field of the PZT element is analytically calculated. However, this model does not account for the heat generated in the surrounding medium due to damping of ultrasound waves. The self heating of PZT actuators has been traditionally considered as a limitation, because the properties of PZT are highly temperature sensitive, and continuous operation at high temperatures (close to the Curie temperature) may lead to degradation of the piezoelectric properties.

The high impedance of the PZT element limits the amplitude of the AC current flowing through the system. This can potentially suppress the losses due to parasitic resistances. Further, PZT promises higher thermal efficiency because of its lower thermal conductivity, which results in lower heat losses due to conduction through connecting wires [Cre05]. As shown in Table 1.1, the thermal conductivity of PZT is about two orders of magnitude less than that of metals. The product of density and specific heat capacity for the PZT, which is directly proportional to the time-constant of the heaters (for a system with convection boundary condition), is almost the same as that of metals (Table 1.1). The thermal coefficient of expansion of PZT (which is about $3.8 \times 10^{-6}/^{\circ}\text{C}$ [Ber98]) is closer to that of single crystal silicon, silicon nitride, and silicon dioxide than metals. Thus, PZT microheaters may cause less thermal stress (due to expansion mismatch) than conventional metal heaters.

The temperature of the PZT actuator is dependent on the electric field applied across its electrodes [Zho95]. Hence for a given drive voltage, higher temperature rise can be achieved by reducing the thickness of the PZT element. Thus, microfabricated PZT heaters bear significant potential. The conventional microfabrication techniques for PZT, though capable of achieving thickness of few microns, exhibit degraded material properties and device performance, thereby limiting the use of these actuators as microheaters [Po196]. However, the development of serial and batch mode bulk ultrasonic micromachining processes has allowed the microfabrication of bulk PZT materials with superior properties, making the proposed device feasible [Li06].

1.5. Applications

1.5.1. Needle tract cauterization during needle aspiration biopsy

Needle aspiration biopsy is a diagnostic procedure used to investigate the presence of tumor cells [Ame01]. In this technique, a thin, hollow needle is inserted into the targeted region to extract cell samples. These samples are then stained and examined under a microscope to determine the presence of tumor cells. A major surgical (or open) biopsy can be avoided by instead performing the needle aspiration biopsy. The needle aspiration biopsy is less traumatic than an open surgical biopsy. Needle aspiration biopsies are nowadays widely accepted as a diagnosis method for detection of thyroid, liver, kidney, lungs, bones and pancreas cancers.

Even though percutaneous biopsies are safe, there have been reports of potential risks of complications such as deposition of tumor cells or “seeding” along the needle tract. This can lead to spread of tumor cells to new regions [Tak00, Ryd03]. The percentage of seeding rates varies for various biopsy follow-up techniques as well as with different organs. The seeding rates have ranged from 0.6% to 12.5% for fine-needle aspiration biopsies (FNAB) [Pel00, Llo01] for hepatocellular carcinoma. Seeding rates for biopsies using the cutting needle technique has varied from 0.76% to 3.4% [Dur01, Kim00, Hua96]. Subcutaneous tumor seeding after fine needle aspiration biopsies of metastatic colonic adenocarcinoma [Go192] and metastatic pancreatic adenocarcinoma [Sio02] have also been reported.

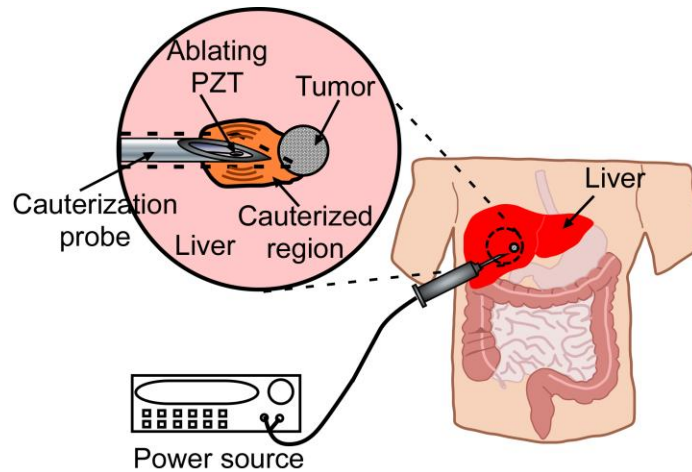


Figure 1.4: Concept diagram of ultrasonic cauterization device for needle tract cauterization during biopsy procedure.

Another probable complication that occurs with percutaneous needle biopsies is hemorrhage. Studies suggest that post biopsy hematoma in the liver can be as high as 18.3% and 23% with 2 mm Tru-cut needles and 1.6 mm Jamshidi needles, respectively [Sug91, Min87]. Further, this percentage can be higher for patients with cirrhosis and uncorrected coagulopathy [Pic86]. Another study suggests that minor to severe bleeding occurs in 90% of the patients after percutaneous needle biopsies [Ra187]. Subsequent imaging is required to detect these post biopsy hemorrhages. Various techniques have been used in the past for promoting blood clotting after percutaneous needle biopsies. These approaches involve trans-needle placement of steel coils [All88] and injection of fibrin [Chi89], gelatin particles and thrombin [Zin92], gelatin sponge pledgets [Smi96, Fan96], fibrinogen and thrombin [Fal99, Pau00]. These techniques do not provide a solution to the possibility of deposition of tumor cells along the needle tract [Pri04]. Needle tract ablation may be a helpful therapeutic option to avoid post biopsy hemorrhage and needle tract seeding (Fig. 1.4). A modified biopsy device can easily be

manufactured to facilitate use of post-biopsy cauterization to minimize the risk of bleeding and needle-tract seeding for high-risk patients.

1.5.1.1. Existing tissue cauterization methods

Electrocautery (monopolar and bipolar) or RF ablation is the most common method used for tissue cauterization [Haa62, Sch01]. In this technique, AC current at radio frequencies flowing through a biological tissue results in the heat generation. In monopolar electrocautery, the current flows from an electrode to the patient's body which serves as a ground. In bipolar electrocautery, the probe consists of two electrodes and only the tissue between the electrodes is cauterized [Joh82]. Electrocautery could interfere with the working of devices such as pacemakers and cannot be used in electrically sensitive regions such as heart and brain.

The use of laser energy for tissue cauterization has been investigated by Mizutani *et al.* [Miz92]. A portable laser system to stop internal bleeding has been reported [Dur99]. In addition to laser energy, microwaves have also been used for thermal ablation of biological tissue. The probe is designed to function as an antenna to concentrate the energy around it [Nah00].

Ultrasound has also been used for tissue cauterization. The harmonic scalpel, consisting of a titanium knife blade driven by a high power ultrasound transducer, has been used for simultaneous cutting and cauterization of biological tissue [Koc03]. Also, the use of HIFU for hemostasis has been reported in [Vae97]. However, HIFU requires bulky transducers making it expensive. Further, HIFU suffers from strong reflections

from air-tissue interfaces and bone-tissue interfaces. HIFU also has severe focus aberrations which could result in uncertainty in cauterized region.

There have been efforts at developing interstitial ultrasonic applicators. Interstitial ultrasound transducers made of cylindrical elements for omni-directional heating have been reported [Hyn92, Jar96, Die99]. Planar [Cho00] and weakly focused [Laf02] elements with rotation have been developed for selective heating of targeted tissue. Makin *et al.* has reported an approach for tissue ablation using linear array of PZT elements [Mak05]. A 32 element array of size $2.3 \times 49 \text{ mm}^2$ with an operation frequency of 3.1 MHz is used for the tissue cauterization.

1.5.1.2. Past work on ablation for biopsy procedure

Animal studies of radiofrequency (RF) ablation using the biopsy needle itself have been discussed by Kim *et al.* [Kim93]. The outside of the biopsy needle has been coated with a thin layer of electrically insulating material except for the last two centimeters. A RF electrical power source has been used to cauterize the needle tract. Comparison of hemorrhage after liver and kidney biopsies with and without the needle tract cauterization has been studied by Pritchard *et al.* [Pri04]. RF ablation by the introducer needle has been employed as the ablation procedure in these experiments. The study suggests that RF ablation reduced bleeding in liver and kidney by 63% and 97%, respectively. Mean amounts of blood loss in the liver in the RF and no-RF groups are 2.03 g and 5.50 g, respectively. Mean amounts of blood loss in the kidney in the RF and no-RF groups are 0.26 g and 8.79 g, respectively.

Past work on biopsy needle tract cauterization has been limited to RF ablation because of the difficulty in integration of other ablation methods with biopsy needles. The development of batch mode micro ultrasonic machining process [Li06], has resulted in the microfabrication of the PZT elements with repeatable piezoelectric properties, thereby making the use of the PZT elements for the proposed application feasible. Li *et al.* has reported a micromachined piezoelectric sensor integrated into a cavity in a biopsy needle for real time tissue differentiation [Li07]. In the experiments, piezoelectric discs of 50 μm thickness and 200 μm diameter has been used. The experiments have been performed using an ultrasonic human tissue phantom, and porcine fat and muscle samples. The magnitude and frequency of the electrical resonance impedance peak indicate tissue specific characteristics. In porcine tissue, the anti-resonance frequency changes by 13 MHz and the impedance magnitude decreases by 1600 Ω as the needle moves from fat to muscle. This device has demonstrated promise for needle positioning guidance during the fine needle aspiration biopsy.

In contrast with the biopsy tool sensor, a goal of this work is to evaluate a minimally invasive biological tissue ablation device for cauterization of the needle tract during biopsy procedures (Fig. 1.5a). Further, its compatibility with tissue contrast sensing would be an added advantage as it can be used as a measure of completion of tissue ablation as well as to aid in accurate ablation of the targeted tissue (Fig 1.5b). Measurement of the completion of tissue cauterization aids in limiting the extent of thermal damage to the surrounding healthy tissues. Since the PZT element is highly damped for heat generation, the quality factor of PZT element is quite low. Hence, a new

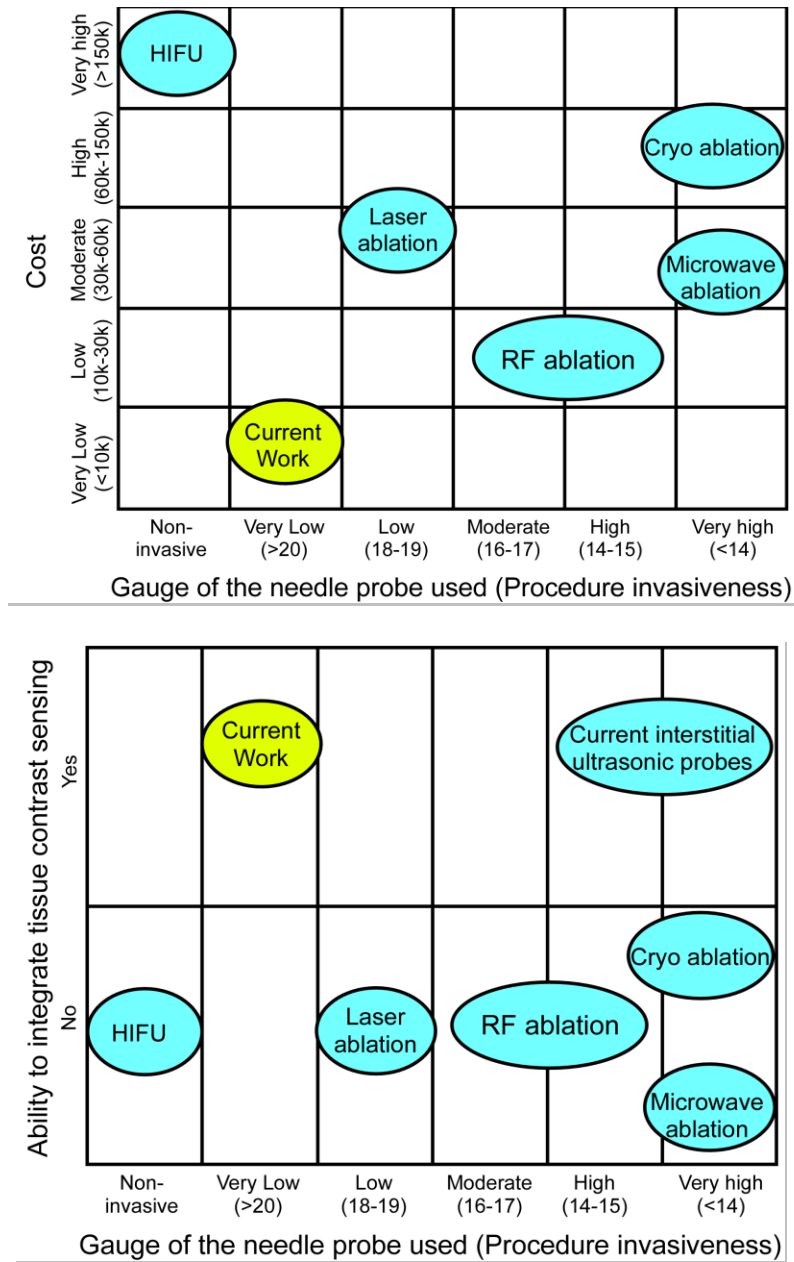


Figure 1.5: (a) Comparison of the cost versus invasiveness of the existing thermal cauterization method with the present work. (b) Comparison of the procedure invasiveness with the ability for integrated tissue contrast sensing for various thermal ablation methods [Dod00].

interface readout circuit also needs to be developed for measuring the resonance frequency shift of the PZT sensor due to tissue cauterization.

1.5.2. Microthermal stimulators for locomotion control of insects

Developments in digital electronics, communications and micro-fabrication over the past decades have spurred research in autonomous micro vehicles. The goal of these micro vehicles is to provide an inexpensive and disposable platform for carrying various sensors and actuators for military applications such as surveillance, radiation and chemical spill mapping and for civil applications such as aid in search and rescue operations, wildlife monitoring etc.

Interest in micro air-vehicles (MAVs) has existed atleast since the 1990's. One of the earliest battery powered MAVs were developed by Aero Vironment Inc. [Ash98]. Later, fixed wing prototypes were developed by Lockheed Sanders [Gre99] and Naval Research Laboratory [Kel02], respectively. A flexible wing MAV prototype was designed by Ifju *et al.* [Ifj02]. There had also been efforts at developing internal combustion engine based MAVs [Mor00] and solar powered MAVs [Pat00].

With more emphasis on miniaturization and inspiration from nature, micro-vehicles based on the flapping wing mechanism were developed. The insect-inspired flapping wing mechanism is attractive because it allows for hovering, short take off and landing. Michelson *et al.* reported an electromechanical entomopter insect based on flapping wing mechanism [Mic98]. Pornsin-Sirirak *et al.* reported the first micromachined wing using titanium alloy metal as the wing frame and Parylene-C as the wing membrane [Por01]. A biologically inspired micro-vehicle capable of aerial and terrestrial locomotion was reported [Bac09]. In addition to the aerial and terrestrial micro-vehicles, underwater micro-vehicles based on ionic polymer metal composite

actuator were reported in [Guo06, Guo08]. The micro-vehicle was able to move forward, backward and also change directions.

Numerous studies have been carried out to understand the factors controlling the locomotion of various species of insects. For example, the role of the motion sensitive horizontal cells in the lobula plate of the fly in controlling the yaw torque generated was studied in [Hau89, Hau90]. The dependence of the flight stability during maneuvers of hawk moths on the mechanosensory input from the antenna was reported by Sane *et al.* [San07]. An FM radio telemetry device, weighing 0.4 g was developed to record the muscle potential from a free flying moth [Kuw99]. Similarly, a radio frequency system with a shape memory alloy micro electrode was reported for neural recording of freely moving insects such as cockroaches [Tak04]. Mohseni *et al.* described a FM biopotential recording system for dorsal muscles of giant spinx moths fabricated on a foldable, lightweight polyimide substrate [Moh01].

There have also been preliminary studies of stimulating locomotion in land and air-borne insects. Electroneural stimulation by implanted electrodes is the most common technique that has been explored for stimulating motion. Moore *et al.* reported the steering of Madagascar hissing roaches with minimally invasive electrical stimuli to the basal region of either antennae or cerci [Moo98]. Similarly, electrical stimulation of the muscles in the hind legs of *Periplanata Americana* was reported in [Kuw94]. The effectiveness of electrical stimulation of the antenna of *Periplanata Americana* for controlling locomotion was reported in [Ho197]. A micromachined bioelectronic neuromuscular interface for the flight control of *Manduca Sexta* has been developed in [Boz08]. A biorobotic platform intended to explore the emergent behaviors resulting

from the coupling of a tethered fly and a wheeled robot was reported [Gra08]. An implantable flight control microsystem consisting of neural, muscular and visual stimulators for locomotion control of *Cotinis texana* was reported in [Sat08a]. Successful flight control of giant beetles (*Mecynorhina torquata*) was also demonstrated by direct neural stimulation of optic lobes [Sat08b]. The behavioral response of tiger beetles (*Cicindela Marutha*) to trains of bat-like ultrasonic pulses was reported [Yag97], but was successful only for flight initiation, not directional control.

Recent advances in microfabrication have made it possible to make sensors and actuators weighing less than a gram that can be attached as a “backpack”. Further, surgical implantation of microsystems during the late pupal stage in hawk moths has been demonstrated by Paul *et al.* [Pau06]. A microsystem consisting of a radio-frequency receiver assembly, a micro-battery and an electroneural stimulator has been developed by

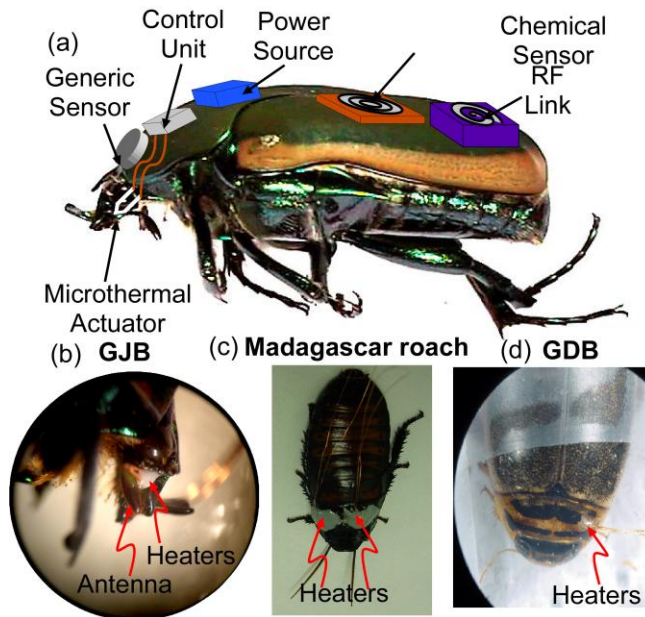


Figure 1.6: (a) Concept of instrumented insect. (b) Enlarged side view of the head of the green june beetle with thermal stimulators near the antenna. (c) Photo of Madagascar hissing roach with implanted thermal stimulators.

Sato *et al.* for electroneural flight control of *Mecynorhina Torquata* [Sat09].

The work here presents an effort at thermal stimulation using microheaters, which exploits the natural propensity of insects to escape fire, to initiate and control the direction of their locomotion. Preliminary studies suggest that insects experience discomfort at temperatures $>43^{\circ}\text{C}$ [Aba05]. This technique is potentially widely applicable across different species of insects due to its independence from any specific neurological or physiological structures of the concerned insect. In order to show the versatility of the proposed technique, experiments are done on the green June beetle (GJB) (*Cotinis Nitida*), Madagascar hissing roaches (*Gromphadorhina Portentosa*) and green diving beetles (GDB) (*Thermonectus*) (Fig. 1.6). This work explores the feasibility of PZT-5A based piezothermal stimulators and analyzes their performance for the locomotion control of insects.

1.6. Research challenges addressed in this work

The following are the goals targeted in this work.

1. Develop a simulation model to estimate the temperature rise in the PZT heaters for different geometries, operating frequencies and drive voltages. The model needs to account for the heat generated from losses within the PZT element and losses in the surrounding medium. Perform experiments to validate the proposed simulation model.
2. Conduct experiments to determine the most suitable operating conditions for the PZT heaters. Both single element heaters and dual element stacks need to be

evaluated. Perform experiments to show the feasibility of biological tissue cauterization using the proposed PZT heaters.

3. Show feasibility of thermal stimulation using PZT heaters for locomotion control of airborne, ambulatory and aquatic insects. Conduct experiments to determine the turning characteristics of these insects to thermal stimulation.
4. Design and fabricate a biopsy needle with embedded PZT heaters for needle tract cauterization during biopsy procedures. Perform experiments to determine the temperature profile generated by the cauterization tool. Show the feasibility of *in-situ* cauterization monitoring using the proposed biopsy tool.
5. System level implementation of the proposed biopsy needle tract cauterization tool with readout and actuation interface circuit. Because the PZT elements embedded in the wall of the biopsy needles are covered with epoxy for heat generation, the quality factor of these PZT elements tends to be low. Hence, the traditional oscillator circuit cannot be used for measuring the resonance frequency shift of the PZT element due to tissue cauterization. Hence, a new read-out circuit needs to be developed.

1.7. Outline

Chapter 2 provides the theory and the simulation model developed for estimating the temperature rise from the PZT heaters. Experiments for determining the most suitable operating conditions for the PZT heaters are also discussed. Chapter 3 describes the experiments on the locomotion control of air-borne, ambulatory and aquatic insects using microthermal stimulation. Chapter 4 discusses the experiments on biopsy needle

tract cauterization and *in-situ* cauterization monitoring using the proposed PZT heaters. The readout circuit developed to measure the resonance frequency shift of the PZT heaters due to tissue cauterization is described in Chapter 5. Chapter 6 provides the conclusion and the future work.

CHAPTER 2

SIMULATION MODEL AND EXPERIMENTAL CHARACTERIZATION OF PIEZOCERAMIC HEATERS

As discussed in Chapter 1, the goal of this work is to explore the heat generation capability of piezoceramic microheaters for biological tissue cauterization (Fig. 2.1). This chapter discusses the experiments for characterizing the PZT heaters for determining suitable operating conditions [Vis01]. PZT heaters of 3.2 mm diameter and 191 μm in thickness are used in the experiments. Section 2.1 describes the theory and simulation model used to estimate the heat generated by these heaters. Section 2.2 discusses the device design and fabrication of the heaters used in this work. The initial portions of Section 2.3 discuss the experimental results for the characterization of these heaters. The latter portion of Section 2.3 shows the feasibility of using these heaters for cauterization of biological tissues.

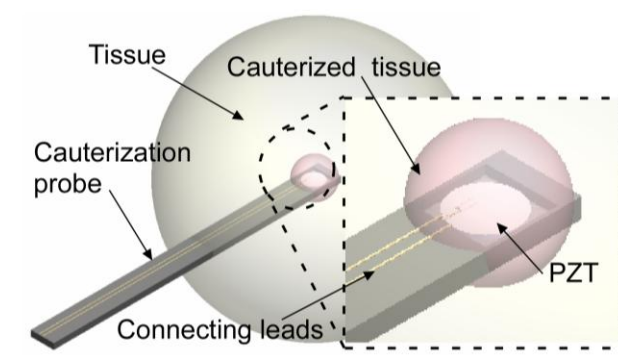


Figure 2.1: Concept diagram of a PZT based cauterization tool.

2.1. Simulation model for temperature rise in PZT heater

2.1.1. Theory

The heat generation from a piezoelectric material is primarily due to losses within piezoelectric material and attenuation of ultrasound waves in the surrounding medium.

(i) Losses within the piezoelectric material

For a ferroelectric material, there are four sources of losses in the material [Har82]: (1) losses due to domain wall motion, (2) losses due to presence of point defects in the lattice structure, (3) microstructural losses arising from the grain boundaries due to polycrystalline nature of the material and (4) ohmic losses (which are relevant mainly for highly conductive materials). However, in piezoceramic material the domain wall losses dominate the other three losses. In piezoelectric material, the domain wall losses consist of dielectric, elastic and electromechanical hysteresis losses.

The piezoelectric material is modeled using linear theory of piezoelectricity. In linear piezoelectricity, the following equations govern the behavior of piezoelectric materials [Iee87,Ike96]:

$$S_p = s_{pq}^E T_q + d_{kp} E_k \quad (2.1)$$

$$D_i = d_{iq} T_q + \varepsilon_{ik}^T E_k \quad (2.2)$$

where T is the stress tensor, S is the strain tensor, E is the electric field vector, D is the electric displacement vector, s_{pq}^E is the mechanical compliance coefficients, d_{kp} is the piezoelectric coupling coefficients, and ε_{ik}^T is the dielectric permittivity coefficients.

In general, there are 36 independent constants for mechanical compliance (s_{pq}^E), 18 for piezoelectric coupling (d_{kq}), and 9 for dielectric permittivity (ϵ_{ik}^T). However, due to the orthotropic nature of most piezoelectric materials, the compliance matrix takes the following form:

$$s^E = \begin{bmatrix} s_{11} & s_{12} & s_{13} & 0 & 0 & 0 \\ s_{21} & s_{22} & s_{23} & 0 & 0 & 0 \\ s_{31} & s_{32} & s_{33} & 0 & 0 & 0 \\ 0 & 0 & 0 & s_{44} & 0 & 0 \\ 0 & 0 & 0 & 0 & s_{55} & 0 \\ 0 & 0 & 0 & 0 & 0 & s_{66} \end{bmatrix} \quad (2.3)$$

Further, for the PZT used in this model, $s_{12} = s_{21}$, $s_{31} = s_{13}$, $s_{23} = s_{32}$, $s_{11} = s_{22}$, and $s_{44} = s_{55}$. Most dielectric materials do not exhibit cross-coupling in the relationship between electric field and electric displacement. Hence, the permittivity matrix gets reduced to a diagonal matrix. Often the permittivity values in the ‘11’ and ‘22’ directions are also equal. Hence, the permittivity matrix can be written as:

$$\epsilon = \begin{bmatrix} \epsilon_{11} & 0 & 0 \\ 0 & \epsilon_{11} & 0 \\ 0 & 0 & \epsilon_{33} \end{bmatrix} \quad (2.4)$$

Similarly, the symmetry in the crystal structure of the piezoelectric materials allows for coupling only in certain directions as shown below:

$$d = \begin{bmatrix} 0 & 0 & 0 & 0 & d_{15} & 0 \\ 0 & 0 & 0 & d_{24} & 0 & 0 \\ d_{31} & d_{32} & d_{33} & 0 & 0 & 0 \end{bmatrix} \quad (2.5)$$

For the PZT under consideration $d_{31} = d_{32}$ and $d_{24} = d_{15}$. The constitutive equations above can be combined into a single matrix as shown below:

$$\begin{bmatrix} S_1 \\ S_2 \\ S_3 \\ S_4 \\ S_5 \\ S_6 \\ D_1 \\ D_2 \\ D_3 \end{bmatrix} = \begin{bmatrix} s_{11}^E & s_{12}^E & s_{13}^E & 0 & 0 & 0 & 0 & 0 & 0 & d_{31} \\ s_{12}^E & s_{11}^E & s_{13}^E & 0 & 0 & 0 & 0 & 0 & 0 & d_{31} \\ s_{13}^E & s_{13}^E & s_{33}^E & 0 & 0 & 0 & 0 & 0 & 0 & d_{33} \\ 0 & 0 & 0 & s_{55}^E & 0 & 0 & 0 & d_{15} & 0 & 0 \\ 0 & 0 & 0 & 0 & s_{55}^E & 0 & d_{15} & 0 & 0 & 0 \\ 0 & 0 & 0 & 0 & 0 & s_{66}^E & 0 & 0 & 0 & 0 \\ 0 & 0 & 0 & 0 & d_{15} & 0 & \varepsilon_{11}^T & 0 & 0 & 0 \\ 0 & 0 & 0 & d_{15} & 0 & 0 & 0 & \varepsilon_{11}^T & 0 & 0 \\ d_{31} & d_{31} & d_{33} & 0 & 0 & 0 & 0 & 0 & 0 & \varepsilon_{33}^T \end{bmatrix} \begin{bmatrix} T_1 \\ T_2 \\ T_3 \\ T_4 \\ T_5 \\ T_6 \\ E_1 \\ E_2 \\ E_3 \end{bmatrix} \quad (2.6)$$

The losses in the piezoelectric material can be modeled by using complex physical constants in these constitutive equations. One assumption in this model is that the losses are small and can be treated as perturbations. The dielectric, elastic and electromechanical coefficients can now be written as [Uch06]:

$$\varepsilon^{T*} = \varepsilon^T (1 - j \tan \delta) \quad (2.7)$$

$$s^{E*} = s^E (1 - j \tan \phi) \quad (2.8)$$

$$d^* = d(1 - j \tan \theta) \quad (2.9)$$

where, δ is the phase delay between the electric displacement and applied electric field under a constant stress, ϕ is the phase delay between strain and applied stress under a constant electric field and θ is the phase delay between electric displacement and applied stress. The power dissipated within the piezoelectric material is then given by:

$$P = \frac{I_m V_m}{2} \cos \varphi = \frac{V_m^2}{2} \text{Re}(A) \quad (2.10)$$

$$Q_p = \frac{P}{\text{volume}(PZT)} \quad (2.11)$$

where, V_m and I_m are the magnitude of the actuation voltage and current, φ denotes the phase angle difference between the current and the voltage, A is the complex admittance of the PZT embedded structure and Q_p is the internal heat generation rate per unit volume in the PZT element. A method for determining the complete set of complex dielectric, elastic and electromechanical coefficients is described in [Alg04].

(ii) Losses in the surrounding medium

The ultrasound wave travelling in the surrounding medium is attenuated due to material damping. This energy loss results in heat generation in the surrounding medium. In order to simulate the resulting temperature rise, a steady state heat conduction model is used [Mea98].

$$\rho_t c_t \frac{\partial T}{\partial t} = \nabla \cdot k \nabla T + \dot{q} \quad (2.12)$$

where ρ_t is the density (kg.m^{-3}), c_t is the specific heat capacity ($\text{J.kg}^{-1}.\text{K}^{-1}$), k is the thermal conductivity ($\text{W.m}^{-1}.\text{K}^{-1}$), T is the temperature (K), and \dot{q} is the heat generation rate per unit volume due to ultrasound attenuation (W.m^{-3}). The heat generation rate per unit volume in the surrounding medium is given by:

$$\dot{q} = \alpha \frac{pp^*}{\rho_t c} \quad (2.13)$$

where α is the ultrasound attenuation coefficient, p is the acoustic pressure, p^* is the complex conjugate of the pressure, and c is the sound wave velocity.

In the absence of a pressure source, the pressure distribution in the surrounding medium due to PZT vibration can be determined by solving the following wave equation:

$$\frac{1}{\rho_t c^2} \frac{\partial^2 p}{\partial t^2} + \nabla \cdot \left(-\frac{1}{\rho_t} \nabla p \right) = 0 \quad (2.14)$$

The losses in the medium are modeled using complex sound velocity as shown below [Wat84]:

$$k = \frac{\omega}{c} - i\alpha \quad (2.15)$$

$$c_c = \frac{\omega}{k} \quad (2.16)$$

Here c_c is the complex wave velocity of the medium. Because the PZT element is excited using a sinusoidal wave, the pressure wave can be assumed to vary harmonically in time as:

$$p(x, y, z, t) = p(x, y, z) e^{i\omega t} \quad (2.17)$$

The normal acceleration (a_n) of the PZT material due to vibrations is related to the pressure wave generated in the surrounding medium by the following boundary condition at the PZT-medium interface:

$$n \cdot \left(\frac{1}{\rho_t} \nabla p \right) = a_n \quad (2.18)$$

where n is the unit normal vector to the PZT-medium interface.

2.1.2. Simulation model

A 3-D multi-physics finite element model (COMSOL 3.5a Multiphysics®) was used to determine the heat generated by the PZT heaters for different geometries, operating frequencies, and drive voltages. The simulation was subdivided into 3 steps: the first step involves modeling the heat generated within the PZT element. The piezo

solid module in COMSOL was used to determine the electro-mechanical admittance of the PZT element, which in turn determined the heat generation rate within the PZT element. The losses in the PZT element were modeled by using complex values for dielectric, elastic and electromechanical coefficients as shown in equations 2.7-2.9. The losses in the surrounding medium were modeled by using complex material properties as shown in equation 2.16. The medium surrounding the PZT element was assumed to be isotropic for wave propagation. Next, the acoustic module was used to determine the pressure waves generated in the surrounding medium by the vibration of the PZT element. Finally, a generalized heat transfer module was used to determine the temperature rise in the PZT element and surrounding medium. The heat generation rate per unit volume in the surrounding medium was calculated using equation 2.13. Convection heat flux (to surrounding air) was used as a boundary condition for all the boundaries.

2.2. Device design and fabrication

The simulation model described in section 2.1 is used to determine the most suitable shape for the heater. Simulations were performed for PZT ultrasonic heaters of different shapes, but with the same volume and cross-sectional area. The heaters were assumed to be bonded to a brass substrate. Shapes such as circle, square and rectangle (length = 2x width) were considered in the simulations. A voltage of 6 V (peak-peak amplitude) was applied across the electrodes of the PZT element. Ultrasound attenuation coefficients of 100, 170 and 1100 dB/m/MHz (obtained from the experiments described in Section 2.3.2) were used for the brass substrate, conductive and non-conductive epoxy,

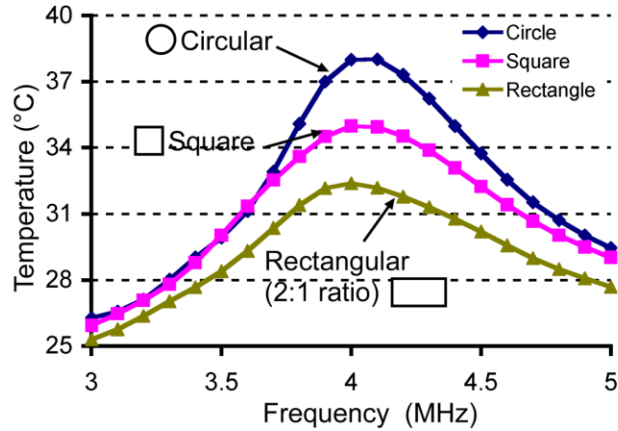


Figure 2.2: Comparison of the simulated temperature rise of the PZT element for a given drive voltage bonded to a brass substrate. Different cross-sectional shapes were used, with same volume and cross-sectional area. The circular shape provides the most favorable response.

respectively. The simulations indicated that the circular shape is most suitable for a given volume and cross-sectional area. For a given voltage the circular shape generated 21% and 39% more temperature rise as compared to the square and the rectangular shapes, respectively (Fig. 2.2).

This study uses PZT-5A material because it offers higher Curie temperature ($\approx 350^\circ\text{C}$) than other forms of PZT, and consequently allows higher working temperatures. Moreover, the piezoelectric constant (d_{31}) and relative dielectric constant (K) of PZT-5A show lower temperature sensitivity [Zho95]. Commercially available PZT-5A discs (Piezo Systems Inc., Woburn, MA, USA) of 3.2 mm diameter and 0.191 mm thickness were used for experiments.

Figure 2.3a shows the schematic of the device designed for simulation model validation. PZT heaters of 3.2 mm diameter and 0.191 mm thickness were used. The PZT disc was covered with 130- μm thick and 270- μm thick layers of conductive and non-conductive epoxy, respectively.

Figures 2.3b and 2.3c show the schematic and dimensions of the unstacked and stacked structures used for device characterization experiments. For unstacked structures, thin gold bond wires (diameter $\approx 25.4 \mu\text{m}$, length $\approx 10 \text{ cm}$) were connected to the PZT discs by conductive epoxy, followed by an insulating layer of non-conductive epoxy. For stacked structures, the PZT discs were bonded in pairs by a thin layer of non-conductive epoxy. Four gold bond wires of $25.4 \mu\text{m}$ diameter (two for each PZT element) were used to provide the electrical connections to the PZT discs as described above. Photographs of the fabricated structures are shown in Fig. 2.3d.

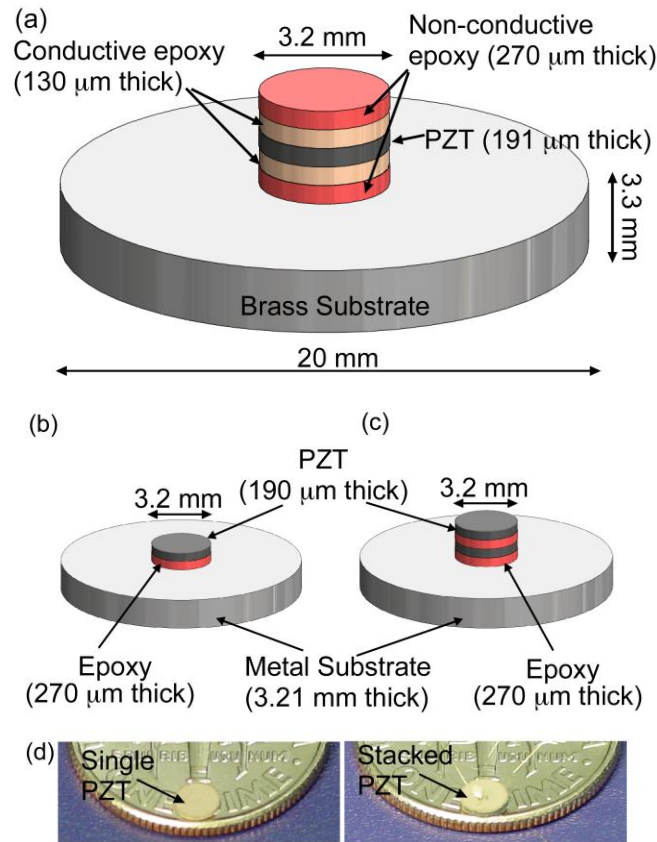


Figure 2.3: (a) Schematic of the device designed for simulation model validation. Schematic of the (b) unstacked PZT heater and (c) stacked PZT heater. (d) Photograph of the fabricated unstacked and stacked PZT heater.

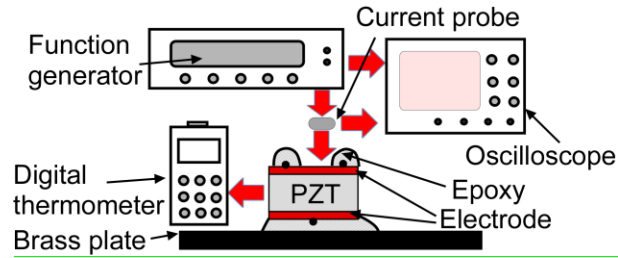


Figure 2.4: Schematic of the test setup used in the characterization PZT heaters.

2.3. Device and operating parameter characterization

2.3.1. Experimental setup

The experimental setup is illustrated in Fig. 2.4. The heaters were actuated using a HP 33520A function generator. The voltage applied across the electrodes and the current flowing through the heaters were measured using an Agilent DSO6014A oscilloscope and Tektronix CT1 (1 GHz) current probe, respectively. A K-type thermocouple attached to a digital thermometer was used to measure the surface temperature of the PZT heater.

2.3.2. Simulation model validation

Simulations and experiments were carried out for circular PZT-5A heaters of 3.2 mm diameter and 0.191 mm thickness bonded to 3.3 mm thick brass substrates (Fig. 2.3a). Sinusoidal actuation voltages of peak-peak amplitude 4 V, 5 V and 6 V, were used to determine the ultrasound attenuation in the brass substrate, conductive and non-conductive epoxies. The material properties used in the simulations are listed in Table 2.1.

Experiments were performed to determine the temperatures attained for various actuation frequencies and were compared against the simulation results (Fig. 2.5a). The simulation results were in good agreement with the experimental results for attenuation values of 100, 170 and 1100 dB/m/MHz in the brass, conductive and non-conductive epoxy, respectively.

Simulations were also performed to determine the temperature rise for varying input power from the PZT heaters bonded to elytra of a beetle carcass. The simulations were performed using a fitted ultrasound attenuation coefficient of 1000 dB/m/MHz for the elytra of the beetle carcass. The thickness of elytra was assumed to be 200 μm . The properties of the elytra used in the simulations are listed in Table 2.1. The temperature rise from the PZT heater obtained from simulations was compared with the experiments (Fig. 2.5b). The simulation and experimental results match within 10%.

Table 2.1: Properties of the materials used in the finite element simulations.

PZT 5A		Value	Units	Non-conductive epoxy	Value	Units
Piezo electric constants	d_{31}	-175	10^{-12} m/V	Elasticity module	0.55	10^{10} N/m ²
	d_{33}	400		Thermal conductivity	0.5	W/m-K
	d_{15}	590		Attenuation	1100	dB/m/MHz
Elastic constants	c_{11}	6.6	10^{10} N/m ²	Density	1096	Kg/m ³
	c_{12}	4		Conductive epoxy		
	c_{13}	4		Density	3000	Kg/m ³
	c_{33}	5.2		Elasticity module	1.875	10^{10} N/m ²
	c_{44}	1.2		Attenuation	170	dB/m/MHz
	c_{66}	1.25		Thermal conductivity	1.58	W/m-K
Dielectric constants	ϵ_{33}/ϵ_0	830		Brass		
	ϵ_{11}/ϵ_0	916		Density	8500	Kg/m ³
Density		7750	Kg/m ³	Attenuation	100	dB/m/MHz
Structural damping		0.1		Elasticity Module	10.5	10^{10} N/m ²
Coupling loss		0.1		Thermal conductivity	115	W/m-K
Dielectric loss		0.1		Beetle's elytra		
Thermal conductivity		1.5	W/m-K	Attenuation	1000	dB/m/MHz
Miscellaneous				Thermal conductivity	0.4	W/m-K
Convection coefficient		20	W/m ² .K	Density	1000	Kg/m ³
Initial temperature		300	K	Elasticity module	6	10^9 N/m ²

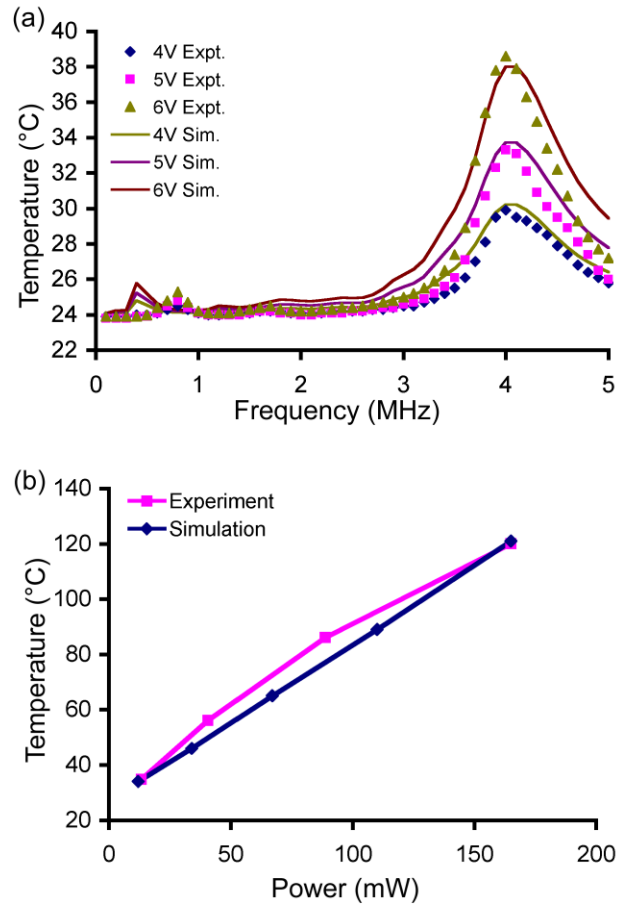


Figure 2.5: (a) Comparison of the simulated and experimental data for temperature attained for varying applied voltage by PZT elements bonded to a 3.3 mm thick brass plate. The properties of the material used in the simulation are provided in Table 2. (b) Comparison of the simulated and experimental temperature rise generated by the PZT heater for varying input power when attached to elytra of a beetle carcass. The simulations were performed with fitted ultrasound attenuation coefficients of 1100, 170, 100, 1000 dB/m/MHz for the non-conductive epoxy, conductive epoxy, brass substrate and elytra, respectively. The measured thermal efficiency of the heater was $0.93^{\circ}\text{C}/\text{mW}$ at 85°C .

2.3.3. Operating frequency selection

The piezoceramic ultrasonic heaters were characterized to determine the most suitable operating frequency. The heaters were bonded to 3.3 mm thick brass plate using non-conductive epoxy. The thermal efficiency was measured as a function of frequency

and compared with the electromechanical impedance of the structure. The thermal efficiency of the heater is defined as the temperature rise per unit watt of power consumed. Figure 2.6a suggests that the heater attains local maximum in thermal efficiency around each resonance frequency of the element.

Further analysis was performed to determine the best resonance mode for operation of the PZT heater. Figure 2.6b suggests that the thermal efficiency attained in each resonance mode is directly proportional to the effective electromechanical coupling coefficient of the resonance mode. The electromechanical coupling coefficient of a resonance mode is defined as [Che05]:

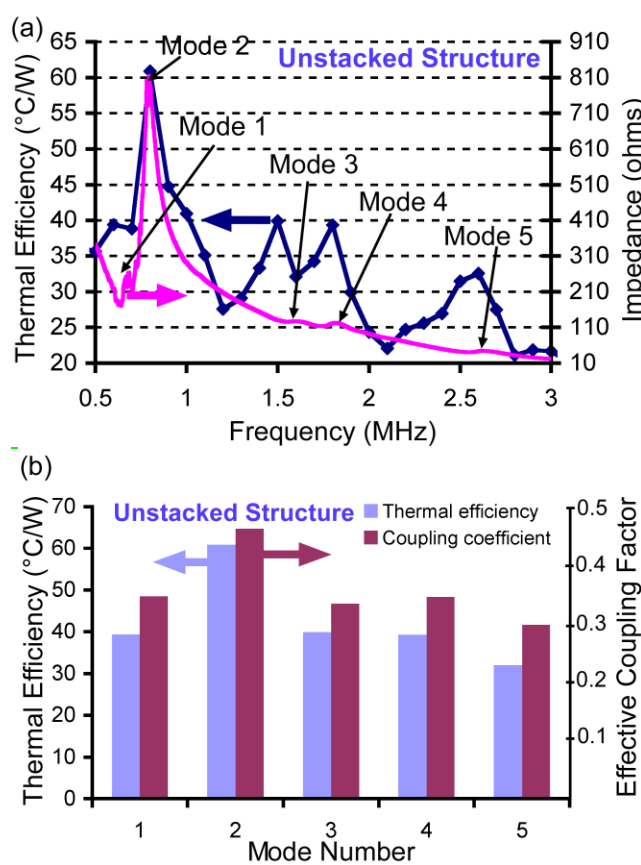


Figure 2.6: (a) Thermal efficiency and electromechanical impedance of unstacked PZT heater bonded to a brass substrate as a function of frequency. (b) Thermal efficiency and coupling factor for various mode shapes observed in unstacked PZT heater bonded to brass.

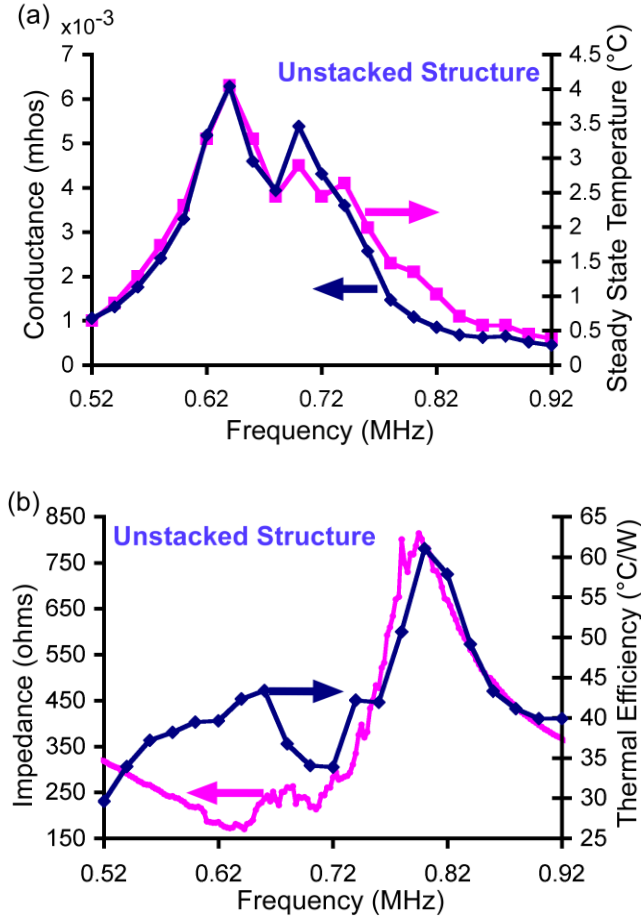


Figure 2.7: (a) Comparison of temperature attained by PZT and conductance as a function of frequency of excitation for mode 2 on brass. (b) Comparison of thermal efficiency and electromechanical impedance of the PZT heater as a function of frequency for mode 2 on brass.

$$k_{eff} = \left(\frac{f_{ar}^2 - f_r^2}{f_{ar}^2} \right)^{0.5} \quad (2.19)$$

where f_{ar} is the anti-resonance frequency, and f_r is the resonance frequency. For the present heater bonded to the brass plate, mode 2 is the optimum. Closer analysis of mode 2 indicates that the heater attains maximum steady state temperature for a given voltage at the frequency of maximum electromechanical conductance (Fig. 2.7a). This is expected, as higher conductance results in higher current amplitude, which, in turn, leads

to higher temperature rise. However, the thermal efficiency of the heater is maximum around the frequency of maximum impedance (Fig. 2.7b). This is believed to be due to decrease in the losses due to parasitic resistances. Hence, there is a compromise in selecting the operating frequency because the maximum steady state temperature rise per unit voltage occurs at the frequency of maximum conductance, whereas the maximum thermal efficiency occurs at frequency of maximum impedance.

2.3.4. Effect of voltage offset and substrate material

Experiments indicate that maximum thermal efficiency occurs at zero DC offset in the drive voltage, and that the thermal efficiency decreases with increase in offset voltage. This is believed to be due to the internal stress generated in the PZT element by the DC offset voltage. This decreases the electromechanical coupling coefficient as discussed in [Cho05]. This, in turn, reduces the thermal efficiency of the heater. Experiments suggest that for an element bonded to a brass plate the thermal efficiency decreases by 28% for an applied voltage offset of 4 V (Fig. 2.8a).

The thermal efficiency of the PZT heater when bonded to different substrates was studied. The thermal efficiency of the heater was higher for substrates with high damping coefficients and lower thermal conductivity like biological tissues, and lower for substrates such as metals (Fig. 2.8b). The heaters attained a maximum thermal efficiency of $0.93^{\circ}\text{C}/\text{mW}$ when bonded to biological tissue (elytra of a beetle carcass). The thermal efficiency was $0.06^{\circ}\text{C}/\text{mW}$ and $0.17^{\circ}\text{C}/\text{mW}$ for brass and glass substrates, respectively.

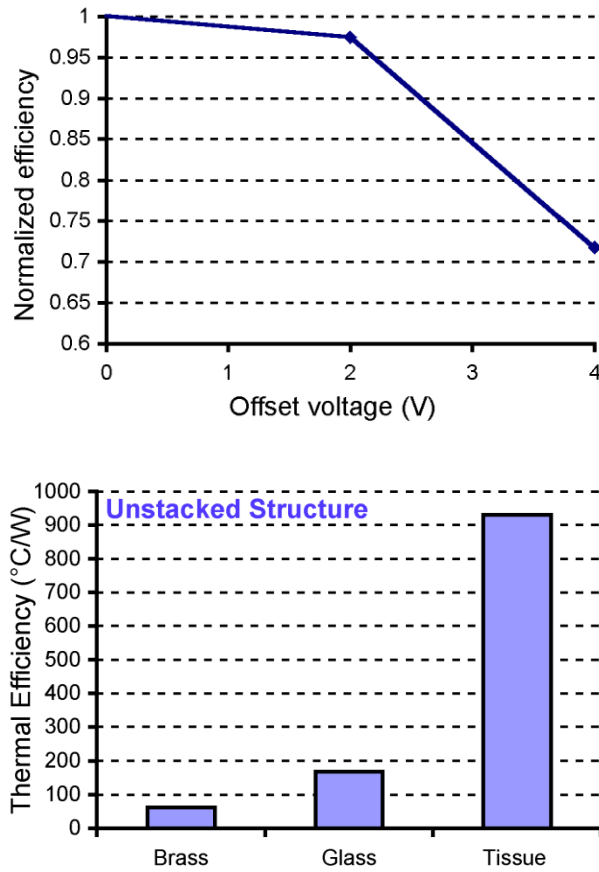


Figure 2.8: (a) Variation of normalized thermal efficiency ($efficiency_{offset}/efficiency_{zero-offset}$) with increase in the DC offset in the excitation voltage. The thermal efficiency was found to decrease with increase in the offset voltage. (b) Thermal efficiency of PZT microheater on different substrates. The efficiency of the heater was higher for highly damping substrates like tissues.

2.3.5. Stacked structure design

The stacked heater elements (Fig. 2.3c) were tested in four modes of operation: actuation of bottom element alone, actuation of top element alone, actuation of both elements with electric field in same direction, and actuation of both elements with electric field in opposite direction. Figure 2.9 shows the comparison of maximum steady state temperature and thermal efficiency attained during various modes of operation of the

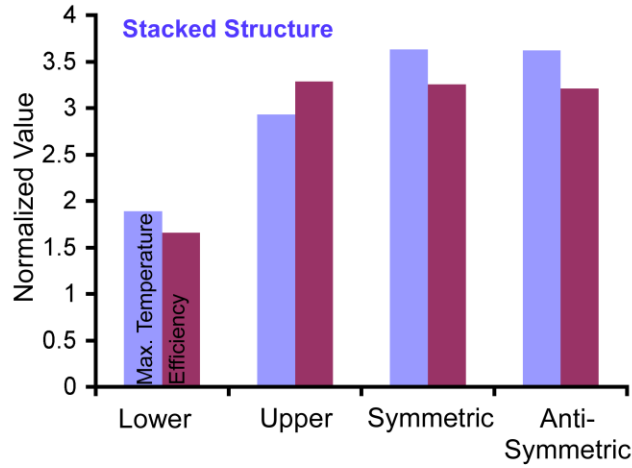


Figure 2.9: Normalized maximum temperature ($T_{max}/T_{max-unstacked}$) and efficiency ($eff/eff_{unstacked}$) attained by stacked PZT heater. The stacked heaters were tested in four modes of operation: actuation of lower element alone, actuation of upper element alone, symmetric actuation of both elements with electric field in same direction and anti-symmetric actuation of both elements with electric field in opposite direction.

stacked heater. Actuation of the bottom PZT heater alone causes larger temperature rise than unstacked heaters – likely because of the increase in the damping due to the presence of epoxy on both sides of the element. Further, the actuation of the top element alone generates more temperature rise and is more efficient than the lower one – likely because of thermal isolation provided by the lower element. Actuation of both the elements within a stack generates the maximum temperature rise, and the thermal efficiency is slightly less than that of actuating only the top element. Actuation of both the elements in the stacked structure provides a 3.5x increase in the steady state temperature, and 3x increase in the thermal efficiency of the heater when compared to unstacked heater. The direction of the applied electric field does not have a measurable effect on the temperature rise and the thermal efficiency of the stacked heaters.

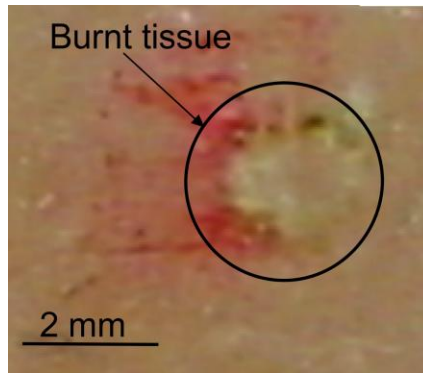


Figure 2.10: Photograph of the cauterization of porcine tissue using unstacked PZT heater probe. The heater probe brands the tissue in 2-3 seconds with $10 V_{RMS}$. The interface temperature is $\approx 150^{\circ}C$.

2.3.6. Biological tissue cauterization experiments

Experiments were performed using porcine tissue samples to show the feasibility of the microheaters in medical applications. Unstacked circular PZT heaters were used in these experiments. The heaters were bonded to glass substrates by non-conductive epoxy. The voltage output of the function generator was amplified using Krohn-Hite model 7500 amplifier. The PZT heater probe branded the porcine tissue when a sinusoidal voltage of $10 V_{RMS}$ was applied for 2-3 seconds. The interface temperature rose $150^{\circ}C$, which is much greater than the required temperature of $70-100^{\circ}C$ required for applications such as cauterization [Pri04]. The 3.2 mm diameter and 0.191 mm thick heater generated a burn mark of about 2 mm in diameter as shown in Fig. 2.10. This shows the feasibility of using the proposed microheaters for biological tissue cauterization applications.

2.4. Conclusions

There are a number of conclusions that can be drawn based on the findings of this chapter. Simulations suggest the circular shape is most suitable to maximum temperature rise at a given drive voltage for constant cross-sectional area and volume. Circular PZT-5A heaters (3.2 mm diameter and 0.191 mm thickness) were used in experiments. The PZT heaters attained maximum temperature at the frequency of maximum conductance and maximum thermal efficiency at frequency of maximum impedance. Further, the thermal efficiency of each resonance mode was proportional to the electromechanical coupling coefficient of that mode. The thermal efficiency of the heaters decreased with an increase in the DC offset of the applied sinusoidal voltage. Further, the thermal efficiency was higher in non-conducting and highly damping substrates. The performance of the stacked PZT structure was also compared with unstacked structure. The stacked structure provided 3.5x the maximum temperature rise and 3x the thermal efficiency attained by the unstacked heaters. The direction of applied electric field did not measurably influence the heating characteristics of the stacked elements. An unstacked heater was used in the cauterization of porcine tissue samples. A sinusoidal input voltage of 10 V_{RMS} generated an interface temperature of 150°C and branded the porcine tissue.

CHAPTER 3

LOCOMOTION CONTROL OF AIRBORNE, AMBULATORY AND AQUATIC INSECTS USING MICROTHERMAL STIMULATION

This chapter describes the feasibility of using microthermal stimulators for locomotion control of ambulatory and airborne insects [Vis02, Vis03]. Experiments are performed on green June beetles (GJB) (*Cotinis nitida*), Madagascar hissing roaches (*Gramphadorhina Portentosa*) and green diving beetles (*Thermonectus*) to show the versatility of proposed technique. Section 3.1 describes the design and fabrication of piezothermal stimulators used in this work. It also describes the simulation model used for estimating the insect-stimulator interface temperature. The initial portion of Section 3.2 describes the experiments on the characterization of the stimulators. The latter portion of Section 3.2 discusses the experiments on green June beetles, Madagascar hissing roaches, and green diving beetles, respectively. Finally, scaling limits of the piezothermal stimulators and battery requirements are discussed in section 3.3.

3.1. Design and fabrication

Four different kinds of PZT based microstimulators (P1, P2, P3, P4) are investigated. The PZT based stimulators generate heat due to dielectric losses in the PZT and the damping of ultrasonic waves in PZT and surrounding medium

[Lia96]. The PZT stimulators are believed to be suitable for this application as they have high impedance even at thicker cross-section (hundreds of microns), which is required to provide structural rigidity to withstand the forces during implantation and bonding and reduce parasitic losses in the connecting wires. PZT-5A is used in the present study because of its higher Curie temperature ($\approx 350^\circ\text{C}$), which allows higher in vivo working temperatures. Moreover, the piezoelectric constant (d_{31}) and relative dielectric constant of PZT-5A show lower temperature sensitivity as compared to other PZT materials like PZT-5H [Zho95].

A finite element simulation model is developed to predict the input power required to achieve the target temperature by the stimulators. The steady state heat conduction model in COMSOL Multiphysics® is used in these simulations. The simulations are performed for a rectangular PZT-5A piezothermal stimulator ($1 \times 0.5 \times 0.127 \text{ mm}^3$) used in the experiments on GJB (Fig. 3.1). Each stimulator is assumed to be surrounded by $100 \text{ }\mu\text{m}$ thick copper wire and $200 \text{ }\mu\text{m}$ thick non-conductive epoxy on both sides for insulation. The stimulator is assumed to be implanted in the tissue. In order to reduce the complexity of the model, the insect body is modeled using a $15 \times 10 \times 6 \text{ mm}^3$ cuboid. Because of high impedance, joule heating can be

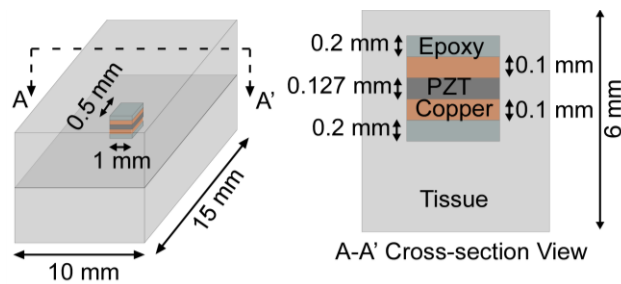


Figure 3.1: Schematic of the model used in the finite element simulations for predicting insect stimulator interface temperature.

Table 3.1: Material properties used in the finite element simulation of interface temperature generated for various input power.

Beetle tissue properties	Epoxy Properties
Initial Temp., $T_1= 295$ K	Initial Temp., $T_2=295$ K
Density, $\rho_1=1100$ kg/m ³	Density, $\rho_2=1096$ kg/m ³
Heat Capacity, $c_1= 3700$ J/kg.K	Heat Capacity, $c_2 = 110$ J/kg.K
Thermal Conductivity, $k_1= 1$ W/m.K	Thermal Conductivity, $k_2= 0.25$ W/m.K
Copper wire properties	PZT-5A properties
Initial Temp., $T_3= 295$ K	Initial Temp., $T_4=295$ K
Density, $\rho_3=8700$ kg/m ³	Density, $\rho_4=7650$ kg/m ³
Heat Capacity, $c_3= 385$ J/kg.K	Heat Capacity, $c_4 = 350$ J/kg.K
Thermal Conductivity, $k_3= 400$ W/m.K	Thermal Conductivity, $k_4= 1.5$ W/m.K

neglected. All the input power delivered is assumed to be converted into heat – either within the PZT element or within the surrounding tissue. The tissue boundaries exposed to surroundings are assumed to be at room temperature of 295 K. The material properties used in the simulation are listed in Table 3.1.

Figure 3.2 shows the simulation results for the variation of the maximum temperature in the stimulator and the average temperature at the insect stimulator interface for varying input power. The average temperature is calculated by averaging

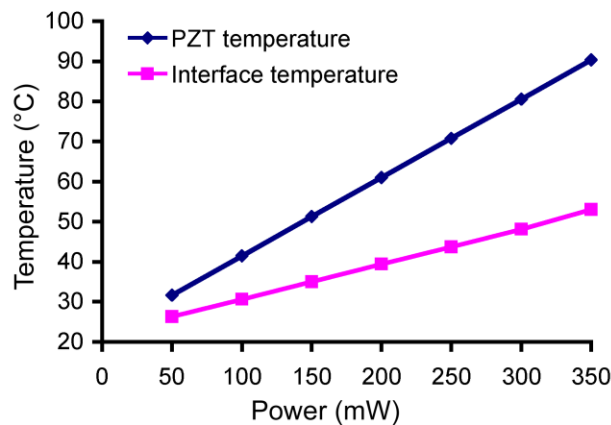


Figure 3.2: Finite element simulation results showing the maximum temperature in the PZT and the temperature at the tissue interface as a function of varying input power.

Table 3.2: Comparison chart for different types of piezothermal stimulators used in the experiment.

	Shape	Dim. (mm)	Property
P1	○	$\Phi=3.2; h=0.2$	$C = 0.65 \text{ nF}$
P2	▭	$1 \times 3 \times 0.127$	$C = 0.37 \text{ nF}$
P3	▭	$1 \times 0.5 \times 0.127$	$C = 0.06 \text{ nF}$
P4	○	$\Phi=0.2; h=0.04$	$C = 0.012 \text{ nF}$

the temperature profile over the interface area between the insect and stimulator. The simulations suggest that the target temperature ($\approx 43^\circ\text{C}$) is achieved for input power of 250 mW. At this input power, the maximum temperature in the stimulator is 70°C .

The specifications of the stimulators used in the experiments are given in Table 3.2. Circular PZT stimulators (P1/P4) are fabricated by ultrasonic micromachining of the piezoelectric elements from a PZT-5A plate (Fig. 3.3) [Li06]. The fabrication of piezoelectric stimulators is a two step process. A negative image of the desired pattern is micromachined on a stainless steel substrate using micro electro-discharge machining. The pattern formed is then transferred to the PZT-5A plate using ultrasonic machining with the help of tungsten carbide abrasive slurry. The plate is then flipped over and lapped from behind to release the pattern imprinted by the steel tool. A 50 nm thick titanium layer and a 500 nm thick gold metal layer are sputtered onto the PZT discs to form the electrodes. Thin copper wires (gauge ≈ 38 , length ≈ 40 cm, resistance $\approx 0.2 \Omega$)

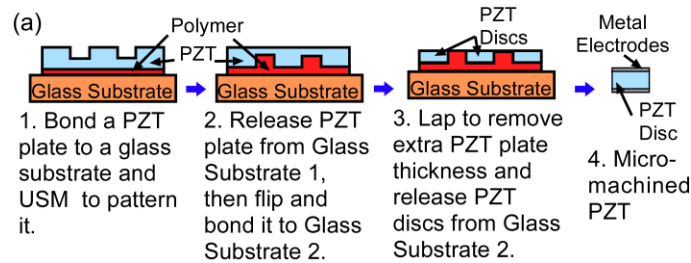


Figure 3.3: Ultrasonic machining for piezothermal stimulators.

are connected to the PZT discs by using conductive epoxy followed by an insulating layer of non-conductive epoxy.

The rectangular PZT stimulators (P2/P3) are made by dicing a 0.127 mm thick PZT-5A plate into the required dimensions. The electrical connections are provided by connecting copper wires (gauge ≈ 44) using conductive epoxy followed by a coating of non conductive epoxy.

3.2. Experimental results

Section 3.2.1 describes the experiments performed to evaluate suitable operating frequencies for the piezothermal stimulators. Section 3.2.2 describes the thermal stimulation results on GJB, Madagascar hissing roaches and GDB.

3.2.1. Characterization of Piezothermal Stimulators

The fabricated stimulators were experimentally evaluated prior to implantation. The voltage and current across the PZT element was measured using an Agilent DSO6014A oscilloscope and Tektronix CT1 (1 GHz) current probe respectively. The power dissipated by the PZT is given by:

$$P_c = V_{rms} I_{rms} \cos(\varphi) \quad (3.1)$$

where I is the current flowing through PZT, V is the drive voltage and φ is the phase difference between the current and the drive voltage. The temperatures in the experiments were measured using a K-type thermocouple read using HH506A multilogger thermometer.

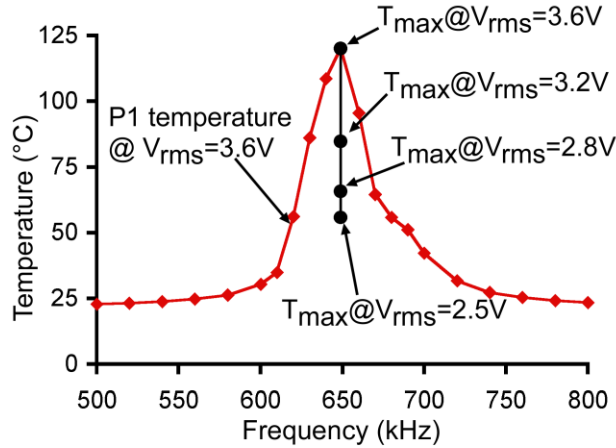


Figure 3.4: Variation of the steady state temperature attained by the piezothermal stimulator as a function of frequency when bonded to the elytra of the beetle. The temperature variation with the input RMS voltage is also plotted.

The experiments were carried out using PZT-5A heater (P1) bonded to an elytra of a beetle carcass. The existence of an optimal operating frequency for P1 is evident from the peak in Fig. 3.4. This frequency corresponds to the resonance frequency (650 kHz) of the structure (PZT bonded to beetle) measured using the impedance analyzer (Agilent 4395A). The frequency at which the maximum temperature (650 kHz) attained was then further used to study the steady state response of the piezothermal stimulator at varying input voltages (Fig. 3.4). It was thus determined that at this frequency, P1 achieved a thermal efficiency of $0.93^{\circ}\text{C}/\text{mW}$.

3.2.2. Control of insect locomotion

3.2.2.1. Experiments on green June beetles

The GJB has active flight behavior and appreciable load capacity, which are appealing characteristics for transporting sensor platforms [Dom88]. It has been observed that the head of the beetle is the most sensitive location for thermal stimulation,

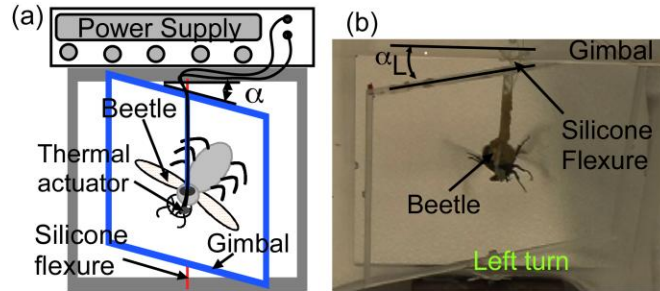


Figure 3.5: (a) Schematic of the experimental setup used in characterizing the angle turned by the beetle. (b) Photograph of beetle turning towards left side due to actuation on right side.

particularly in the vicinity of the antennae [Gul04]. Hence, in these experiments, the thermal stimulators are attached or implanted near the antennae of the beetles.

The response of the beetles to thermal stimulation was quantified by attaching them to a custom fabricated gimbal with an acrylic frame and silicone flexures (Fig. 3.5a). The gimbal was designed to minimize resistance to rotation about its axis, while constraining other the degrees of freedom. The torsional stiffness of the silicone flexures was experimentally measured at 68.7 mN-mm/rad. The microstimulators were mounted in close vicinity of the two antennae of the beetle.

The performance of P3 PZT stimulators ($1 \times 0.5 \times 0.127 \text{ mm}^3$) was compared with that of a resistive stimulator. These ‘V’-shaped Ni foil stimulators (R1) of size $4 \times 1.3 \times 0.05 \text{ mm}^3$ were fabricated using photochemical etching process (Fotofab Corporation, Chicago, Illinois, USA). The stimulators were bonded to the beetle using epoxy to prevent being dislodged by the beetle. An AC function generator (HP 33520A) was used to actuate the PZT stimulators. A DC power supply (HP E3630A) was used to actuate the resistive stimulators. The stimulators, P3, were actuated at the resonance frequency (1.9 MHz) for maximum thermal efficiency.

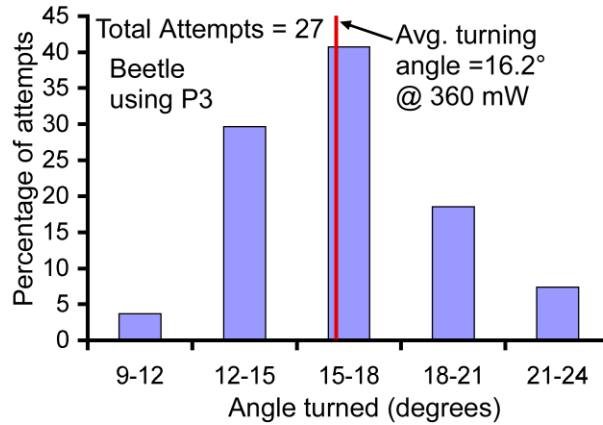


Figure 3.6: Turning characterization for P3 in GJB. P3 produces an average turning of 16° at 360 mW.

Experimental results confirmed the aversion of beetle to thermal stimulation. The micro-stimulators, R1 and P3 repeatedly demonstrated flight initiation and directional control of the GJB. The beetle turned away from the direction of the actuated stimulator (Fig. 3.5b). An applied power of 800 mW across R1, resulted in the stimulation of the beetle. This confirmed that the thermal response was indeed the cause of stimulation. The beetle turned away from the side being stimulated by approximately 15° (0.26 rad), which resulted in a torque of 18 mN-mm. However, stimulator P3 required only 360 mW of power for flight initiation and direction control. The beetles were stimulated 34 times with an overall success rate of 80%. For this power, the beetle rotated away from the side being stimulated by an average 16.2° which demanded a torque of 19.2 mN-mm. The statistical results for repeated actuation of P3 are plotted in Fig. 3.6.

3.2.2.2. Experiments on Madagascar hissing roaches

In order to show the versatility of the proposed technique, experiments were also performed on Madagascar hissing roaches. The roaches are considered to be one of the

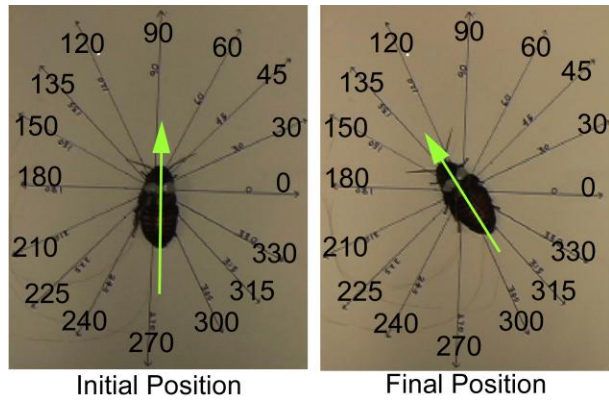


Figure 3.7: Photograph of the roach turning towards its left side due to the actuation of P2 on the right side. The angle turned was characterized by positioning the roach on the paper marked with angles.

most primitive creatures on earth and are known to be immune to radiation making it an ideal candidate for micro vehicle applications [Big08]. Two sets of PZT stimulators, P1 (3.2 mm diameter and 0.191 mm thickness) and P2 (3x1x0.127 mm³), were investigated for the experiments on roaches.

The roaches were tested with two PZT stimulators implanted on either side of the thorax, but near the head. The turning responses were characterized by performing the

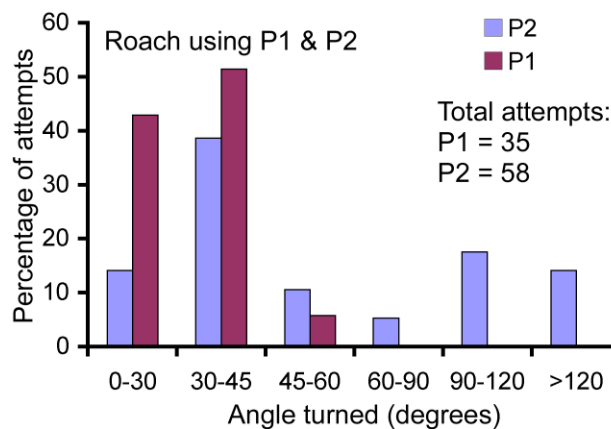


Figure 3.8: Turning characterization for P1 and P2 in roaches. Statistical variation of angle turned indicates that maximum count occurs in the range of 30°-45° per actuation at 330 mW.

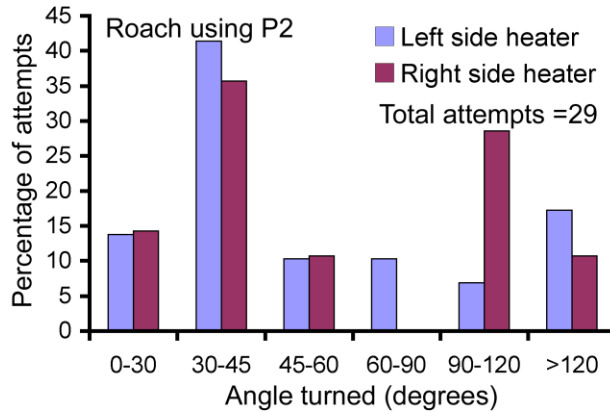


Figure 3.9: Left and right turning characteristics for P2 in roaches. The behavior was statistically symmetrical.

tests on a surface marked with angles (Fig. 3.7). An AC function generator (Agilent 33250A) was used to actuate P1 and P2 stimulators at their respective resonance frequencies of 4.2 MHz and 5.5 MHz, respectively.

Figure 3.7 shows an exemplary consequence of stimulating the right side of the roach. Like beetles, the roach also moves away from the activated stimulator. The minimum power required for the actuation using P1 was about 550 mW; P2 required only about 330 mW, mainly due to its smaller thermal mass. About 60 trials were carried out using P1 and 62 trials using P2. P2 stimulators showed superior direction control (93.5% of total attempts were successful as compared to 60% for P1). This was also attributed to smaller size of P2 which makes localized heating possible. The angle turned during each stimulation event was characterized for both the PZT heaters (Fig. 3.8). The roaches turn about 30°-45° per stimulation. As expected, the left and right turns were statistically similar (Fig. 3.9).

The variation in the time needed for actuation with applied power was studied using P2. On average, about 20 seconds were needed for stimulation at an input power of

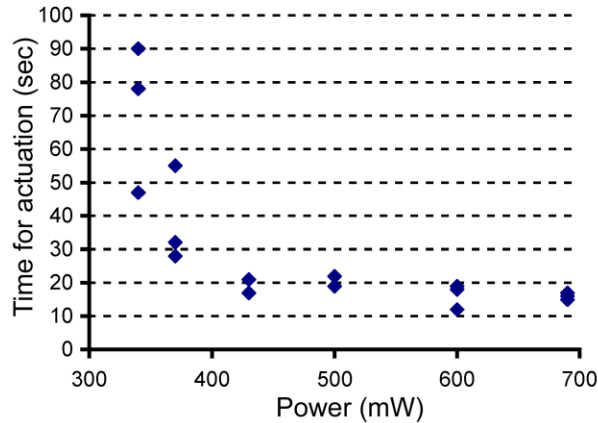


Figure 3.10: Variation of time required for actuation of roaches with input power. As expected, the actuation time decreased with increase in the input power.

400 mW (Fig. 3.10). It was observed that the time for actuation generally decreased as the input power increased.

3.2.2.3. Experiments on green diving beetles

Experiments were conducted on GDB to show the applicability of thermal stimulation for locomotion control of aquatic insects. The GDB are oval in shape and are generally $\frac{3}{4}$ inches long. The GDB have oar shaped rear legs with hair like structures to assist in swimming. Unlike other aquatic insects, GDB generally travel on or near the surface of water.

The piezothermal stimulators were implanted in the thorax of the beetles. The locomotion of the beetles was monitored within a water-filled container. The piezothermal stimulators, P4 (diameter = 200 μm and thickness \approx 40-50 μm), were used in these experiments because GDBs were smaller in size compared to other two types of insects. Because of the smaller size of these stimulators, the impedance is relatively high. This limits the current flowing through the stimulator, particularly at lower frequencies

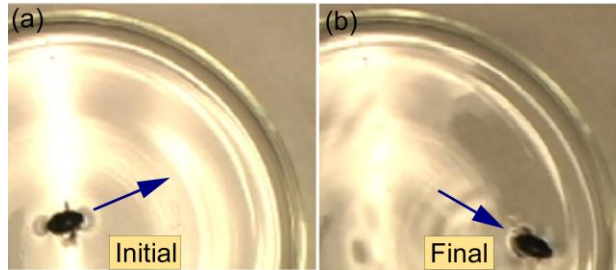


Figure 3.11: Photograph of the green diving beetle turning towards its right side due to stimulation on the left side. The arrow indicates the orientation of the GDB before and after stimulation.

which in turn limits the heat generated by these stimulators at a given voltage amplitude. The maximum voltage that can be applied to these stimulators is limited by the depoling electric field of the PZT (7kV/cm for PZT-5A) and the function generator. Hence, in order to generate enough heat, the stimulators were operated at a higher order resonance mode (44-47 MHz). Within a water ambient, the average input power required for stimulation is 100 mW.

Figure 3.11 shows a sample response of a GDB to the actuation of the left side stimulator. Like the other insects, the GDB turn away from the thermal stimulation. The

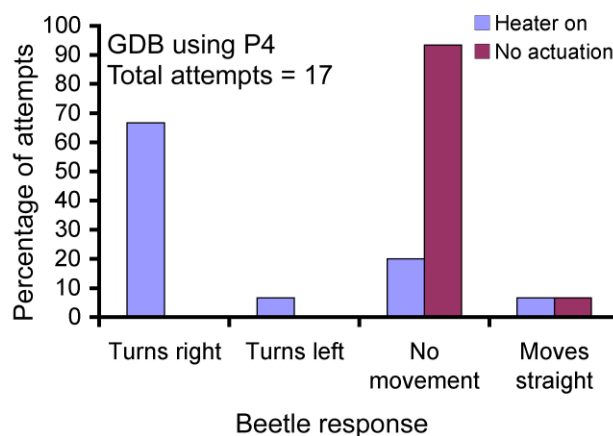


Figure 3.12: Statistical variation in the response of the green diving beetle with and without thermal stimulation.

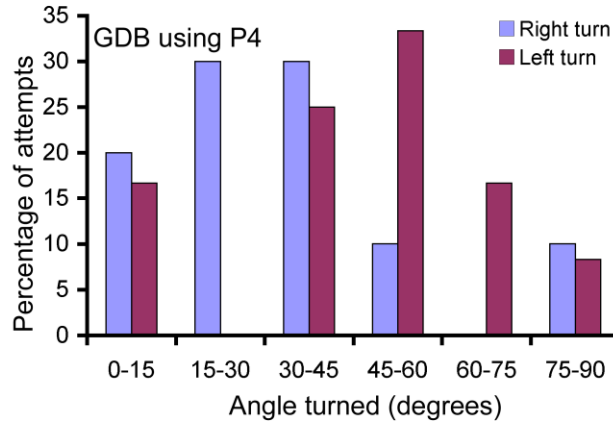


Figure 3.13: Left and right turning characteristics for P4 in green diving beetles. The green diving beetles turn about 15°-60° per actuation.

statistical variation in the response of the GDB with and without thermal stimulation is shown in Fig. 3.12. The GDB moves straight for 90% of attempts when there is no stimulation. The GDB turns in 68% of the attempts when a stimulator is actuated. The angle of the turns is typically 15°-60° (Fig. 3.13).

3.3. Discussion

3.3.1. Scaling of piezothermal stimulators

Reducing the size of the stimulator is attractive because this reduces the total heat delivered in each stimulation and also localizes the stimulation for better directional response. It also reduces the power required for achieving the target temperature of 43°C. However, the smallest size of the stimulator is limited by the maximum allowable temperature in the PZT stimulator. Even though the stimulator size is scaled down, the thickness of the connecting wire and insulating epoxy remain constant for reliable operation of the device. Hence, the maximum temperature within the stimulator increases for a given interface temperature as we shrink the size of the stimulator. The

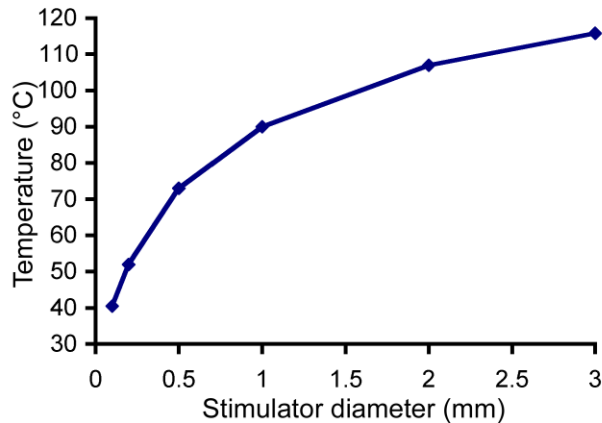


Figure 3.14: The average temperature at the tissue-stimulator interface for different sizes of the piezothermal stimulator when the maximum temperature in the stimulator is 450 K. Simulations suggest that for diameter <math>< 130 \mu\text{m}</math>, the interface temperature falls below 43°C.

maximum allowable temperature in the PZT element is limited to 50% of the Curie temperature. For PZT-5A, the temperature is limited to 450 K (for $T_{\text{curie}} = 350^\circ\text{C}$).

Finite element simulations were performed for different diameters of the 125 μm -thick circular piezothermal stimulator to determine the average temperature at the tissue interface when the maximum temperature in the stimulator reaches 450 K. The properties of the heaters, connecting wires and insulating epoxy used in the simulations are listed in Table 3.1. Figure 3.14 suggests the minimum diameter is 130 μm , below which the temperature at the stimulator tissue interface falls below 43°C.

3.3.2. Battery

Thermal stimulation of insects require higher current (>50 mA) as compared to other methods such as electroneural stimulation. Further, the insects have a maximum payload capacity of 2 g [Yag97]. Hence, in order for system level implementation of the proposed technique, a light-weight and high current output battery is required. The

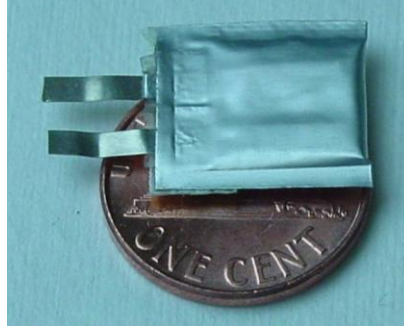


Figure.3.15: Photograph of the commercially available ultra-light weight lithium ion battery.

ultralight lithium ion battery is believed to be most suitable for this application (e.g. PGEB20151, Powerstream Inc.) (Fig. 3.15). These batteries are $2 \times 15 \times 15 \text{ mm}^3$ in size and weigh about 0.43 g. The maximum discharge capacity is 80 mA whereas the rated capacity is 10 mAh. The batteries have a nominal voltage of 3.7 V. Hence 2-3 batteries can be connected in series to generate the required voltage for stimulation. For an average stimulation power of 400 mW and stimulation time of 20 seconds, a pair of batteries can be used for about 32 stimulations, which is potentially the limiting constraint of this approach.

3.4. Conclusions

The feasibility of locomotion control of insects using thermal stimulators for micro vehicle applications such as military surveillance and environmental monitoring was demonstrated. Experiments conducted on GJB, Madagascar hissing roaches and GDB suggested the feasibility of microthermal stimulation as a widely applicable method for locomotion initiation and directional control. Further, piezothermal stimulation especially near the resonance frequency was observed to be more power efficient. The

PZT based stimulators achieved a thermal efficiency of $0.93^{\circ}\text{C}/\text{mW}$ when bonded to elytra of beetle. A finite element model was used to estimate the required power for the beetle-stimulator interface temperature to be 43°C (required for stimulation). The piezothermal stimulation showed an overall success rate of 80%, 93.5%, and 68% on GJB, Madagascar hissing roaches, and GDB, respectively. On average, thermal stimulation resulted in an angle turn of about 15° - 18° on GJB, 30° - 45° on the roaches and 15° - 60° on GDB. The corresponding average input power was 360 mW, 330 mW and 100 mW for GJB, roach and GDB, respectively. Even though electroneural stimulation is better than the thermal stimulation in terms of input power and response time, the thermal stimulation is believed to provide a generalized stimulation method for locomotion control of wide variety of insects without need for detailed knowledge of insect physiology.

CHAPTER 4

BIOPSY NEEDLE TRACT CAUTERIZATION AND *IN-SITU* CAUTERIZATION MONITORING USING EMBEDDED PIEZOCERAMIC MICROHEATERS

This chapter addresses the feasibility of biopsy needle tract cauterization and *in-situ* cauterization monitoring using PZT-5A based microheaters embedded into the wall of biopsy needles [Vis04, Vis05]. Circular piezoceramic heaters of 200 μm diameter and 70-80 μm thickness are used to evaluate these functions. The cauterization and cauterization monitoring experiments, performed on the porcine tissue samples, are described. Section 4.1.1 describes the simulation model used for determining the temperature profile in the surrounding tissues. An analytical model for determining the resonance frequency shift due to tissue cauterization is described in Section 4.1.2. The design, fabrication and integration of the piezoceramic microheaters with the biopsy needles are described in Section 4.2. Section 4.3 describes the experimental results for needle tract cauterization and cauterization monitoring using the proposed biopsy tool.

4.1. Simulation model

4.1.1. *Tissue ablation model*

A 3D finite element model has been developed to determine the temperature profile generated by embedded heaters in biological tissue surrounding the biopsy needle.

Pennes' bioheat transfer model is used to model the heat transfer in tissues [Pen48]. The model is given by:

$$\rho_t c_t \frac{\partial T}{\partial t} = \nabla \cdot k \nabla T + \rho_b c_b \omega_b (T_b - T) + \dot{q} \quad (4.1)$$

where ρ_t is the density, c_t is the specific heat capacity, k is the thermal conductivity, T is the temperature, ρ_b is the density of blood, c_b is the specific heat capacity of blood, ω_b is the perfusion rate of the blood, T_b is the arterial blood temperature and \dot{q} is the heat generation rate per unit volume due to ultrasound applicator. The perfusion rate accounts for the cooling due to blood flow in the surrounding fluid.

For the structure used in this work, PZT heaters are significantly smaller than the size of the needle. Hence it is permissible to model the heaters as small spherical sources. The heat generation rate from the PZT heater is given by [Ski98]:

$$\dot{q} = \frac{2\alpha I_s r_0^2}{r^2} e^{-2\alpha(r-r_0)} \quad (4.2)$$

where α is the ultrasound absorption coefficient ($\text{Np} \cdot \text{m}^{-1}$), I_s is the ultrasound intensity along the surface of the transducer ($\text{W} \cdot \text{m}^{-2}$), r is the radial distance from the center of the transducer and r_0 is the radius of the transducer. Due to inefficiencies in the transducer, not all the electrical energy provided to it is converted into acoustic energy. This unconverted energy is dissipated, within the transducer as heat. For a given transducer efficiency, ν , the heat generation rate per unit volume within the transducer is given by:

$$\dot{q}_{app} = \left(\frac{1-\nu}{\nu} \right) \frac{3I_s}{r_0} \quad (4.3)$$

The simulations were performed using the bioheat equation model in COMSOL Multiphysics®. Three designs were considered in the simulations: single PZT disc, PZT

array (4 discs) with no gap between elements, and PZT array with 0.5 mm gap between elements (Fig. 4.1). All these models consisted of four major regions: PZT heater, epoxy surrounding the PZT heater, biopsy needle and biological tissue. The biological tissue was modeled by a 5 cm diameter sphere surrounding the needle. The 20 gauge needle used in the experiments was modeled by a semi-circular cylinder with inner and outer radii of 300 μm and 450 μm , respectively. The length of the needle was 6 cm. For the single PZT element design, a hole of 135 μm depth and 300 μm diameter modeled the cavity in which the PZT heater was located. For the arrayed element design, a slot of $2000 \times 300 \times 135 \mu\text{m}^3$ was used. The material properties used in the simulations are listed in Table 4.1.

The cooling due to blood flow was considered only in the biological tissue region. The heat generation rate given by equation 4.2 was used in the epoxy, needle and tissue region. The heat generation rate given by equation 4.3 was used in the PZT region. The outer surface of the tissue was assumed to be at 310 K. The base of the needle extending outside the tissue region was assumed to be at 300 K. For a PZT transducer operating at

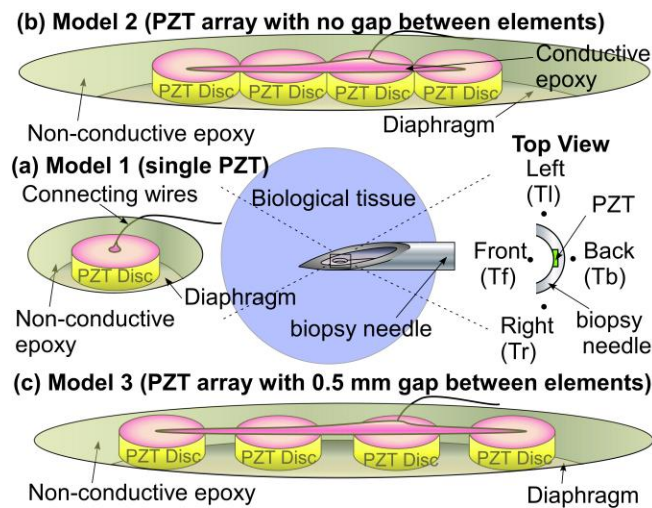


Figure 4.1: Schematic model of various biopsy tool designs considered in the simulation.

Table 4.1: Material properties used in the simulations.

Density of tissue	1050 kg.m ⁻³
Thermal conductivity of tissue	0.51 W.m ⁻¹ .K ⁻¹
Specific heat capacity of tissue	3639 J.kg ⁻¹ .K ⁻¹
Density of blood	1000 kg.m ⁻³
Specific heat capacity of blood	4180 J.kg ⁻¹ .K ⁻¹
Perfusion rate of blood	15x10 ⁻³ s ⁻¹
Arterial blood temperature	310 K
Thermal conductivity of needle	44.5 W.m ⁻¹ .K ⁻¹
Density of needle	7850 kg.m ⁻³
Specific heat capacity of needle	475 J.kg ⁻¹ .K ⁻¹
Thermal conductivity of epoxy	1.7 W.m ⁻¹ .K ⁻¹
Density of epoxy	1060 kg.m ⁻³
Specific heat capacity of epoxy	1000 J.kg ⁻¹ .K ⁻¹
Thermal conductivity of PZT	1 W.m ⁻¹ .K ⁻¹
Density of PZT	7700 kg.m ⁻³
Specific heat capacity of PZT	350 J.kg ⁻¹ .K ⁻¹

a frequency of 7 MHz with an input power level of 50 W/cm², the transducer efficiency as identified in the context of equation 4.3 was determined to be 0.52 in [Tyr02]. Hence, in the present simulations, with transducer frequency of 10 MHz and input power level of 90 Wcm⁻², the transducer efficiency was assumed to be 0.52. Figure 4.2 compares the simulation results for the variation of temperature as a function of distance from the needle. Simulations suggest that for an ultrasound surface intensity of 90 W.cm⁻², maximum temperature rise is attained by the PZT array with no gap between the elements. The ultrasound surface intensity is directly proportional to the drive voltage applied to the electrodes of the PZT elements. Hence, in the experiments, biopsy needles with an embedded array of four PZT discs with no gap between the elements are used.

4.1.2. Model for estimating resonance frequency shift due to cauterization

A modified Butterworth-Van-Dyke circuit model is used to determine the

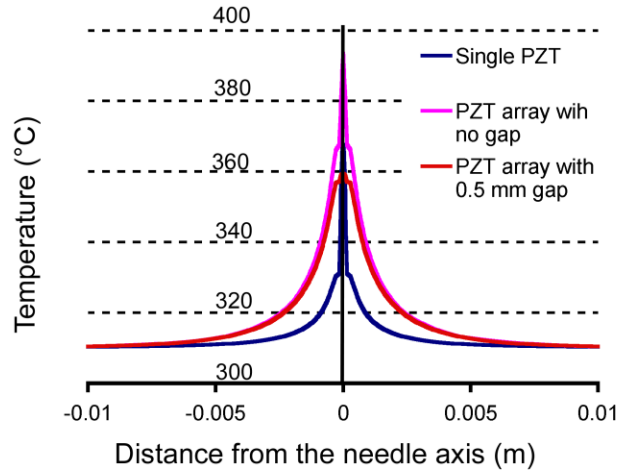


Figure 4.2: Finite element simulation results for the variation of temperature as a function of distance from the needle for the three designs for ultrasound intensity, $I_s = 90 \text{ W.cm}^{-2}$.

variation in impedance characteristics of the PZT element around the resonance frequency, when it is in air, and in tissue before and after cauterization [Pan06, Ban99]. The resonance frequency and the magnitude of the electromechanical impedance of a PZT-embedded structure at resonance frequency depend on the density, elastic modulus and loss factor of the surrounding medium. The elastic modulus and loss factor of the tissue increase due to ablation, thereby providing a method for monitoring tissue cauterization [Kis04].

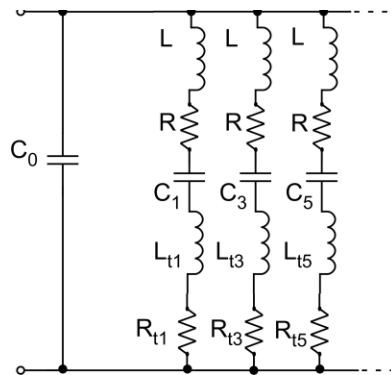


Figure 4.3: Modified Butterworth Van Dyke (BVD) equivalent circuit for predicting the frequency shift in resonance due to tissue cauterization.

Table 4.2. Material properties used in the BVD analytical model [Pan06].

Normal tissue	
Density, ρ_t	1054 kg.m ⁻³
Storage modulus, G	550 Pa
Loss factor, η	13 Pa.s
Cauterized tissue	
Storage modulus, G'	37000 Pa
Loss factor, η	230 Pa.s
PZT-5A	
Young's modulus, E_0	5.2x10 ¹⁰ Pa
Density, ρ_0	7800 kg.m ⁻³
Coupling constant, K_t	0.72
Relative dielectric constant	1800

Figure 4.3 shows the schematic of the modified Butterworth-Van-Dyke circuit. The circuit model consists of a static branch (C_0). The static branch describes the fixed dielectric capacitance of the PZT element. In parallel with this branch are an infinite number of motional branches (R_n, L_n, C_n), each corresponding to different resonance modes. The motional branches determine the resonance characteristics such as the resonance frequency and quality factor of various resonance modes. The various resistors, capacitors and inductors in the circuit are given by [Li07, Pan06]:

$$C_0 = \frac{\epsilon A}{t_0} \quad (4.4)$$

$$L = \frac{1}{4\pi^2 f_{a1}^2 c_1} \quad (4.5)$$

$$C_n = \frac{8k_t^2/n^2\pi^2}{1-8k_t^2/n^2\pi^2} C_0 \quad (4.6)$$

$$R = \frac{\eta_0}{\rho_0 v_0^2 c_1} \left(\frac{f}{f_{a1}} \right) \quad (4.7)$$

where k_t is the electro-mechanical coupling constant, η_0 is the viscosity of PZT layer, ρ_0

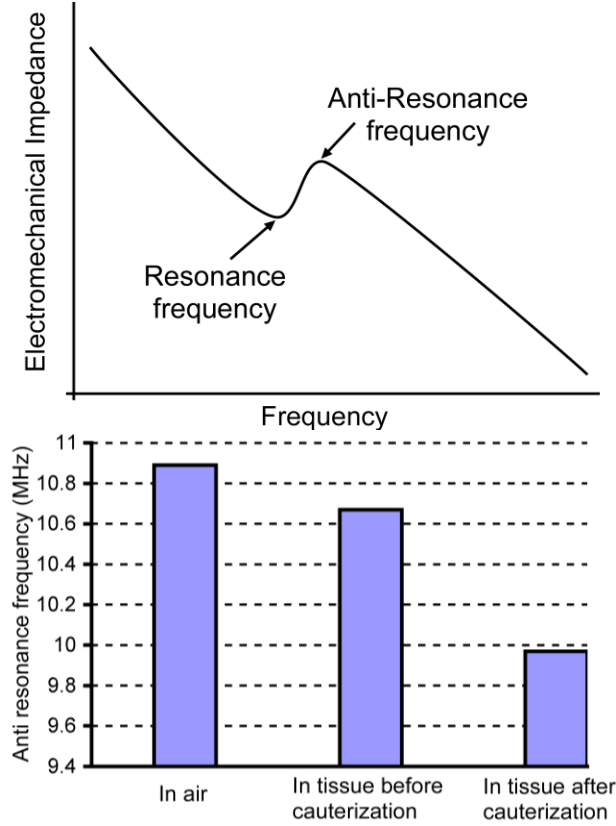


Figure 4.4: (a) Schematic of the impedance curve of the PZT around the resonance frequency. (b) Analytical modeling results for the variation of anti-resonance frequency when the biopsy needle tip is in air, and in tissue before and after cauterization.

is the density of PZT, A is the area of PZT element, v_0 is the acoustic velocity in PZT, t_0 is the PZT element thickness and ϵ is the dielectric permittivity in PZT. The fundamental resonance, f_m , (minimum impedance) and anti-resonance (maximum impedance) frequency, f_{an} , are given by:

$$f_{r1} = \frac{1}{2\pi\sqrt{LC_1}} \quad (4.8)$$

$$f_{a1} = \sqrt{1 + \frac{C_1}{C_0}} f_{r1} \quad (4.9)$$

The effect of tissue loading is modeled by adding a resistor R_m and inductor L_m to the motional branch of the circuit. For a semi-infinite viscoelastic medium R_m and L_m are given by [Ban99]:

$$R_m = \frac{n\pi}{4k_t^2 \omega C_0 Z_q} \left[\frac{\rho_t \left(\sqrt{G} + G' \right)}{2} \right]^{0.5} \quad (4.10)$$

$$L_m = \frac{n\pi}{4k_t^2 \omega C_0 Z_q} \left[\frac{\rho_t \left(\sqrt{G} - G' \right)}{2} \right]^{0.5} \quad (4.11)$$

$$Z_q = \sqrt{E_0 \rho_0} \quad (4.12)$$

$$G = G' + i\eta\omega \quad (4.13)$$

where E_0 is the young's modulus of PZT, ρ_t is the tissue density, ω is the operation frequency, G' is the tissue storage modulus, η is the loss factor in tissue and Z_q is the PZT acoustic impedance. Table 4.2 lists the material properties used in the model. Because the fundamental radial resonance mode of the PZT element is used in the experiments, the variation of the anti-resonance frequency of this mode is calculated. The variation of the anti-resonance frequency when the biopsy needle tip is in air, in tissue before cauterization and in tissue after cauterization is shown in Fig. 4.4. Analytical modeling results suggest that the fundamental anti-resonance frequency decreases by 0.9 MHz after cauterization.

4.2. Device design and fabrication

The schematic of the proposed biopsy tool design is shown in Fig. 4.5. The PZT discs were fabricated from PZT-5A material as it has a Curie temperature of 350°C,

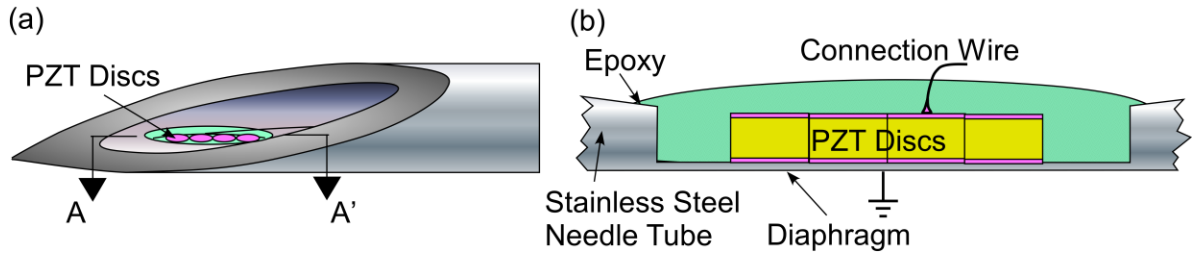


Figure 4.5: (a) Schematic diagram of the proposed biopsy tool. (b) Schematic of the cross-section view of the proposed biopsy tool.

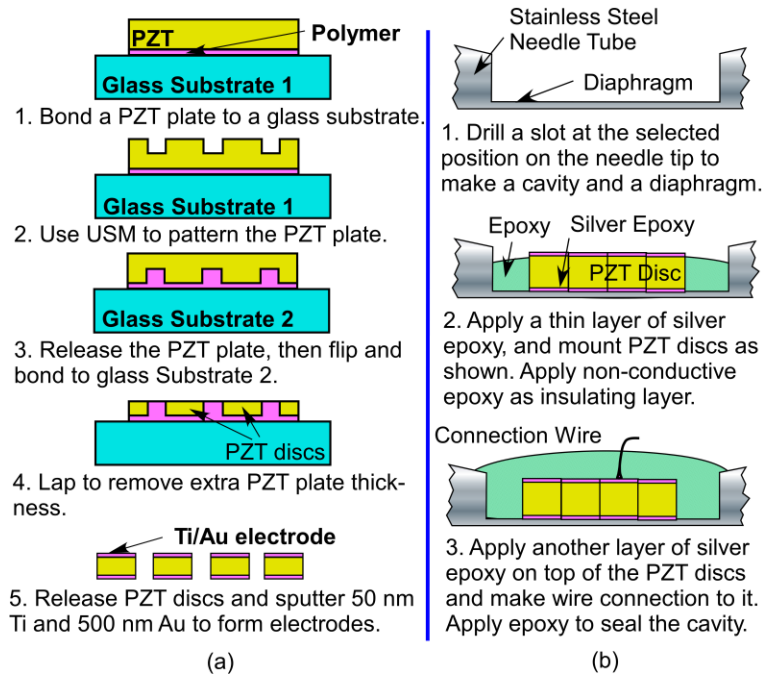


Figure 4.6: (a) Ultrasonic machining process for PZT disc fabrication [Li06]. (b) PZT disc integration procedure for the biopsy tool.

which is greater than the target temperature of 70-100°C ($\Delta T=33-63^\circ\text{C}$). Circular PZT elements were used because for a given volume of the device, these generate higher temperature rise per unit voltage as compared to square and rectangular devices (as described in Chapter 2).

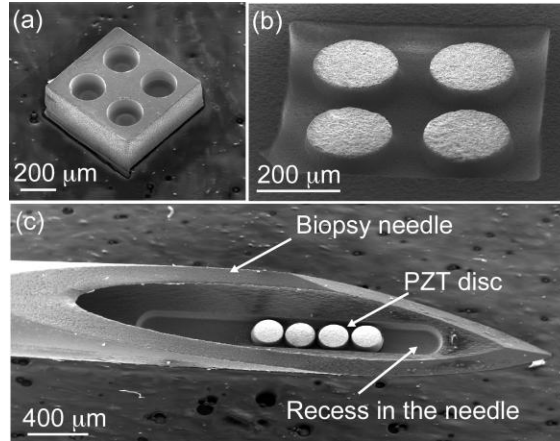


Figure 4.7: (a) SEM image of the tool used in the μ -USM process. (b) SEM image of the pattern transferred onto a PZT substrate using the μ -USM process. (c) SEM image of the PZT discs assembled into a recess made on the wall of a biopsy needle using μ -EDM.

The PZT discs (of diameter 200 μm and thickness 70-80 μm) were fabricated using batch mode micro ultrasonic machining process (μ -USM) [Li06] (Fig. 4.6a). The USM tools were fabricated using micro electro-discharge machining (μ -EDM) of a stainless steel substrate. Figure 4.7a shows the SEM image of a fabricated USM tool. The patterns were then transferred to the PZT-5A plate using USM with tungsten carbide slurry (Fig. 4.7b). Tungsten carbide powders of diameter 0.5-0.99 μm were used in these machining steps (Alldyne Powder Technologies, Huntsville, Al). The patterned PZT discs were released by lapping the substrate from behind. A 50 nm thick titanium layer and a 500 nm thick gold metal layer were sputtered onto the PZT discs to form the electrodes. The sides of the discs were covered with a thin layer of photoresist to prevent shorting of the two electrodes during sputtering.

The PZT discs were integrated into a recess ($2000 \times 300 \times 135 \mu\text{m}^3$) cut into 20-gauge stainless steel needles using μ -EDM (Becton Dickinson, Franklin lakes, NJ, Model #: 305175) (Fig. 4.6b). Because of the circular cross-section of the needle, the thickness of the resulting diaphragm was between 10 and 36 μm for a 20 gauge needle. The

variation in the thickness of the diaphragm was less than 2 μm . This prevents the discs from blocking the path for acquiring tissues during the biopsy process. The thin diaphragm left behind in the wall of the needle after the formation of recess also reduces the heat loss due to conduction along the needle. The PZT discs were bonded to the biopsy needle using conductive epoxy. Figure 4.7c shows the photograph of a biopsy needle with four PZT discs integrated into the recess. The PZT discs were surrounded by non-conductive epoxy in order to provide a highly damping medium for heat generation as well as reduce heat loss due to conduction. A flexible copper wire within the lumen provided power to the top electrode while the needle provided the ground return path. The copper wire was bonded using a layer of conductive epoxy.

4.3. Experimental results

4.3.1. Tissue cauterization

The temperature profile generated by the biopsy tool was measured at two resonance modes: the radial mode (10.3 MHz) and the thickness mode (22.3 MHz). The diameter and thickness of each of the four PZT discs was about 200 μm and 80 μm , respectively. The PZT discs had a low quality factor because of the high damping provided by the surrounding epoxy. Hence, there was only a single combined peak observed in the electromechanical impedance curve around the radial mode and thickness mode resonance frequencies. Depending on the resonance mode used for actuation, the PZT discs were actuated by sinusoidal waves at the combined resonance peak frequency of either 10.3 MHz or 22.3 MHz. The sinusoidal waves were generated using a function generator and were amplified using a power amplifier. The temperature was measured

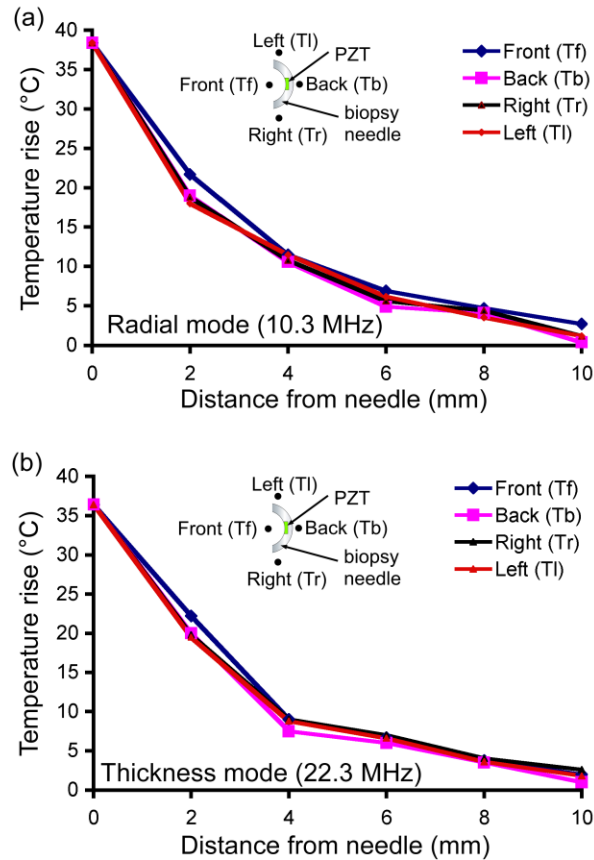


Figure 4.8: Variation of temperature as a function of direction and distance from the needle for (a) radial mode and (b) thickness mode resonances. The temperature distribution is similar in all directions for both resonance modes.

using a K-type thermocouple read using a digital thermometer. The experiments were performed by inserting the needle into porcine tissue samples. Figures 4.8a and 4.8b show the temperature measured at different distances and directions from a needle for the radial and thickness mode resonances, respectively. The temperature distribution was similar in all directions for both resonance modes. This indicated uniform cauterization in the surrounding region.

The temperature rise at the surface of the needle, in both resonance modes, for varying input voltage is shown in Fig. 4.9a. The needle surface exceeds the minimum target temperature rise of 33°C for an applied voltage of 17 V_{RMS} and 14 V_{RMS} for radial

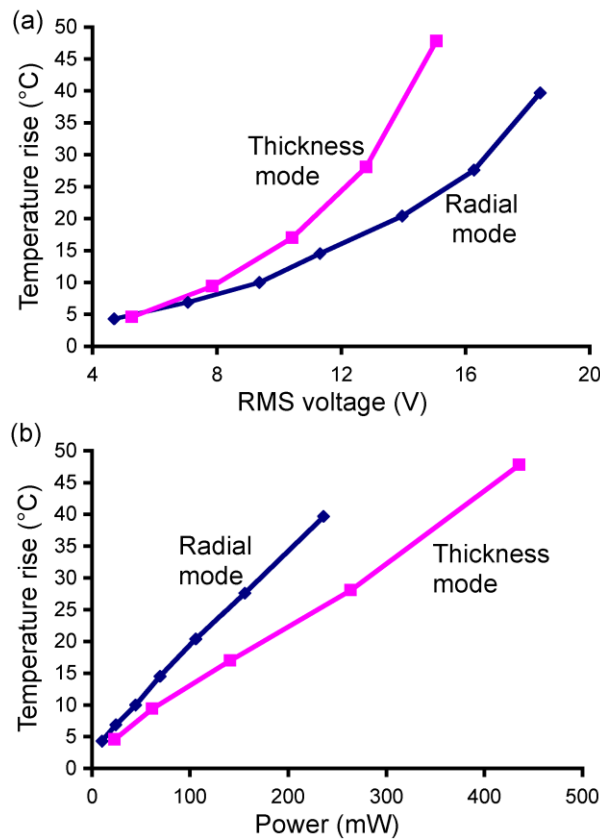


Figure 4.9: Variation in the temperature generated at the surface of the needle for various (a) input voltages and (b) input power.

and thickness mode, respectively. This difference is believed to be mainly due to the higher electromechanical impedance of the PZT device at lower operating frequency. Figure 4.9b compares the temperature rise generated at the surface of the needle for various input power for the two modes. The plot suggests that the target temperature rise of 33°C was achieved for input power of 236 mW and 325 mW, respectively. Figure 4.10 shows the photographs of the cauterized porcine tissue for an applied voltage of 14V_{RMS} at 22.3 MHz. The radius of tissue cauterization is 1-1.25 mm beyond the perimeter of needle. This suggests minimal damage was sustained by the surrounding healthy tissue. This is desired as for this application it is only necessary to cauterize the tissue layer in contact with the needle.

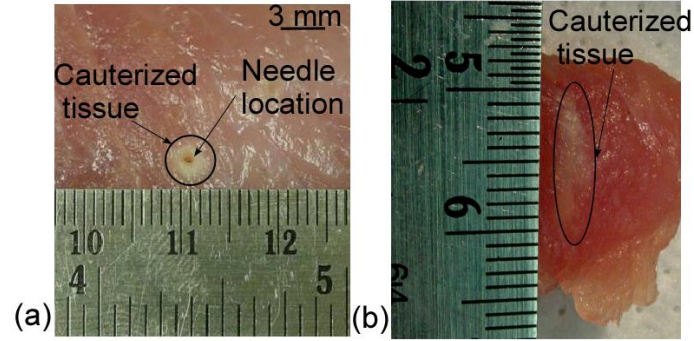


Figure 4.10: Photograph of (a) top view and (b) cross section of the cauterized porcine tissue. The radius of cauterization beyond perimeter of needle was 1-1.25 mm for an input RMS voltage of 14 V.

4.3.2. Sensing of the tissue cauterization

Cauterization experiments were conducted by inserting the biopsy needle into porcine tissue samples. The porcine tissue sample was cauterized by actuating the PZT discs with an RMS voltage of 14 V at the fundamental anti-resonance frequency of 9.6 MHz. The impedance characteristics of the PZT discs were measured using Agilent 4395A impedance analyzer. All impedance measurements were conducted at room temperature unless stated otherwise.

Figure 4.11 shows the variation of the impedance characteristics of the PZT transducer for the following three cases: biopsy needle tip in air, in tissue before and after cauterization. The fundamental anti-resonance frequency (f_{a1}) of the PZT discs was used for monitoring of cauterization. When the biopsy needle was inserted into the tissue, f_{a1} dropped from 9.66 MHz to 9.61 MHz. After cauterization, f_{a1} and the impedance magnitude decreased further by 0.6 MHz and 900 ohms, respectively (Fig. 4.11). This decrease matches to that predicted by the analytical model and can be used to monitor the progress of cauterization.

The variation in f_{a1} was also measured with temperature varied in the range for

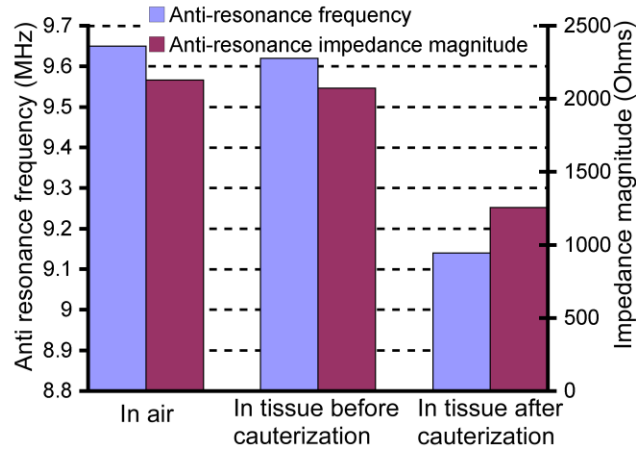


Figure 4.11: Measured variation, using Agilent 4395A impedance analyzer, of anti-resonance frequency and peak impedance magnitude, when a needle was in air, in tissue before and after cauterization (all at room temperature).

cauterization while the needle tip stayed in air. Even though f_{a1} decreased (from 11.92 MHz to 11.38 MHz) with increasing temperature (from 22°C to 78°C), it was observed that f_{a1} returned to its initial value when the needle was cooled down to room temperature (Fig.4.12). As the readings in Fig. 4.11 were all made at the same room temperature, additional correction is not necessary.

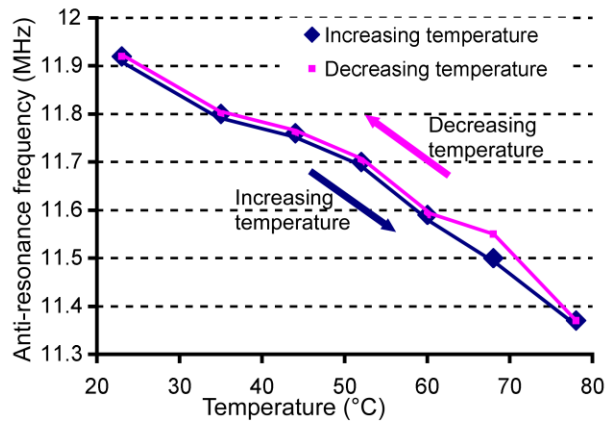


Figure 4.12: Measured variation of anti-resonance frequency with temperature in the range used for cauterization. The f_{a1} returned to the original value at the range of temperatures from body temperature to room temperature.

4.4. Conclusions

This chapter showed the feasibility of biopsy needle tract cauterization and cauterization monitoring using PZT heaters embedded into the wall of a biopsy needle. Finite element simulations suggested that a PZT array with no gap between the elements is most suitable for generating maximum temperature rise for a given drive voltage. An analytical model based on modified Butterworth-Van-Dyke circuit model suggested that the resonance frequency of the PZT element decreases when the tissue is cauterized. The PZT heaters generated the target temperature rise of 33 °C for an input power of <325 mW and a drive voltage of <17 V_{RMS}. The extent of tissue cauterization was <1.25 mm beyond the perimeter of the needle thereby ensuring minimum damage to the surrounding tissues. Cauterization of porcine tissue sample resulted in a decrease of 0.6 MHz in the resonance frequency and 900 ohms in the peak impedance magnitude, thereby providing a way to monitor the extent of cauterization. This approach bears significant promise in the long term for developing miniaturized servo-controlled cauterization procedure.

CHAPTER 5

THE ACTUATION AND SENSING INTERFACE CIRCUITS FOR BIOPSY NEEDLE TRACT CAUTERIZATION TOOL

Chapter 4 discussed the feasibility of using piezoceramic microheaters embedded in the wall of biopsy needles for needle tract cauterization. The use of these PZT heaters for *in-situ* cauterization monitoring was also discussed. However, this procedure required expensive and bulky equipment such as network analyzer for sensing of the cauterization. Such equipment may not be widely available and could potentially become a limiting factor for the accessibility of this technique. This chapter describes an approach to simplify the signal readout and heater actuation equipment, and make it an inexpensive and widely accessible technique. The method proposed here involves the design and fabrication of an interface circuit on a printed circuit board (PCB). Section 5.1 discusses the existing readout circuits available for resonance frequency measurement of the piezoelectric elements and the need for the proposed circuit. Section 5.2 describes the design of the proposed interface circuit for sensing of the cauterization and the PZT heater actuation. Section 5.3 describes PSpice[®] simulation results for the proposed circuit for sensing of the cauterization. Section 5.4 describes the details of the layout and fabrication of the interface circuits on a PCB. Preliminary experimental results from the assembled PCBs are described in Section 5.5.

5.1. Existing readout circuits for resonance frequency measurement

Past work on readout circuits for the resonance frequency measurement of piezoelectric elements has been mainly focused on quartz crystal microbalances. Most of the existing readout circuits can be classified into the following three categories based on their working principle [Eic99]: (1) Impulse excitation, (2) Phase-locked loop, and (3) Oscillators.

5.1.1. Impulse excitation

In this method, a voltage pulse is applied to the piezoelectric element [Eic99]. The response of the piezoelectric element is measured using known electrical impedance in series with it. This measured response is transformed into the frequency domain to obtain the impedance of the PZT element as a function of frequency. The resonance frequency is then obtained from the impedance curve. The main limitation is the difficulty in the generation of an ideal pulse. Also this method needs a computer or a microcontroller to record and obtain the frequency response.

5.1.2. Phase-locked loop

Another common circuit used for resonance frequency measurement is phase-locked loop [Fer96]. In this method, the output of a voltage controlled oscillator (VCO) is locked to the phase of a reference signal. The resonance frequency can be read directly from the VCO's output. This method is capable of producing very high frequency stability. However, it can measure only small shifts in resonance frequency.

5.1.3. Oscillators

Oscillator circuits are the most common method used for measuring the resonance frequency of piezoelectric devices. In this method, the piezoelectric devices are excited to stable oscillations at their resonance frequency. The resonance frequency is then obtained by determining the frequency of the output signal. Most oscillating circuits consist of an amplifier in a feedback loop. For generation of stable oscillations, the total phase shift in the feedback loop needs to be 360° . In addition, the closed loop gain should be ≥ 1 . The most common circuit used for this purpose is the Pierce oscillating circuit [Eic99]. This circuit uses an inverting amplifier which provides a phase shift of 180° . The remaining 180° phase shift is provided by the piezoelectric device, resistors and capacitors in the circuit. Further, the resistors and capacitors values are chosen such that the closed loop gain is ≥ 1 . The other types of oscillator circuits that have been used for this purpose are lever oscillators [Eic99] and emitter coupled oscillators [Eic99]. The advantage of this approach is that it is simple and inexpensive. This allows it to be easily integrated along with the sensor. However, this approach requires a high quality factor for the piezoelectric element. Since PZT inherently has a low quality factor (which is further reduced by the surrounding materials), it is difficult to build an oscillator circuit to generate stable oscillations. Further, the capacitor and resistor values need to be chosen for each device separately. Hence, making a universal read out circuit using this approach is difficult.

Recently, a hill climbing algorithm has been implemented for measuring the resonance frequencies of MEMS cantilever resonators [Fan11]. In this method, a VCO is used to actuate the cantilevers. The vibration amplitude of a cantilever is measured and is

used as a feedback signal to detect the resonance frequency. The circuit locks onto the frequency of maximum vibration amplitude of the cantilever. The main limitation is that this method requires external photo detectors for generating the feedback signal.

5.2. Design of the proposed interface circuits

The working principle of the proposed circuit is similar to the hill climbing algorithm described in the previous section. Instead of measuring the frequency of local maxima in the electromechanical impedance, the proposed circuit measures the frequency of local minima in the impedance. In addition, the proposed circuit also does not require any external photo detectors for generating the feedback signal. This is important as the biopsy needles containing the PZT elements will be inserted into a tissue and the vibrations of the PZT elements cannot be measured using an external sensor. A more detailed explanation of the working principle of the proposed circuit is described in the next section.

5.2.1. Sensing circuit for resonance frequency shift measurement

Figure 5.1 shows the block diagram of the proposed interface circuit for measurement of resonance frequency shift of the PZT heater during tissue cauterization. It consists of a voltage controlled oscillator (VCO), low pass filter, current to voltage converter, peak detection circuit and an adder circuit. This section describes the working principle of the proposed circuit.

Figure 5.2 shows the typical electromechanical impedance spectrum of a PZT element around the resonance frequency. A VCO is used to generate a square wave

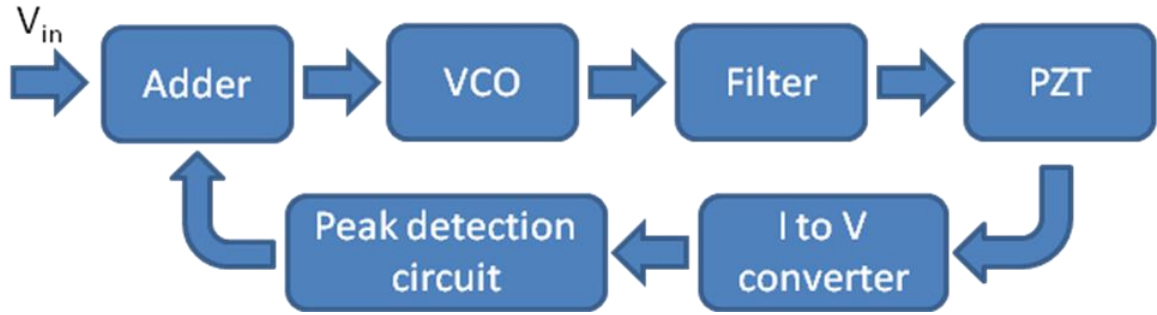


Figure 5.1: The block diagram of the proposed readout circuit for measurement of the resonance frequency shift of the PZT heaters due to tissue cauterization

signal with frequency proportional to an applied input voltage. An initial voltage, V_{in} , is used to initiate the signal from the VCO. Assume that for this initial voltage, V_{in} , the VCO generates a signal at frequency f_1 (Fig. 5.2). This signal is passed through a low-pass filter to convert the square wave signal into a sine wave signal. This signal is applied to the PZT element. A current to voltage converter is used to generate a voltage signal proportional to current flowing through the PZT element. A peak detection circuit provides a DC voltage value corresponding to the amplitude of the AC current flowing through the PZT element. This, in turn, is added to the initial voltage (V_{in}) and provided as input to the VCO. This increases the output signal frequency of the VCO from f_1 to f_2 (Fig. 5.2). Since the impedance of the PZT element at f_2 is lower than that at f_1 , the amplitude of the AC current flowing through the PZT element increases. This, in turn, increases the voltage output from the peak detection circuit, which further increases the frequency of the output signal from the VCO.

This process is repeated until the frequency of the output of the VCO becomes f_3 . The change in the signal frequency from f_3 to f_4 leads to an increase in the impedance of the PZT element. This reduces the amplitude of the AC current flowing through the PZT

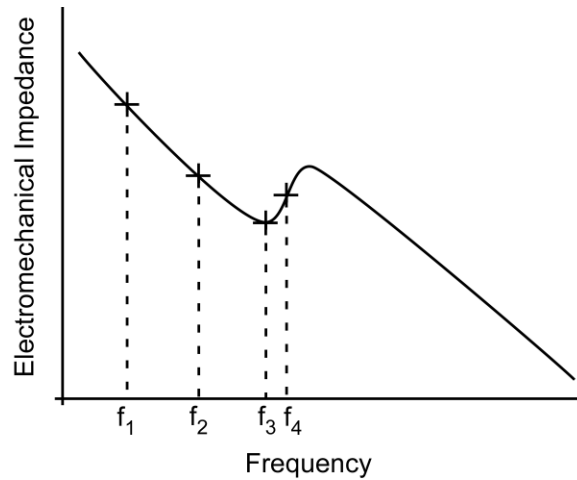


Figure 5.2: Schematic of a typical electromechanical impedance curve of a PZT element around its resonance frequency.

element, which, in turn, reduces the feedback voltage. This shifts the output frequency of the VCO towards f_3 . Thus, the output frequency of the system settles around f_3 , which is the resonance frequency of the PZT element.

5.2.2. Actuation circuit

Based on the experiments on tissue cauterization described in Chapter 4 it was observed that the actuation circuit for driving the PZT heaters should be able to generate a signal with amplitude of 25-30 V and frequency of 8-12 MHz. Figure 5.3 shows the block diagram of the actuation interface circuit for the PZT heater. It consists of a MOSFET driver and high voltage p and n channel FETs. The MOSFET driver is used to drive high voltage p and n -channel transistors and should be capable of delivering high output current to drive the capacitive load. Further, it should have a very low input capacitance and fast switching speed.

The output of the MOSFET driver is then used as input to a high voltage, low threshold n and p -channel FETs which generate the desired high voltage pulses. The

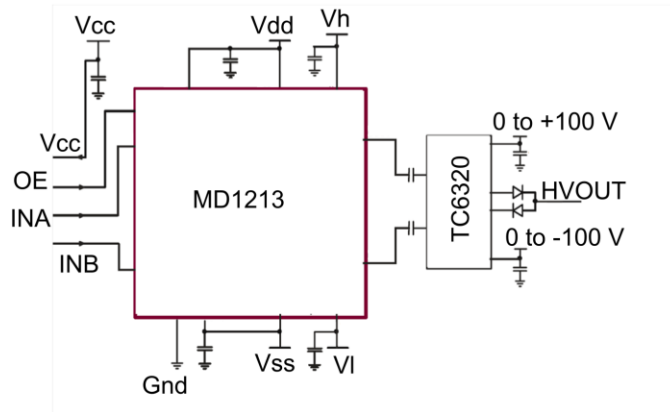


Figure 5.3: Schematic of the interface circuit for actuation of the PZT heaters [Sup00].

FETs should have a low input capacitance, high breakdown voltage and fast switching speeds.

5.3. Simulation results

The performance of the proposed circuit was verified using simulations in PSpice®. Figure 5.4 shows the schematic of the circuit used in the simulations.

The voltage-controlled square-wave oscillator was modeled using an ideal sine wave generator with very high output voltage amplitude (of 100 V), connected to two zener diodes (Fig. 5.4). The two zener diodes clipped the sine wave when the amplitude reached a value equal to the sum of the forward voltage drop and reverse breakdown voltage of the zener diode. The zener diodes were selected such that the amplitude of the square wave was ≈ 3.3 V which is a typical output from a commercially available CMOS VCO. Figure 5.5 shows an exemplary output from the simulated VCO. To prevent the loading of the VCO and to increase the current delivered to the circuit, the output of the VCO was connected to a voltage buffer.

The output of the voltage buffer was connected to a low-pass filter to convert the square wave signal into a sine wave signal. The resonance frequency of the PZT element is about 7-10 MHz. Hence, the filter was designed to have low attenuation for frequencies <15 MHz and high attenuation for frequencies >15 MHz. To achieve a flat response in the low pass region and a steep roll-off above the cut off frequency, an eighth order butterworth low pass filter using Sallen-Key topology was implemented [Tex01]. The frequency response of the designed filter is shown in Fig. 5.6. The simulations suggested the cutoff frequency to be 16 MHz. The roll-off for the designed filter was 160 dB/dec.

A non-inverting amplifier was connected to the output of the filter to amplify the signal, if necessary. The output of the amplifier was connected to the PZT element. The

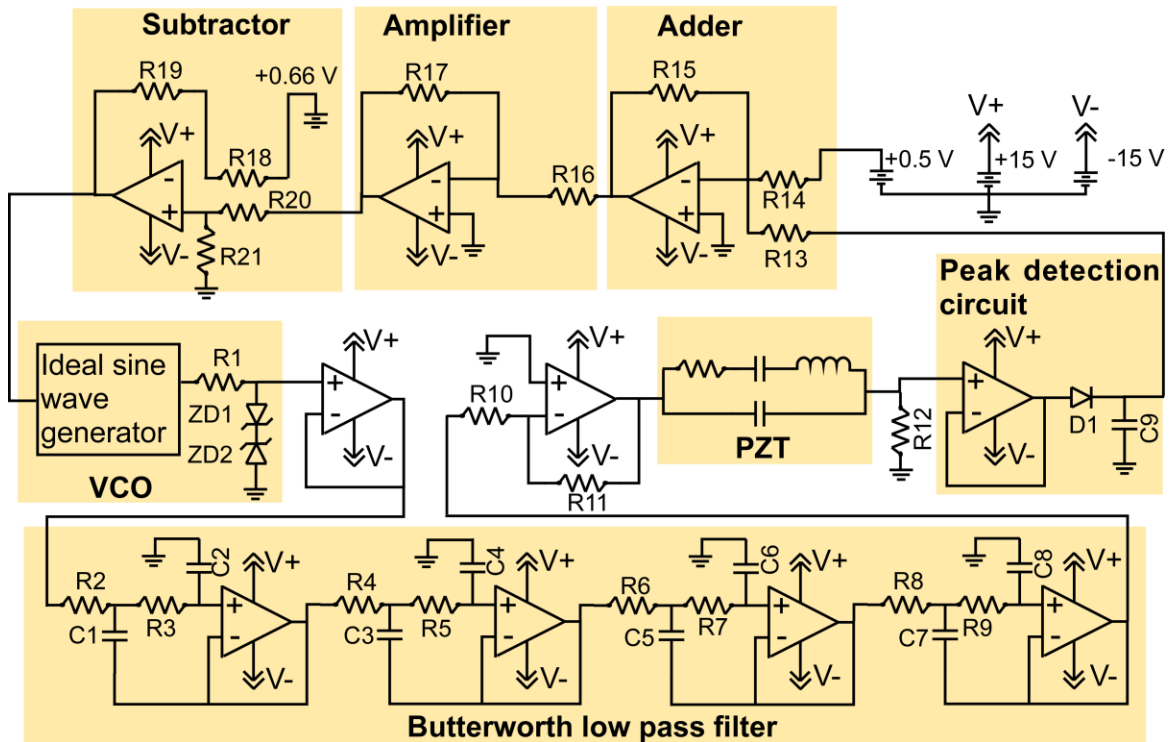


Figure 5.4: Schematic of the circuit used in PSpice simulations.

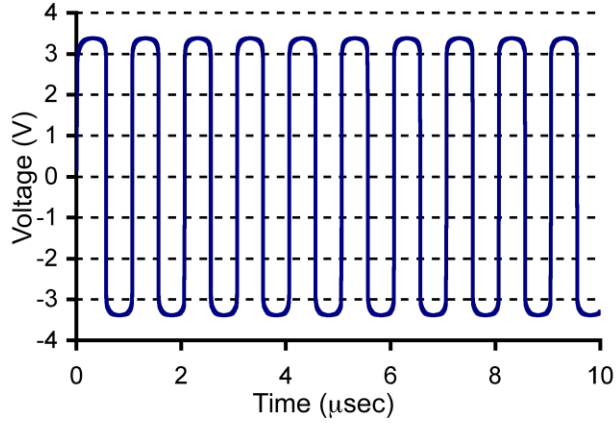


Figure 5.5: Simulated output of the simulated VCO for a frequency of 5 MHz. The amplitude of the square wave generated is ≈ 3.3 V.

PZT element was modeled using the Butterworth Van Dyke circuit as shown in Fig. 5.4. As described in chapter 4, the BVD model consists of a static branch and infinite number of motional branches. In this model, only the fundamental resonance mode was considered. Hence only one motional branch was used in the simulations. The resonance frequency is given by:

$$f_{r1} = \frac{1}{2\pi\sqrt{L_1C_1}} \quad (5.1)$$

Hence the resonance frequency of the PZT element can be varied by changing either motional inductance, L_1 , or motional capacitance, C_1 .

A 430 Ω resistor connected in series with the PZT element was used as the current to voltage converter. The voltage drop across this resistor was proportional to the amplitude of the AC current flowing through the PZT element. This voltage signal was provided as the input signal to a peak detection circuit through a voltage buffer. The peak detection circuit consisted of a diode and a capacitor. A sample simulated response of the peak detection circuit for an input sine wave of amplitude 5 V and frequency 11

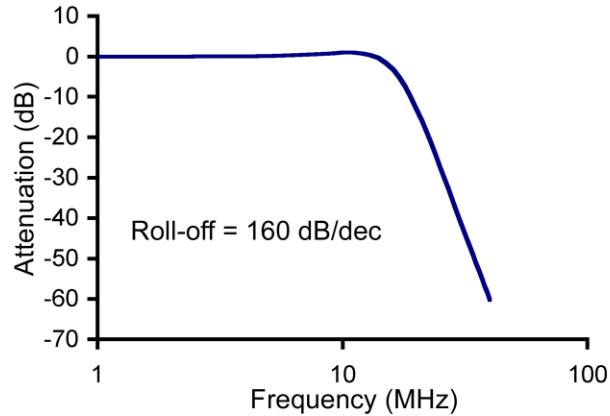


Figure 5.6: Simulated frequency response of the eighth order Butterworth low-pass filter implemented using Sallen-Key topology.

MHz is shown in Fig. 5.7. The peak detection circuit settled around 4.7 V instead of 5 V due to the voltage drop across the diode.

The obtained DC voltage was used as an input to an adder circuit built using an opamp. A constant voltage of 0.5 V was provided to the other input of the adder circuit. This constant voltage was used to initiate the signal output from the VCO. From simulations, it was observed that for maximizing the bandwidth of the circuit, a smaller initial voltage was needed at lower frequencies and a higher initial voltage was required

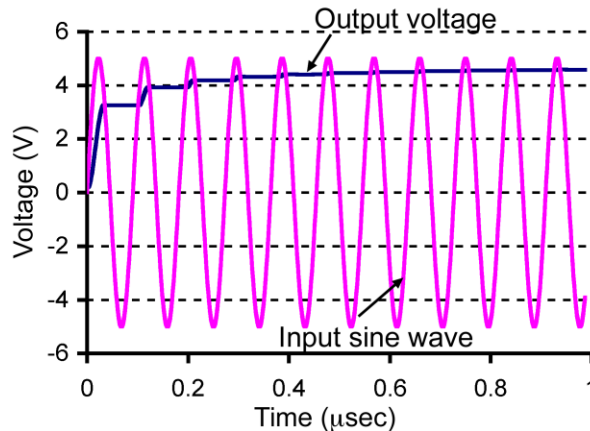


Figure 5.7: Simulated output of the peak detection circuit for an input sine wave of amplitude 5 V and frequency 11 MHz. The input sine wave is also shown.

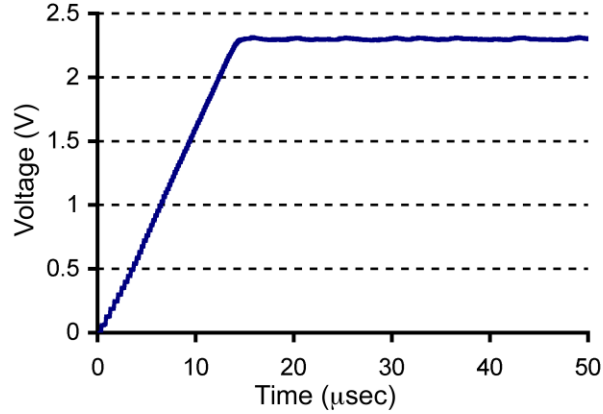


Figure 5.8: The simulated variation of the input voltage to the VCO with time for a PZT resonance frequency of 8.76 MHz.

at higher frequencies. Hence, the adder circuit was designed to add 1.5 x the voltage from the peak detection circuit to the initial voltage of 0.5 V.

Also, the VCO with the following transfer function was found to provide a larger bandwidth for the circuit:

$$f = 4 \times 10^6 \times V_{in} \quad (5.2)$$

where f is the output frequency of the VCO and V_{in} is the input voltage to the VCO. However, the transfer function of the commercially available VCO was:

$$f = 2 \times 10^6 + 3 \times 10^6 \times V_{in} \quad (5.3)$$

Hence amplifier and subtractor circuits (built from op-amps) were used to obtain the desired transfer function given by equation 5.2.

Transient simulations were performed in PSpice to verify the functioning of the proposed circuit. The variation of V_{in} (the input voltage to the VCO) with time for a resonance frequency of 8.76 MHz is shown in Fig. 5.8. The output of the circuit for various resonance frequencies was tested by varying the value of the motional capacitance in the BVD model. Simulations were also performed for both low and highly

Table 5.1. PSpice simulation results of the proposed circuit for low and highly damped PZT element.

Motional capacitor (pF)	Resonance frequency (MHz)	Simulated frequency for $R_1 = 500 \Omega$ (MHz)	Simulated frequency for $R_1 = 3500 \Omega$ (MHz)
0.3	13.46	12.5	12.11
0.4	11.65	11.69	11.5
0.5	10.41	10.49	10.55
0.6	9.48	9.61	9.84
0.7	8.76	8.84	8.94
0.8	8.17	8.3	8.3
0.9	7.74	7.83	7.92
1	7.3	7.44	7.61
1.1	6.91	7.08	7.49
1.2	6.7	6.8	7.44

damped PZT elements by varying the value of the motional resistor (R_1). Motional resistor values of 500Ω and 3500Ω were used to model the low and highly damped PZT element, respectively. In these simulations, the static capacitor and the motional inductor values were assumed to be 18.91 pF and $463.6 \mu\text{H}$. The simulation results are listed in Table 5.1. The circuit worked well in the frequency range of 7 MHz to 11.5 MHz .

5.4. PCB layout and fabrication

5.4.1. Sensing circuit

The sensing circuit was built and tested using discrete integrated chip (IC) components on a printed circuit board (PCB) (Advanced Circuits Inc., Aurora, CO) and breadboard. Figure 5.9 shows the schematic of the circuit built for testing of the proposed circuit. A four layer PCB design was used. The intermediate layers consisted of a ground plane and a split power plane to supply power to the op-amps. A separate power line of 5 V was used to supply power to the VCO. The photograph of the designed

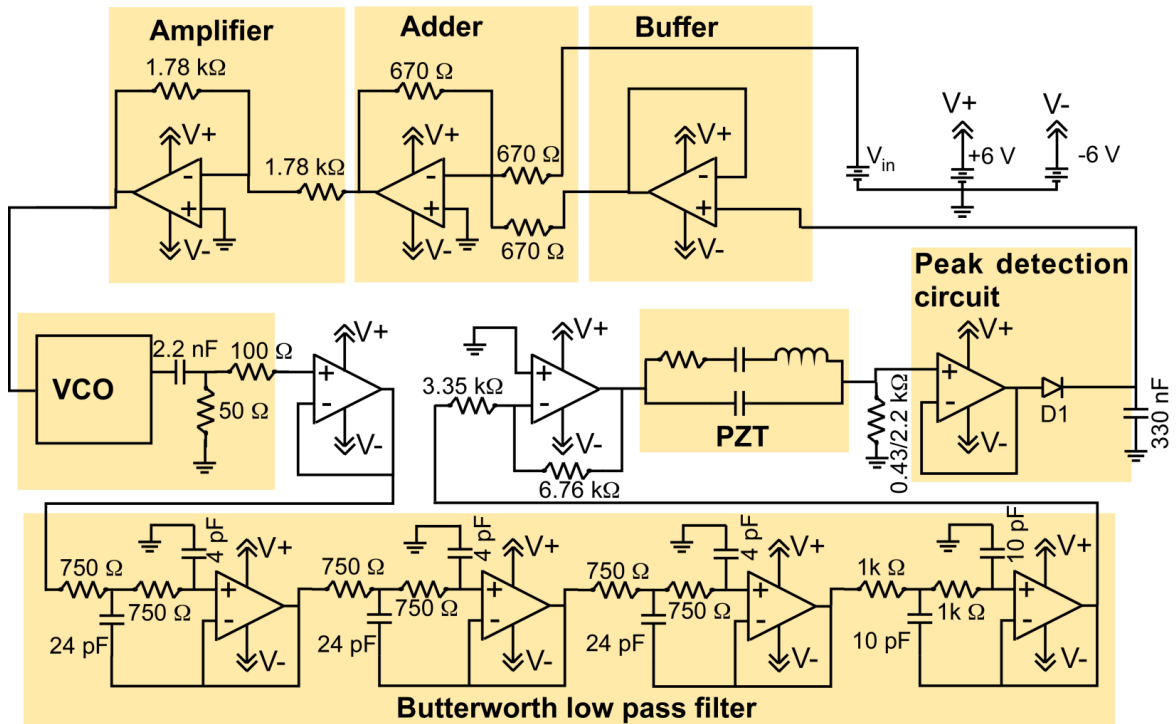


Figure 5.9: Schematic of the circuit built and tested on a PCB and breadboard.

PCB is shown in Fig. 5.10. A SN74LS624 IC (Texas Instruments Inc., Dallas, TX) was used as the VCO. The VCO was capable of generating signals with frequencies up to 20 MHz which was greater than the targeted range of 7-12 MHz. The voltage feedback amplifiers, AD8056, (Analog Devices Inc., Norwood, MA) were used for AC signal processing. Op-amps LM741 (National Semiconductor Inc., Santa Clara, CA) were used for DC signal processing. Table 5.2 lists the components used in this design.

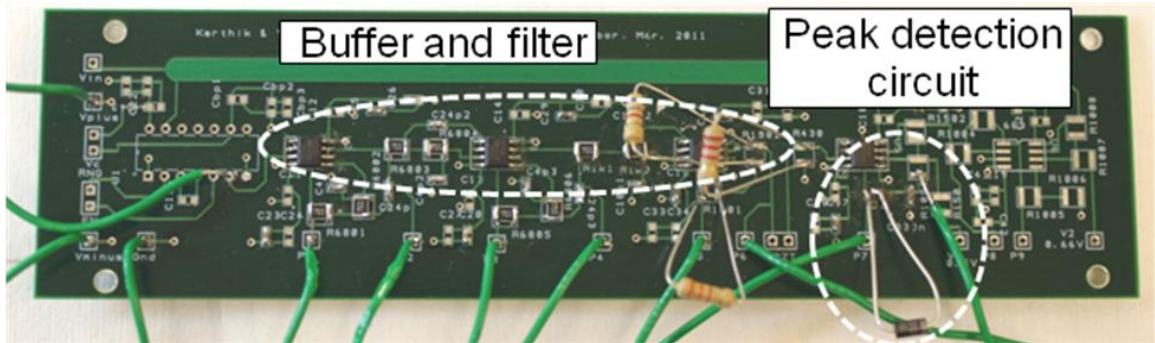


Figure 5.10: Photograph of the PCB used in the experiments.

Table 5.2: List of ICs used in the experiments.

Component	Quantity
SN74LS624 VCO	1
AD8056 op-amp	4
LM741 op-amp	3
750 Ω resistor	6
1000 Ω resistor	2
670 Ω resistor	3
1.78 k Ω resistor	2
3.35 k Ω resistor	1
6.76 k Ω resistor	1
430/2000 Ω resistor	1
100 Ω resistor	1
50 Ω resistor	1
2.2 nF capacitor	1
10 pF capacitor	2
24 pF capacitor	3
4 pF capacitor	3
330 nF capacitor	1
Diode	1

5.4.2. Actuation circuit

The MD1213DB1 demoboard (Supertex Inc., Sunnyvale, CA) was used as the actuation circuit. The photograph of the demoboard used in these experiments is shown in Figure 5.11. It consisted of a MOSFET driver (MD1213) and an IC containing high

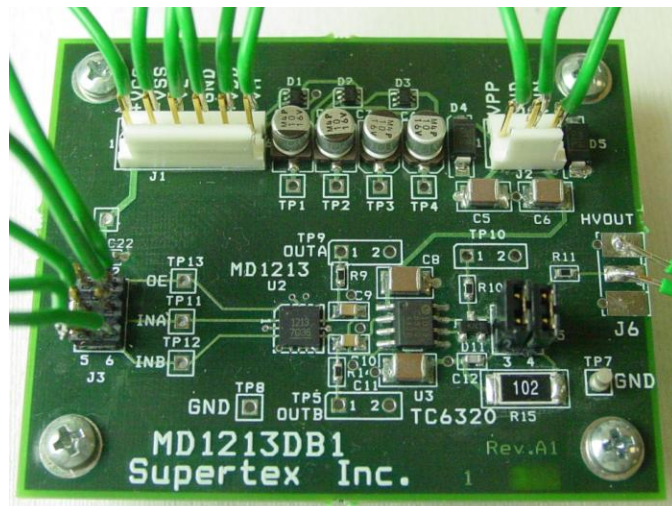


Figure 5.11: Photograph of the demoboard used for actuation of the PZT heaters.

voltage p and n channel FETs (TC6320). This circuit can provide signals with peak to peak amplitudes of ± 100 V and frequencies up to 20 MHz. In addition, it also had a source and sink current capability of ± 2 A.

5.5. Experimental results

5.5.1. Resonance frequency measurement circuit testing

5.5.1.1. Experimental setup

The op-amps in the circuit were powered by a ± 13 V DC power supply (HPE3630A). The voltage controlled oscillator was powered using +5 V DC power supply. Separate power and ground connections were provided for the digital and analog portions of the VCO to improve the stability of the output signal at higher frequencies. The output of the various individual components was measured using an Agilent DSO8064A oscilloscope.

5.5.1.2. Testing of VCO

The VCO (SN74LS624) was tested separately on a breadboard. A 15 pF capacitor and a 2 V DC voltage input was used to set the frequency range. The frequency control input voltage was varied from 0 to 3.5 V and the output frequency of the VCO was recorded. Figure 5.12 shows a sample signal generated by the VCO. Table 5.3 compares the experimental frequency with the expected frequency from the datasheet of the output signal of the VCO for various frequency control input voltages. Experiments suggested that the VCO output frequency was greater than the expected frequency by $\approx 80\%$.

Table 5.3: Comparison of the experimental frequency and the expected frequency for the output signal from the VCO.

Frequency control voltage (V)	Expected frequency (MHz)	VCO output frequency (MHz)
0.5	3	5.4
1	4.8	8.2
1.5	6.5	10.9
2	8	14.1
2.5	9.5	18.2
3	11	20.8
3.5	12.5	24



Figure 5.12: A sample waveform signal generated by the VCO.

5.5.1.3. Testing of Butterworth low pass filter

The filter was tested by providing an input square wave from a function generator (HP33120A). Figure 5.13 shows a sample input signal to the filter and the corresponding output signal from the filter. The frequency response of the filter was also measured by varying the frequency of the input sine wave signal of amplitude 4 V (Fig. 5.14). The experiments suggested the cut-off frequency of the low pass filter to be 12 MHz.

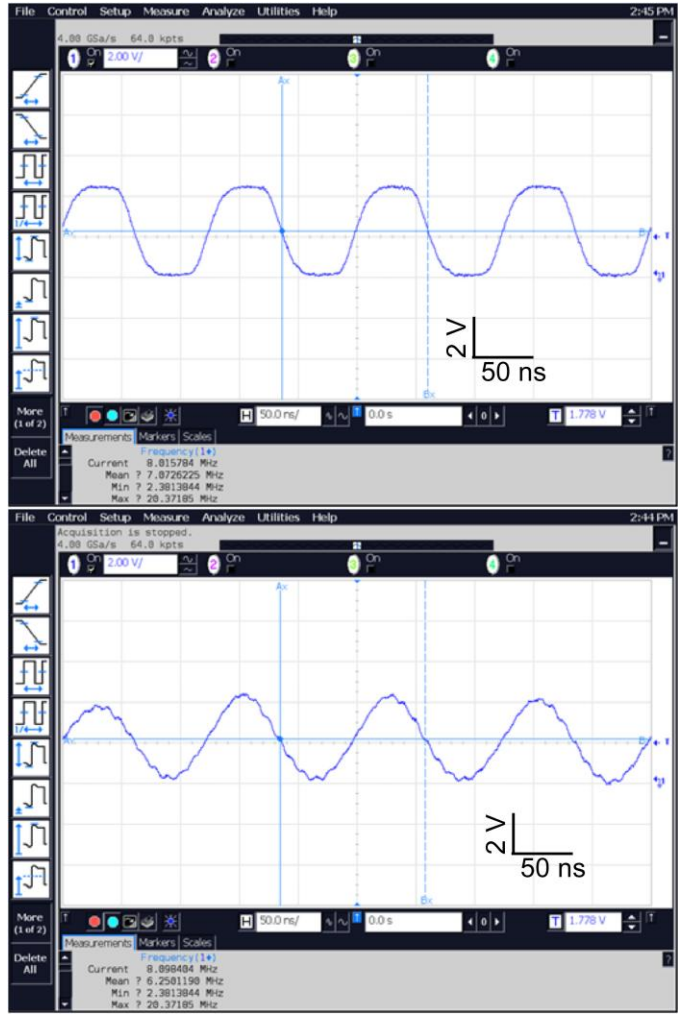


Figure 5.13: (a) Screenshot of the sample signal input to the filter and (b) Screenshot of the corresponding output from the filter. The designed filter had a cut-off frequency of 12 MHz.

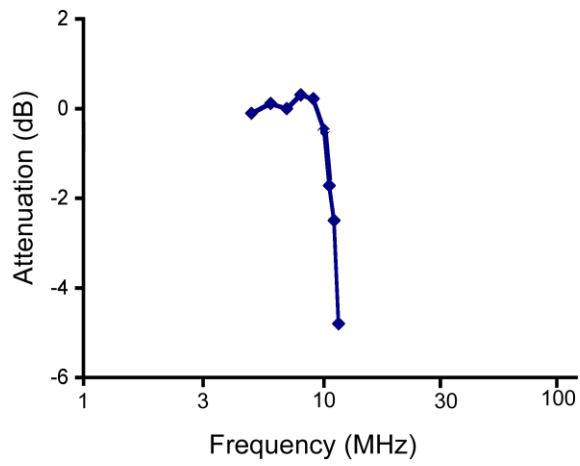


Figure 5.14: Measured frequency response of the designed Butterworth low pass filter for an input sine wave of amplitude 4 V.

Table 5.4: Comparison of the amplitude of the input sine wave signal and the output DC signal from the peak detection circuit.

Amplitude of AC signal (V)	Peak detection output (V)
4.48	4.32
5.03	4.89
3.9	3.73
3.3	3.17

5.5.1.4. Testing of the peak detection circuit

The peak detection circuit was tested by providing an input signal from the function generator to the diode. The output was measured across the capacitor attached to the diode. Figure 5.15 shows a sample input sine wave signal and output signal from the peak detection circuit. Table 5.4 compares the amplitude of the input sine wave and the output voltage from the peak detection circuit.

5.5.1.5. Testing of the adder, amplifier and subtractor

The adder, amplifier and the subtractor circuits were tested by providing two DC voltages at the input of the adder. Table 5.5 compares the calculated and experimental

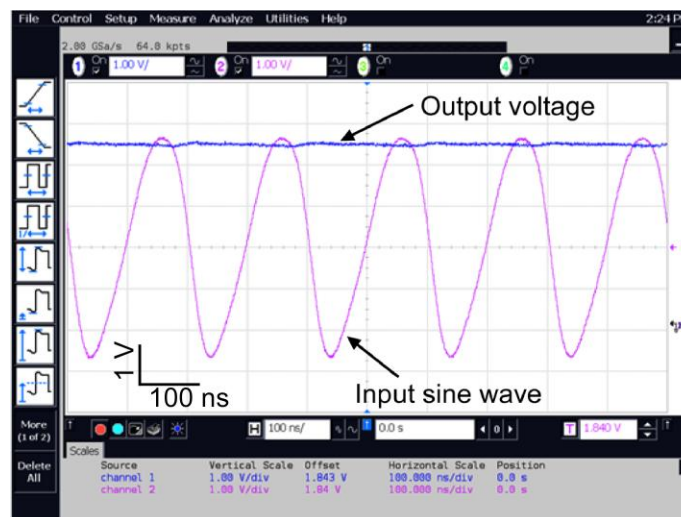


Figure 5.15: A sample input sine wave signal to the peak detection circuit and its corresponding output.

Table 5.5: Comparison of the calculated and experimental outputs obtained from adder, amplifier and subtractor circuits. A1 and A2 are the inputs to the adder and S1 is the input to the subtractor.

A1	A2	S1	Expected adder output	Experimental adder output	Expected amplifier output	Experimental amplifier output	Expected subtractor output	Experimental subtractor output
3	0.55	3.4	-3.825	-3.86	4.9725	4.87	1.47	1.43
2	0.55	2	-2.825	-2.85	3.6725	3.7	1.7	1.56
2	1	2	-3.5	-3.52	4.55	4.32	2.32	2.4
2	1	3	-3.5	-3.52	4.55	4.32	2.32	1.38

data obtained from the adder, multiplier and the subtractor. The results suggest that each of the components was working well.

5.5.1.6. Testing of the complete circuit

The proposed circuit was tested initially using a BVD model resonator to show the feasibility of the proposed circuit for measuring the resonance frequency of the resonator. The schematic of the BVD model resonator used in these experiments is shown in Fig. 5.16. In these experiments the values of R_1 , L_1 and C_0 were selected to be 500Ω , $27 \mu\text{H}$ and 20 pF , respectively. The resonance frequency of the resonator was varied by changing the value of capacitor C_1 in the BVD model. In these experiments, the current to voltage converter resistor value was 430Ω . Figure 5.17a shows the electromechanical impedance of the BVD model resonator obtained using an impedance

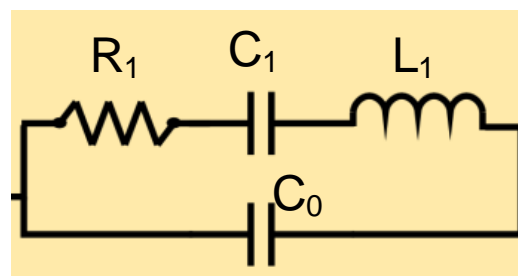


Figure 5.16: The schematic of the BVD model resonator used in the experiments.

Table 5.6: Experimental comparison of the resonance frequency of the BVD model resonator measured using the impedance analyzer and from the proposed circuit

C1 (pF)	Resonance frequency (MHz) (Impedance analyzer)	Resonance frequency (MHz) (From circuit)
5	7.87	8.16
3.33	8.4	8.6
2.5	8.66	8.86
2	8.78	8.89
1.67	8.98	9.17

analyzer for a C_1 value of 5 pF. The corresponding input signal provided to the BVD model resonator by the proposed circuit when the resonator is connected to it is shown in Fig. 5.17b. The frequency of this signal determined the resonance frequency of the circuit.

Table 5.6 compares the resonance frequency obtained from the impedance analyzer and the proposed circuit. Experiments suggested that the circuit was able to follow the changes in the resonance frequency of the resonator.

Next, experiments were performed using the proposed biopsy tool to show the functioning of the circuit. In these experiments, a biopsy needle with an array of four

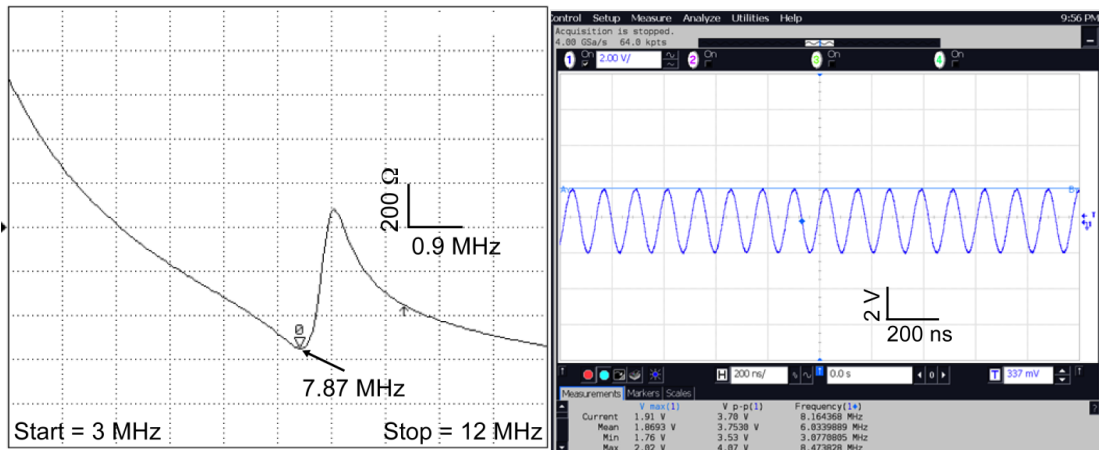


Figure 5.17: (a) Electromechanical impedance of the BVD resonator obtained using impedance analyzer for a C_1 value of 5 pF (b) The oscilloscope trace of corresponding signal given as input to the BVD resonator by the proposed circuit when the resonator is connected.

Table 5.7: Experimental comparison of the resonance frequency of the PZT embedded biopsy needle measured using the impedance analyzer and from the proposed circuit

C1 (pF)	Resonance frequency (MHz) (Impedance analyzer)	Resonance frequency (MHz) (From circuit)
Needle in air	8.22	8.2-8.27
Needle in wax	7.96	7.96-8

PZT elements with no gap between the elements was used. In these experiments, the current to voltage converter resistor value of 2.2 k Ω was used. Figure 5.18a shows the electromechanical impedance of the biopsy needle around the resonance frequency. The corresponding signal given as input to the biopsy needle by the proposed circuit when the needle is connected to it is shown in Fig. 5.18b. Table 5.7 lists the comparison of the resonance frequency measured using the impedance analyzer and the proposed circuit when the biopsy needle is in air and in wax medium. Inserting the needle into wax reduced the resonance frequency by 0.26 MHz. The circuit was able to detect the resonance frequency of the biopsy needle for both cases.

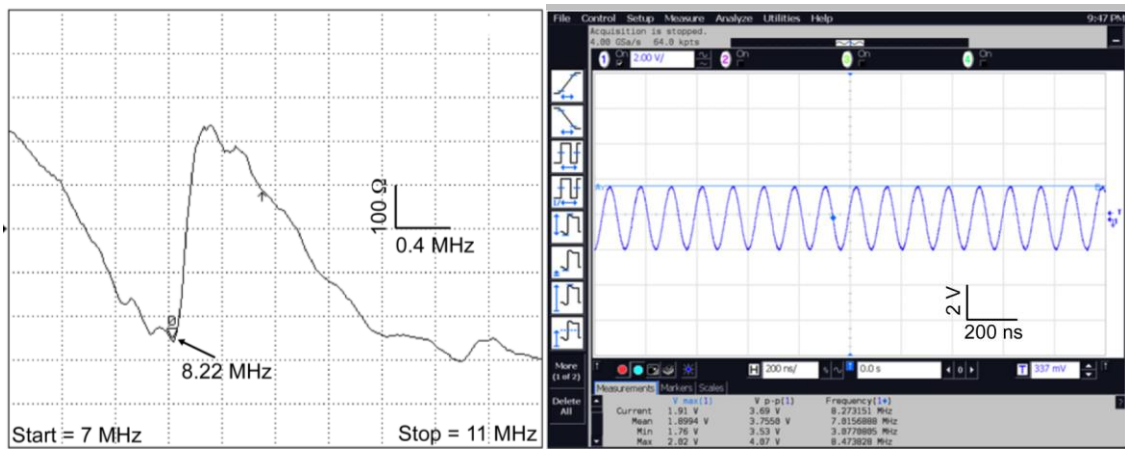


Figure 5.18: (a) Electromechanical impedance of the biopsy needle with embedded PZT heaters obtained using impedance analyzer. (b) The oscilloscope trace of corresponding signal given as input to the PZT heaters by the proposed circuit when the biopsy needle is connected.

5.5.2. Actuation circuit testing

The logic signal inputs INA and INB for the actuation circuit were provided using a function generator (HP33120A). A square wave signal of amplitude 3.3 V was used. The frequency of this signal determined the frequency of the output signal. The positive and negative drive supply for MD1213 MOSFET driver was set at 10 V and 0V, respectively. The *n* and *p* channel FETs were powered using a 13 V voltage supply. This voltage level determines the amplitude of the output square wave. The output of the circuit was measured using an Agilent DSO8064A oscilloscope. Figure 5.19 shows a sample output from the actuation circuit at 10 MHz. The amplitude of the signal was 13 V. The actuation circuit worked in the frequency range of 5-12 MHz.

5.6. Conclusions

This chapter described the interface circuits for measurement of resonance frequency shift of the PZT heater during cauterization. The sensing circuit consisted of a VCO, filter, current to voltage converter and peak detection circuit. The simulations suggested the circuit was able to lock onto the resonance frequency of the PZT. The



Figure 5.19: A sample output signal from the PZT actuation circuit.

simulations suggested the circuit to work in the frequency range of 7 MHz to 11.5 MHz. The circuit was built and tested on a PCB using discrete IC components. The circuit was tested using the proposed biopsy needle and was able to detect the resonance frequency of the needle when it was in air and in wax medium. An interface circuit for actuation of the PZT heaters was also discussed. The circuit consisted of a MOSFET driver and high voltage p and n channel FETs. The actuation circuit worked in the frequency range of 5-10 MHz.

CHAPTER 6

CONCLUSIONS AND FUTURE WORK

This chapter provides the conclusions of the research presented in this thesis and discusses some possible future directions.

6.1. Conclusions

This research effort aimed at investigating the feasibility of use of bulk micromachined PZT elements for heat generation. The PZT heaters provide certain advantages over the resistive heaters. The PZT heaters offer higher power efficiency as compared to resistive heaters because of its lower thermal conductivity which reduces losses due to heat conduction, and higher electrical impedance which reduces the parasitic losses through the connecting wires. The efficiency can be further increased by using stacked PZT element design. This also leads to precise localized heating due to lower thermal conductivity of the PZT. The electromechanical impedance characteristics of the PZT element around its resonance frequency depend on the properties of the surrounding medium. Thus the PZT heaters can lead to the development of “smart” heaters that can vary the heat generation depending on the surrounding medium.

A 3D finite element simulation model was developed to estimate the heat generation in PZT elements for various drive frequencies, voltages and geometries. The

model considered the heat generation due to losses within the PZT element as well as due to damping of the ultrasound waves by the surrounding medium. Experiments were also performed to validate the proposed simulation model. The simulations based on this model suggested the circular shape to be most suitable for generating maximum temperature rise at a given drive voltage for constant cross-sectional area and volume of the PZT element. This simulation model can provide a generalized tool for PZT heater design for other applications too.

Experiments were performed to determine suitable operating conditions for the PZT heaters. For these experiments, circular PZT-5A heaters of 3.2 mm diameter and 0.191 mm thickness were used. The PZT heaters attained maximum temperature rise at the frequency of maximum conductance and maximum thermal efficiency at frequency of maximum impedance. Further, the thermal efficiency of each resonance mode was proportional to the electromechanical coupling coefficient of that mode. The thermal efficiency of the heaters decreased with an increase in the DC offset of the applied sinusoidal drive voltage. Further, the thermal efficiency was higher in thermally non-conducting and highly damping substrates. The performance of the stacked PZT structures was also compared with unstacked structures. The stacked structures provided 3.5x the maximum temperature rise and 3x the thermal efficiency attained by the unstacked heaters. The direction of applied electric field did not measurably influence the heating characteristics of the stacked elements. Experiments were also performed to show the feasibility of biological tissue cauterization. A single element PZT heater was used for the cauterization of porcine tissue samples. A sinusoidal input voltage of 10

V_{RMS} generated an interface temperature of 150°C and branded the porcine tissue. The porcine tissue was cauterized in 2-3 seconds.

Two primary applications were explored for the proposed piezoceramic microheaters. The first one was to use the PZT heaters for locomotion initiation and direction control of airborne, ambulatory and aquatic insects. This technique was intended to be complementary to other locomotion control techniques such as electric, optical and chemical stimulation. The second application was to design and fabricate a needle tract cauterization tool to reduce the risks of tumor seeding and hemorrhage during biopsy procedures.

For the first goal, the feasibility of locomotion control of insects using thermal stimulators was demonstrated. A finite element model was developed to predict the variation of insect stimulator interface temperature with input power. Piezothermal stimulators were fabricated from PZT-5A plates using batch mode micro ultrasonic machining process. Typical sizes ranged from 200 μm to 3.2 mm. For PZT stimulators, the temperature and thermal efficiency reached maximum value around the resonance frequency which was typically in the range of 650 kHz to 47 MHz. Experiments were conducted on green June beetles (GJB), Madagascar hissing roaches and green diving beetles (GDB) to show the versatility of the proposed technique. The stimulators were implanted near the antennae of the GJB and on either side of the thorax of the Madagascar hissing roaches and GDB, respectively. In all the cases, the insect moved away from the direction of the actuated stimulator. The left and right turns were statistically similar. Thermal stimulation achieved an overall success rate of 80%, 93.5% and 68% in GJB, roaches and GDB, respectively. On average, thermal stimulation

resulted in an angle turn of about 15°-18° on GJB, 30°-45° on roaches and 15°-60° on GDB. The corresponding average input power was 360 mW, 330 mW and 100 mW for GJB, roaches, and GDB, respectively. Simulations were also performed to study the scaling limits of the piezothermal stimulators. Finite element simulations were performed for different diameters of the 125 μm -thick circular piezothermal stimulator to determine the average temperature at the tissue interface when the maximum temperature in the stimulator reaches half of the Curie temperature. Simulations suggested the minimum diameter is 130 μm , below which the temperature at the stimulator tissue interface falls below the targeted temperature of 43°C. In future, the thermal stimulation is expected to provide a generalized method for locomotion control of wide variety of insects without the need for detailed knowledge of insect physiology.

For the second goal, biopsy needles with embedded array of PZT heaters were designed and fabricated. Finite element simulations suggested that a PZT array with no gap between the elements is most suitable for generating maximum temperature rise for a given drive voltage. An analytical model based on modified Butterworth-Van-Dyke circuit model suggested that the resonance frequency of the PZT element decreases when the tissue is cauterized. PZT heaters of 200 μm diameter and 80 μm thickness were fabricated using the batch mode μ -USM process. The heaters were integrated into a recess made using μ -EDM on the inner surface of biopsy needles. The cauterization experiments were performed using porcine tissue samples. The PZT heaters were tested at both the fundamental radial (10.3 MHz) and thickness (22.3 MHz) resonance modes. The needle surface exceeded the minimum target temperature rise of 33°C for an applied voltage of 17 V_{RMS} and 14 V_{RMS} for radial and thickness mode, respectively. The

corresponding input powers were 236 mW and 325 mW, respectively. The extent of tissue cauterization was <1.25 mm beyond the perimeter of the needle thereby ensuring minimum damage to the surrounding tissues. Cauterization of porcine tissue samples resulted in a decrease of 0.6 MHz in the resonance frequency and 900 ohms in the peak impedance magnitude, thereby providing a way to monitor the extent of cauterization.

A readout circuit for measurement of resonance frequency shift of the PZT element during cauterization was also developed. The circuit was capable of locking into the local minima of the impedance curve at the resonance frequency. The circuit consisted of a VCO, low pass filter, current to voltage converter, peak detection circuit and an adder. PSpice simulations suggested the circuit to work in the frequency range from 7 MHz to 11.5 MHz. The circuit was built and tested using discrete IC components on a printed circuit board. The circuit was able to detect the resonance frequency of the PZT heaters embedded in a biopsy needle when the needle is in air and loaded with wax. An actuation circuit for driving the PZT heaters consisting of a MOSFET driver and high voltage *n* and *p* channel FETs was also discussed. In future, this technology can lead to the development of a minimally invasive servo-controlled cauterization tool. In addition to the application targeted in this work, this cauterization tool can also be used as a minimally invasive tool for tumor sensing and tumor ablation.

6.2. Future work

The locomotion control of insects using thermal stimulation is mainly limited by the high power required to actuate the PZT heater. One potential solution to reduce the input power is to decrease the size of the PZT heater. Reducing the size of the

stimulators also provides more localized heating, thereby providing better directional control (as discussed in Chapter 3).

Although the head of the beetles seems to be most sensitive to heat, it was observed that it was very difficult to achieve successful implantation of the stimulators as the beetles were easily able to access the region around the head with their legs. Hence, to improve the robustness of the technique, alternate implantation location needs to be investigated. One particular location of interest is the thorax of the flying beetles. Studies suggest that most flying beetles warm their thorax to initiate the flight [Kro41].

Currently the implanted PZT heaters are actuated using a function generator and the locomotion of insects is constrained either by attaching them to a gimbal or by restricting the free movement of insects to a limited distance. The development of an interface circuit such as the one discussed in [Sat09] would enable testing of the PZT heaters on freely moving insects. Since the circuit board needs to be mounted on the back of the insects, experiments need to be performed on insects with higher payload capacity such as *Mecynorhina torquata* [Sat09].

For the biopsy needle tract cauterization application, there are few improvements that need to be addressed. During the experiments it was observed that the output of the VCO becomes noisier and unstable for frequencies greater than 8 MHz. One possible solution to overcome this issue is by using a rectangular PZT element (of size $1 \times 0.2 \times 0.08$ mm³) instead of four circular PZT elements (of diameter = 200 μ m; thickness = 80 μ m) as the heaters. The rectangular PZT element will have a lower resonance frequency as compared to the circular elements.

In the present experiments, dead porcine tissue samples were used. Further experiments need to be performed on live animals and human beings to show the feasibility of the proposed technique. The effect of blood flow on the temperature profile generated by the heaters should be studied. Cellular histology studies should be carried out to study the extent of cauterization to the surrounding tissues.

The actuation and the sensing circuits should be combined together. In the present experiments, a function generator is used to generate the input signals to the actuation circuit. This can be replaced by a clock generator or a VCO. It was observed that the sensing resonance frequency shifts by ≈ 600 kHz during tissue cauterization. In addition, the quality factor of the resonance mode is not high. The temperature rise does not vary significantly around the resonance frequency. Hence, the PZT heaters can be driven at a fixed frequency by the clock generator or the VCO. Further the enable input in the clock generator or the VCO can be used to determine the duration of the actuation and sensing time periods.

APPENDICES

APPENDIX A

PZT FABRICATION TECHNOLOGIES

This section describes fabrication processes available for micromachining of PZT. Section A.1 describes various additive processes used for fabrication of PZT devices. Different subtractive processes used for patterning bulk PZT substrates are described in Section A.2. Section A.3 gives a detailed description of the batch mode micro ultrasonic machining process used in this work.

A.1. Additive processes for micromachining of PZT

A.1.1. Sol-gel

In the sol-gel process, a solution containing the oxide compounds of PZT is coated onto a substrate by spinning, dipping or spray coating [Coo96]. The solution is then allowed to polymerize to form a gel. The crystalline oxide film is obtained by annealing the gel at temperatures $>600^{\circ}\text{C}$. The thickness of the PZT film is limited to <200 nm because of cracking due to residual stress. Thermal expansion mismatch between the PZT film and the substrate can also affect the quality of the PZT films. Garino *et al.* have reported tensile stresses up to 400 MPa in PZT films on silicon substrates using the sol-gel process [Gar89].

A.1.2. Tape casting

Tape casting is the most common method for making flat PZT plates of large area [Nav04]. In this process, the PZT ceramic slurry is poured onto a moving belt. Then it is allowed to pass under a blade, for which the gap to the moving belt is precisely controlled. This gap determines the thickness of the PZT element. The PZT element thickness is in the range of 25 μm to 1 mm.

A.1.3. Fast deposition of ceramics (FDC)

In fast deposition of ceramics (FDC), a nozzle controlled by a CAD program deposits melted PZT in a predefined path onto a substrate to form the desired shape. Finally, a sintering step is performed [Ban98]. This technique is used to fabricate PZT actuators in various shapes such as spirals, cones, tubes, etc. in macro scale.

A.1.4. Screen printing

The screen printing method is used for thick film deposition of PZT [Lee02]. The PZT ceramic slurry is forced through a mesh and then allowed to dry. This method allows for mass production as the patterning can be performed during film deposition.

A.1.5. Dry pressing

In this method, high pressure is applied in a uniaxial direction to the PZT powder confined in a mold. The irregular-shaped ceramic particles are fused together by the pressure. Wide variety of shapes can be formed rapidly using this process [He02].

A.1.6. Molecular beam epitaxy (MBE)

In MBE, the constituent elements are thermally evaporated from respective source materials. These evaporated elements are then deposited onto a heated crystalline substrate to form thin epitaxial layers [And07]. The growth rates are typically on the order of a few angstroms for this process.

A.1.7. Pulsed laser deposition (PLD)

Pulsed laser deposition is used to deposit high quality thin films [Ver98]. In this technique, high power laser pulses are used to melt, evaporate and ionize material from the surface of a target. The ablated material is then allowed to deposit onto a substrate where it condenses and forms a thin film. Thin films deposited using PLD have high film-to-film reproducibility and accurate stoichiometry.

A.2. Subtractive processes for micromachining of PZT

A.2.1. Laser drilling or Laser ablation

There are two mechanisms for material removal by laser ablation [Des07]. The first method uses a beam with energy greater than the binding energy of the atoms of the workpiece. The molecules are decomposed directly into atoms and are removed from the workpiece. The second method involves vaporization of the workpiece using high power lasers. The heat affected region is small for laser ablation, thereby enabling precise micromachining of PZT with fewer defects. The main drawback is the low machining speed. Another drawback is the high cost of the equipment.

A.2.2. Powder blasting

Powder blasting is used for patterning brittle materials such as glasses, ceramics and ferrite materials on the micrometer scale [Wen00]. The etch rates can be as high as 1 mm/min. This method uses a mask that has good erosion resistance to impingement of solid particles. One major limitation of this process is the formation of V-shaped sidewalls on the machined substrates. The process also suffers from the blast lag problem. A wider feature opening on the mask will produce a larger cutting depth than smaller openings.

A.2.3. Wet etching

Wet etching of PZT is a fast and inexpensive method to etch large areas [Bab04]. However, it is limited by the lack of good etch control methods and by photoresist undercut, which make wet etching of narrow patterns difficult. The most common etchant used for this purpose is a mixture of hydrofluoric acid, hydrochloric acid and water. The etch rate for this process is on the order of 50-100 nm/s.

A.2.4. Dry etching

Reactive ion etching (RIE) is the most common dry etching technique used for micromachining of PZT films. Etch rates of upto 100-250 nm/min have been demonstrated using pure argon gas [Bab04]. However, this process suffers from sloped walls (with angles on the order of 35°-70°), low selectivity to photoresist, and material redeposition on the sidewalls. Hence, RIE with a halogen gas (such as chlorine and

fluorine) has been used. Etch rates of PZT upto 100 nm/min have been demonstrated using monochlorotetrafluoroethane (HC_2ClF_4) as the etch gas.

Reactive ion beam etching (RIBE) has been developed to etch PZT at lower working pressure than the RIE process can provide [Bab04]. This reduces redeposition of etched material and improves the etch anisotropy. This process also requires lower energy levels than RIE. RIBE process requires a RF power of 60 W as compared to 500 W required for RIE process.

A.2.5. Conventional ultrasonic machining (USM)

In conventional USM process, ultrasonic vibrations of 20 kHz to 100 kHz frequency with amplitudes of 0.05 mm to 0.125 mm are delivered to a tool [Mor92]. These vibrations, in turn, are transmitted to fine abrasive powders that are suspended in slurry between the tool and the surface of the workpiece. Boron carbide, silicon carbide, and aluminum oxide powders with particle diameter ranging from 0.008 mm to 0.5 mm are commonly used. When the tool approaches the workpiece, the workpiece material is removed by microchipping caused by the bombardment of the high speed powders [Mad02]. The main advantage of the ultrasonic machining process is that it produces little damage or high-stress deformation at or below the surface. Moreover, it causes no thermal or chemical alterations of the machined material. Since the tool always remains near the workpiece, it allows for accurate transfer of patterns from the tool. The USM process also creates better vertical sidewalls as compared to powder blasting. The devices used in the present work are fabricated using a batch mode ultrasonic machining

process [Li06]. A more detailed discussion of the process is given in the following section.

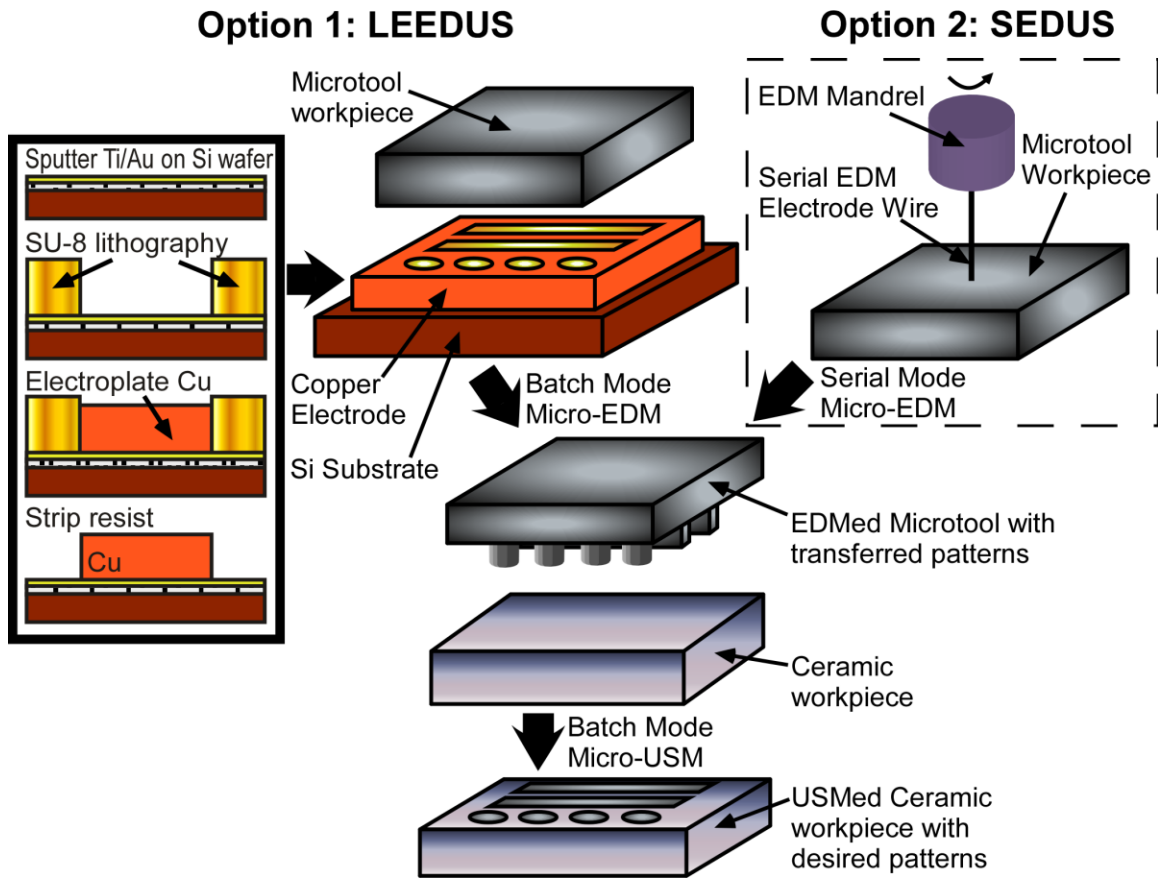


Figure A.1: Schematic of the LEEDUS and SEDUS process used for patterning PZT ceramic plate [Li09].

A.3. Batch-mode electro-discharge machining and ultrasonic machining process (SEDUS and LEEDUS)

The SEDUS and LEEDUS process flows are shown in Figure A.1. In the SEDUS process, serial-mode micro electro-discharge machining (μ EDM) is performed on a hard-metal microtool workpiece (such as stainless steel), to create the negative of the desired pattern [Li06]. The setup for serial mode μ EDM is shown in Figure A.2. In the μ EDM process, the tungsten electrode and the stainless steel workpiece are immersed in

dielectric oil (kerosene). A pulsed discharge is used to perform the machining. The stainless steel workpiece is eroded much faster during the discharge than the tungsten electrode. During the machining process, the tungsten electrode is rotated at very high speed to prevent the welding of the electrode and the workpiece.

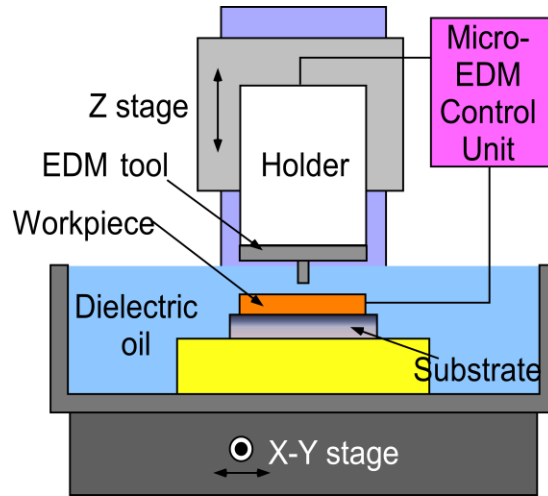


Figure A.2: Schematic of the serial mode μ EDM setup used for fabrication of microtools [Li09].

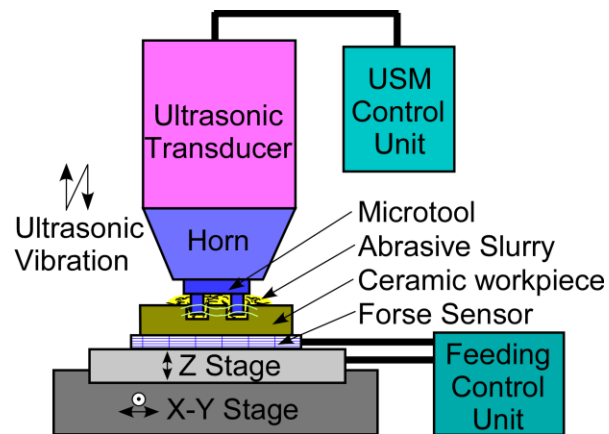


Figure A.3: Schematic of the μ USM setup created for batch mode pattern transfer to ceramic workpiece [Li09].

The microtool created using μ EDM is then mounted on an ultrasonic machining (μ USM) setup to transfer the desired positive pattern onto the ceramic workpiece. The

schematic diagram of the setup used for batch-mode μ USM is shown in Figure A.3. The setup consists of an X-Y stage for alignment of the microtool and the ceramic workpiece. A motorized Z stage controlled by a computer is used to feed the tool towards the workpiece. A force sensor mounted below the Z stage is used to monitor the machining load. The μ EDM'ed microtool is mounted at the tip of the horn using epoxy. Abrasive slurry consisting of water and tungsten carbide powders of 0.5-1 μm diameter is circulated between the microtool and the ceramic workpiece. The vibrating tip of the microtool is fed towards the ceramic workpiece. During the downward stroke the vibration of the microtool imparts velocity to the abrasive particles. These particles, in turn, erode the workpiece, thereby creating the desired patterns on the workpiece. Machining rates of $>18 \mu\text{m}/\text{min}$ for both Macor and PZT have been reported [Li06].

To increase the throughput of the process and for transferring complex patterns, the LEEDUS process can be used. In this process, a batch mode μ EDM step is performed to fabricate the microtool for the μ USM process using an electrode array fabricated using lithography and electroplating. The electrode array is vibrated in a vertical axis perpendicular to the workpiece to prevent the welding of electrode and the workpiece. The schematic diagram of the setup used for batch mode μ EDM is shown in Figure A.4. This process can provide 20-30x higher throughput as compared to serial μ EDM. Finally, the batch mode μ USM is used to transfer the patterns from the μ EDM'ed microtool to the ceramic substrates as described for the SEDUS process.

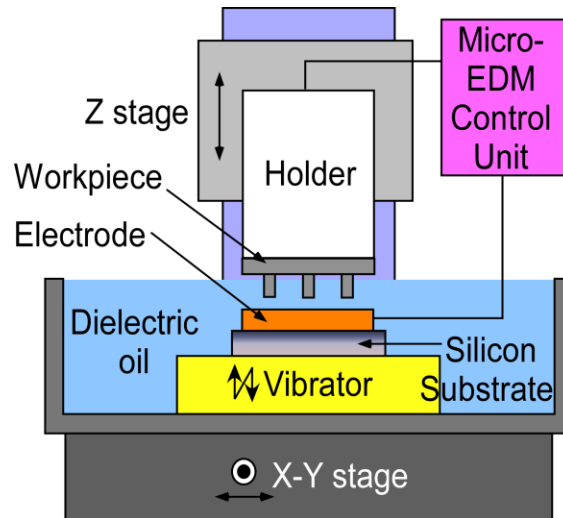


Figure A.4: Schematic of the batch mode μ EDM setup used for fabrication of microtools [Li09].

APPENDIX B

3D-SOULE: A FABRICATION PROCESS FOR LARGE SCALE INTEGRATION AND MICROMACHINING OF SPHERICAL STRUCTURES

This section reports a method for integrating and micromachining spherical structures made from brittle materials such as ceramics, glasses and fused quartz. The 3D-SOULE process combines batch-mode micro ultrasonic machining (μ USM), lapping, and micro electro-discharge machining (μ EDM) for creating spherical structures [Vis06]¹. Micro electro discharge machining is used for creating the stainless steel tool, which is then used for μ USM of the glass spheres. Section B.1 discusses the motivation and the past work on microfabrication of spherical structures. The 3D-SOULE process flow is described in Section B.2. Section B.3 describes the simulation model used for estimating the resonance frequency of the fabricated structures. Section B.4 describes the

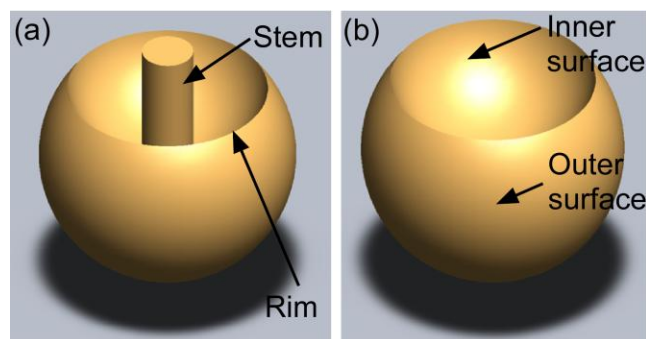


Figure B.1: Schematic of the (a) Mushroom and (b) concave shaped spherical structure fabricated using the 3D-SOULE process.

¹Dr. Tao Li had substantial contributions to this work.

experimental results.

B.1. Introduction

Three dimensional (3D) microstructures in hemispheric, “wine glass” and mushroom shapes are attractive for certain types of inertial sensors (such as rate integrating gyroscopes) (Fig. B.1) [Mat92, Shk05, Izm99]. Most conventional surface and bulk microfabrication methods like etching, film deposition, photolithography, etc. are limited to creating planar structures. Microfabrication methods such as LIGA [Bec86, Guc98] and deep reactive ion etching (DRIE) [Bos94, Cho02] are well suited for creating high-aspect-ratio structures out of metal and silicon, respectively. However, these methods are not easily adapted for making spherical shapes. The use of isotropic wet etching, deposition and oxidation to microfabricate free standing spherical structures from silicon dioxide has been discussed in [Wis81]. The fabrication of dome shaped structures utilizing the buckling of prestressed thin polysilicon films has been discussed in [Zal03]. The thicknesses of the shells fabricated using these techniques are limited to few microns. Recently, a wafer-scale glass blowing process has been reported for the fabrication of spherical shells from glass composites that can melt at modest temperatures [Ek107]. In this process cavities are etched into a silicon wafer, followed by anodic bonding of a glass wafer to the silicon wafer. The wafers are then heated above the softening-point temperature of the glass. The expansion of the trapped gas in the silicon cavities leads to formation of 3D spherical shells.

In this work, a complementary method for integrating and micromachining concave and mushroom-shaped spherical structures made from materials such as fused

quartz (that are not amenable to melting or reflow) is reported. The 3D-SOULE process is a 3D-capable and self-aligned process combining batch-mode micro ultrasonic machining (μ USM), lapping, and micro electro-discharge machining (μ EDM). Since μ USM does not involve any chemical or high temperature steps, it is possible to create stress-free structures in a wide variety of ceramics, glasses and other brittle materials [Li06, Li10].

B.2. Process description

Figure B.2 shows the schematic of the 3D-SOULE process for fabricating concave and mushroom-shaped spherical structures. Initially, μ EDM is used to micromachine cavities in a steel substrate for holding stainless steel spheres (Fig. B.2.1). In the μ EDM process, the tungsten electrode and the stainless steel workpiece are immersed in dielectric oil (kerosene). A pulsed discharge is used to perform the machining. The stainless steel workpiece is eroded much faster during the discharge than the tungsten electrode.

Nonconductive epoxy is then applied into the cavities on the stainless steel substrate. Commercially-obtained stainless steel spheres of 0.8 mm diameter (with A.F.B.M.A. grade 25), with high geometrical precision (with sphericity $<0.625 \mu\text{m}$), are then assembled into these cavities. The stainless steel spheres are then pressed into the epoxy from above using a flat substrate, after which the epoxy is then allowed to cure. This ensures that the tips of all the spheres are at the same level (Fig. B.2.2). For the mushroom shape, an additional μ EDM step is performed to form cavities, of $200 \mu\text{m}$

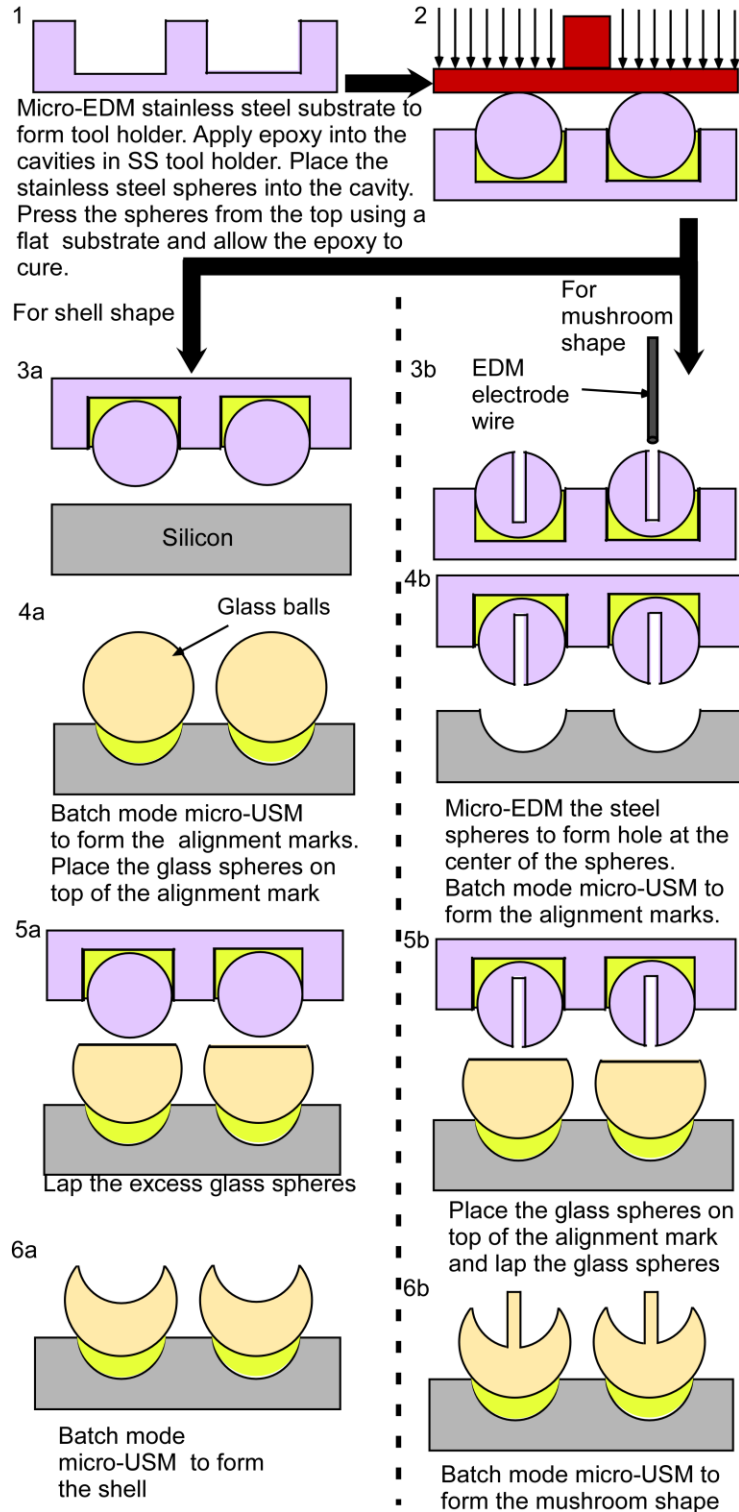


Figure B.2: 3D-SOULE process flow diagram for fabrication of concave and mushroom-shaped spherical structures. 3D-SOULE process utilizes serial μ EDM, batch mode μ USM and lapping to fabricate devices in the above mentioned shapes. This process can be applied to a wide variety of glasses, fused quartz etc.

diameter and 750 μm depth, at the center of the stainless steel spheres (Fig. B.2.3b). This enables the formation of the stem for the mushroom-shaped structures. The diameter of the cavities determines the diameter of the stem in the mushroom-shaped structure at the end of the process. The X-Y resolution of the μEDM positioning stage is 0.1 μm , which enables the fabrication of stainless steel spheres with centered holes.

Next a silicon carrier substrate is bonded to a glass plate. Batch-mode μUSM [Li06, Li10] is then used to form 100 μm deep alignment marks on the silicon carrier substrate with the above assembled stainless steel tool (Fig. B.2.4b). In this process, a 20 kHz ultrasound generator with vibration amplitude of 15 μm is used. This vibration, in turn, is transferred to fine abrasive particles that are suspended in water between the tool and the silicon substrate. Tungsten carbide powders of 0.5-1 μm particle size are used in this process. The pattern on the assembled tool is then transferred onto the silicon substrate by microchipping caused by the bombardment of the high speed powders. For the mushroom shape, an additional step is performed to remove the post formed at the center of the alignment marks.

Glass spheres of 1 mm diameter (NBK7, 1 μm sphericity) with high precision and surface finish are mounted and self-assembled into the alignment marks created on the silicon substrate (Fig. B.2.4a). This ensures that the center of the microtool and the target glass spheres are self-aligned to each other with high geometrical precision. The glass spheres are bonded to the silicon substrate using epoxy (Stycast 2850). Lapping is performed using abrasive slurry (containing 0.25 μm diameter diamond particles) to remove the excess epoxy and to reduce the height of the glass spheres as desired (Fig. B.2.5a,b). A copper lapping plate is used in this process. Batch-mode μUSM on the

lapped glass spheres is then performed to form the desired concave and mushroom shaped spherical structures (Fig. B.2.6a,b). The μ USM process leads to the formation of sharp edges along the rim of the fabricated structures. An additional lapping step can be performed in order to remove the sharp edges on the machined glass spheres. The glass spheres are finally released from the silicon substrate using Dynasolve 165.

B.3. Simulation model

Finite element simulations were performed to determine the resonance frequency of the 4-node “wine-glass” resonance mode in the fabricated structures. The structural mechanics module in COMSOL Multiphysics 3.5a® was used in these simulations. Eigen frequency analysis was carried out on the mushroom-shaped structure with fixed boundary condition applied to the tip of the stem of the structure. The diameter of the stem was assumed to be 200 μm and the mushroom structure was assumed to be fabricated from a glass sphere (Density = $2200 \text{ kg}\cdot\text{m}^{-3}$; Elastic modulus = 73.1 GPa) of 1 mm outer diameter. The height of the glass sphere was assumed to be reduced to 800 μm

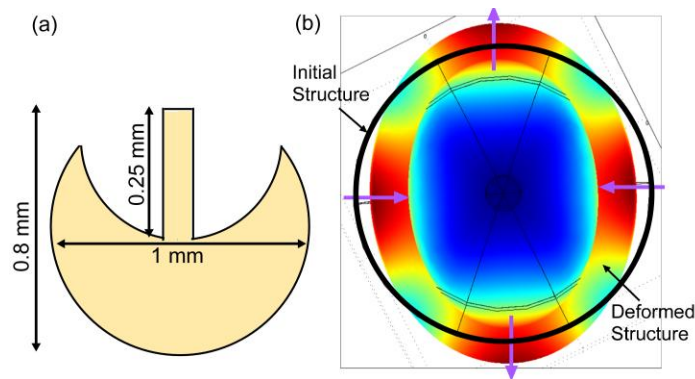


Figure B.3: (a) Schematic of the cross-section view of the simulated structure. (b) Simulated mode shape of the 4 node “wine glass” resonance mode. The simulated value of the resonance frequency was 1.36 MHz.

Table B.1: Comparison of tool wear in SS 316 and SS 440 spheres during μ USM process.

	SS316	SS440
Substrate machined	Glass	Glass
Depth of machining	300 μm	300 μm
Tool wear (volume)	$1.30 \times 10^{-11} \text{ m}^3$	$3.68 \times 10^{-12} \text{ m}^3$

by lapping. The machining depth of the μ USM process was assumed to be 250 μm . Figure B.3a shows the cross-section of the simulated structure. Figure B.3b shows the simulated mode shape of the 4-node “wine-glass” resonance mode in a mushroom structure. It consisted of four anti-nodes of maximum displacement and four nodes of minimum displacement. This mode was selected as it was expected to have low anchor loss. Simulations suggest that the resonance frequency of this mode is 1.36 MHz.

B.4. Experimental results

B.4.1. Fabrication results

Material wear during batch-mode μ USM for stainless-steel spheres made of SS440 and SS316 was compared for determining the most suitable tool material for this application. Machining of the NBK-7 spheres was performed using SS316 and SS440 spheres and the tool wear was determined by measuring the change in the height of the sphere after machining. A laser displacement sensor (Keyence LKGD500) was used for measuring the wear on the stainless steel spheres. Table B.1 lists the comparison of the wear in SS440 and SS316 spheres. Tool wear for SS440 was less than one-sixth as that of SS316. Hence SS440 spheres were used in the fabrication process.

The machining parameters for the batch mode μ USM process used in the 3D-SOULE process are listed in Table B.2. Figures B.4a and B.4b show the photograph of

Table B.2: Machining parameters for the batch mode μ USM process used in the 3D-SOULE process

Ultrasound generator frequency	20 kHz
Ultrasound vibration amplitude	15 μm
Abrasive powder (Tungsten carbide)	0.5-1 μm
Avg. machining rate (depth)	24 $\mu\text{m}/\text{min}$
Machining load	0.5 N
Cutting depth	350 μm

the assembled μ USM tool for fabrication of concave and mushroom-shaped spherical structures, respectively. Figures B.5a and B.5b show the SEM images of the fabricated concave and the mushroom-shaped spherical glass structures. The photograph of the outer surface of a mushroom structure fabricated from a 1 mm diameter NBK-7 glass sphere is shown in Fig. B.5c. A machining rate of 24 $\mu\text{m}/\text{min}$ was achieved for a machining depth of 350 μm at a vibration amplitude and frequency of 15 μm and 20 kHz, respectively, of the ultrasound generator.

Experiments were also performed to show the feasibility of machining ruby spheres using the 3D-SOULE process. Ruby spheres of 1 mm outer diameter were used in these experiments. Figure B.5d shows the photograph of a fabricated mushroom structure from a ruby sphere. A machining rate of 12 $\mu\text{m}/\text{min}$ was achieved for a machining depth of 50 μm at a vibration amplitude and frequency of 15 μm and 20 kHz, respectively, of the ultrasound generator.

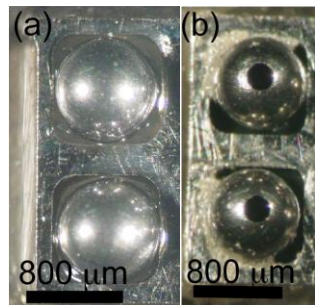


Figure B.4: (a) USM tool for fabrication of spherical shell. (b) USM tool for fabrication of mushroom shaped structure with cavities at the center of the sphere.

B.4.2. Resonance characteristics of mushroom structures

The mushroom-shaped glass structures were actuated with a PZT stack actuator ($5 \times 5 \times 2 \text{ mm}^3$, Physik Instrumente Inc.). The stem of the mushroom structure was bonded to the PZT actuator through a small brass spacer using adhesive polymer. The PZT actuator was mounted on a high precision XY stage (CVI Melles Griot) attached to a rotary stage (Thorlabs RP01) which enabled easy centering of the structure to the axis of rotation of the rotary stage. This also enabled the measurement of the vibration velocity along the circumference of the mushroom-shaped structure to verify the resonance mode. The vibration velocity of the mushroom-shaped structure was measured using a laser vibrometer (Polytec OFV3001S). The outer surface of the structure was sputtered with a 50 nm thick titanium layer and a 500 nm thick gold layer to provide a reflecting surface. The HP4395A network analyzer connected to a power amplifier was used to sweep the drive frequency of the PZT actuator and to record the corresponding output from the laser vibrometer.

The resonance frequency of the “wine-glass” mode was experimentally measured to be 1.379 MHz. This matched well with the simulation results described in Section

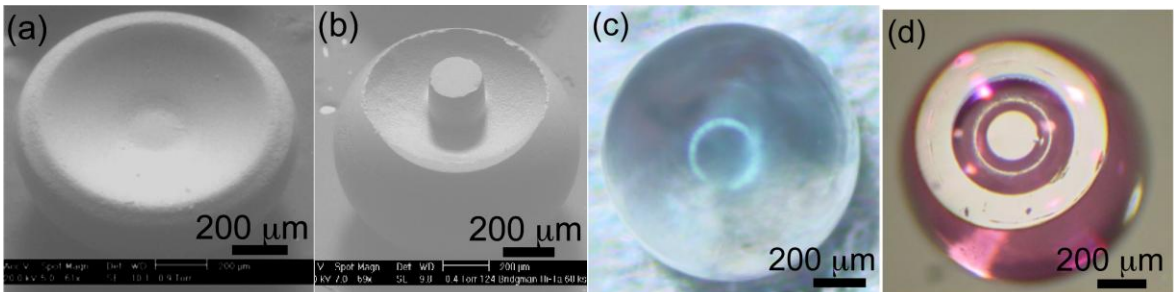


Figure B.5: SEM image of the fabricated (a) concave spherical structure and (b) mushroom shaped structure. (c) Photograph of the top view of the mushroom structure made from transparent NBK7 glass spheres. (d) Photograph of a fabricated mushroom structure from a ruby sphere.

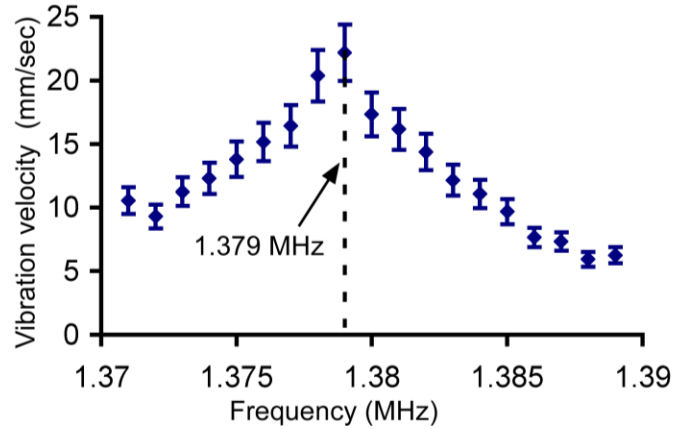


Figure B.6: Resonance characteristics of mushroom-shaped structure around the 4-node wine-glass mode resonance frequency (1.379 MHz) in air. The quality factor of the resonance mode was experimentally measured at 345 in air, limited largely by anchor loss.

B.3. The mode shape was verified by rotating the structure on the rotary stage and measuring the vibration velocity along its circumference. The variation of the vibration amplitude of the mushroom structure as a function of actuation frequency was also measured and the results are shown in Fig. B.6. The quality factor of the resonance mode was measured to be 345 in air. The quality factor is believed to be constrained primarily by the method of attachment (using adhesive polymer) to the PZT substrate.

B.5. Conclusions

A 3D micromachining process combining batch mode micro ultrasonic machining, lapping and micro electro-discharge machining for fabrication of concave and mushroom-shaped spherical structures was described. This process was capable of machining spherical structures from materials such as glass and ruby. Stainless steel 440 was determined to be the suitable tool material for the ultrasonic micromachining with a tool wear below 5%. A machining rate of 24 $\mu\text{m}/\text{sec}$ was achieved for fabrication of

concave and mushroom-shaped spherical structures from 1 mm diameter NBK-7 glass spheres. Finite element simulations were used to determine the resonance frequency of the “wine-glass” mode in the mushroom-shaped structure. The quality factor of the “wine-glass” resonance mode in the mushroom-shaped spherical structure is measured to be 345 in air. This approach has been proved feasible and bears significant promise in the long term for wafer-scale microfabrication of spherical structures from high Q materials such as fused quartz.

BIBLIOGRAPHY

- [Aba05] M. Abaraw, "An introduction to thermal remediation from TEMP-AIR: A patented process to eliminate pests with dry, clean heat: An effective, safe and economical alternative to methyl bromide," *Annual International Conference on Methyl Bromide Alternatives and Emissions Reductions*, 2005
- [Aka05] F. Akasheh, J.D. Fraser, S. Bose, and A. Bandyopadhyay, "Piezoelectric micromachined ultrasonic transducers: modeling the influence of structural parameters on device performance," *IEEE Transactions on Ultrasonics, Ferroelectrics and Frequency Control*, 52, pp. 455-468, 2005
- [Alg04] M. Alguero, C. Alemany, and L. Pardo, "Method for obtaining the full set of linear electric, mechanical and electromechanical coefficients and all related losses of a piezoelectric ceramic," *Journal of American Ceramics Society*, 87, pp. 209-215, 2004.
- [All88] D.J. Allison and A. Adam, "Percutaneous liver biopsy and track embolization with steel coils," *Radiology*, 169, pp. 261-263, 1988.
- [Ame01] R.G. Amedee and N.R. Dhurandhar, "Fine needle aspiration biopsy," *The Laryngoscope*, 111, pp. 1551-1557, 2001
- [And07] P.S. Anderson, S. Guerin, B.E. Hayden, M.A. Khan, and A.J. Bell, "Synthesis of the ferroelectric solid solution, $\text{Pb}(\text{Zr}_{1-x}\text{Ti}_x)\text{O}_3$ on a single substrate using a modified molecular beam epitaxy technique," *Applied Physics Letters*, 90, 202907, 2007.
- [Ara04] H.F. Arata, H. Noji, and H. Fujita, "Motion control of single F_1 -ATPase rotary biomolecular motor using microfabricated local heating devices," *Applied Physics Letters*, 88, 083903, 2006.
- [Asa03] N. Asai, R. Matsuda, M. Watanabe, H. Takayama, S. Yamada, A. Mase, M. Shikida, K. Sato, M. Lebedev, J. Akedo, "Novel high resolution optical scanner actuated by aerosol deposited PZT films," *16th IEEE International Conference on Micro Electro Mechanical Systems*, Kyoto, pp. 247-250, 2003.
- [Ash98] S. Ashley, "Palm-size spy planes," *ASME Journal of Mechanical Engineering*, 120, pp. 74-78, 1998.
- [Ata93] M. Ataka, A. Omodaka, N. Takeshima, and H. Fujita, "Fabrication and operation of polyimide bimorph actuators for a ciliary motion system," *Journal of Microelectromechanical Systems*, 2, pp. 146-150, 1993.
- [Bab04] J. Baborowski, "Microfabrication of piezoelectric MEMS," *Journal of Electroceramics*, 12, pp. 33-51, 2004.

- [Ban98] A. Bandyopadhyay, R.K. Panda, T.F. McNulty, F. Mohammadi, S.C. Danforth, and A. Safari, "Piezoelectric ceramics and composites via rapid prototyping techniques," *Rapid Prototyping Journal*, 4, pp. 37-49, 1998
- [Ban99] H.L. Bandey, S.J. Martin, and R.W. Cernosek, "Modeling the responses of thickness-shear mode resonators under various loading conditions," *Analytical Chemistry*, 71, pp. 2205-2214, 1999
- [Bac09] R.J. Bachmann, F.J. Boria, R. Vaidyanathan, P.G. Ifju, and R.D. Quinn, "A biologically inspired micro-vehicle capable of aerial and terrestrial locomotion," *Mechanisms and Machine Theory*, 44, pp. 513-526, 2009
- [Bar04] D. Barretino, M. Graf, and W.H. Song, "Hotplate based monolithic CMOS microsystems for gas detection and material characterization for operating temperatures up to 500 °C," *IEEE Journal of Solid-State Circuits*, 39, pp. 1202-1207, 2004.
- [Afr02] M.Y. Afridi, J.S. Suehle, and M.E. Zaghoul, "A monolithic CMOS microhotplate based gas sensor system," *IEEE Sensors Journal*, 2, pp. 645-655, 2002.
- [Bas07] A.S. Basu and Y.B. Gianchandani, "A 128-pixel digitally programmable microfluidic platform for non-contact droplet actuation using marangoni flows," *Proceedings of International Conference on Solid State Sensors, Actuators, and Microsystems (Transducers)*, Lyon, pp. 771-774, 2007.
- [Bec86] E.W. Becker, W. Ehrfeld, P. Hagmann, A. Maner, and D. Munchmeyer, "Fabrication of microstructures with high aspect ratios and great structural heights by synchrotron radiation lithography, galvanofforming, and plastic molding," *Microelectronic Engineering*, 4, pp. 35-56, 1986.
- [Ber98] C.W. Bert and V. Birman, "Effects of Stress and Electric Field on the Coefficients of Piezoelectric Materials: One Dimensional Formulation," *Mechanics Research Communications*, 25, pp. 165-169, 1998.
- [Big08] http://www.thebigzoo.com/Animals/Madagascar_Hissing_Cockroach.asp, referenced on 11th September 2008.
- [Bil90] B.E. Billard, K. Hynynen, and R.B. Roemer, "Effects of physical parameters on high temperature ultrasound hyperthermia," *Ultrasound in Medicine and Biology*, 16, pp. 409-420, 1990.
- [Bos94] Robert Bosch GmbH, U.S. Patents 4855017 and 4784720, 1994.
- [Boz08] A. Bozkurt, R. Gilmour, D. Stern, and A. Lal, "MEMS based bioelectronic neuromuscular interfaces for insect cyborg flight control," *21st IEEE International Conference on Micro Electro Mechanical Systems*, Tuscan, pp. 160-163, 2008.

- [Cen97] Y.A. Cengel, "Heat Transfer – A Practical Approach," *McGraw Hill*, pp. 244-271, 1997.
- [Cha05] S. Chang, S.H. Kim, H.K. Lim, W.J. Lee, D. Choi, and J.H. Lim, "Needle tract implantation after sonographically guided percutaneous biopsy of hepatocellular carcinoma: evaluation of doubling time, frequency, and features on CT," *American Journal of Roentgenology*, 185, pp. 400-405, 2005.
- [Che05] Q. Chen and Q.M. Wang, "The effective electromechanical coupling coefficient of piezoelectric thin film resonators," *Applied Physics Letters*, 86, 022904, 2005.
- [Chi89] R.A. Chisholm, S.N. Jones, and W.R. Lees, "Fibrin sealant as a plug for the post liver biopsy needle track," *Clinical Radiology*, 40, pp. 627- 628, 1989.
- [Cho00] R. Chopra, M.J. Bronskill, and F.S. Foster, "Feasibility of linear arrays for interstitial ultrasound thermal therapy," *Medical Physics*, 27, pp. 1281-1286, 2000.
- [Cho02] T.K.A. Chou and K. Najafi, "Fabrication of out of plane curved surfaces in Si by utilizing RIE lag," *IEEE International Conference on Micro Electro Mechanical Systems*, Las Vegas, pp. 145-148, 2002.
- [Cho05] J. Cho, M. Anderson, R. Richards, D. Bahr, and C. Richards, "Optimization of electromechanical coupling for a thin film PZT membrane," *Journal of Micromechanics and Microengineering*, 15, pp. 1797-1803, 2005.
- [Chu04] G.S. Chung, "Fabrication and characterization of micro-heaters with low power consumption using SOI membrane and trench structures," *Sensors and Actuators A: Physical*, 112, pp. 55-60, 2004.
- [Cre05] J.F. Creemer, W. Van der Vlist, C.R. de Boer, H.W. Zandbergen, P.M. Sarro, D. Briand, and N.F. de Rooij, "MEMS hotplates with TiN as a heater material," *IEEE Sensors*, Orange county, pp. 330-333, 2005.
- [Col85] D.J. Coleman, F.L. Lizzi, J. Driller, A. Rosado, S.E.P. Burgess, J.H. Torpey, M.E. Smith, R.H. Silverman, M.E. Yablonski, S. Chang, and M.J. Rondeau, "Therapeutic ultrasound in the treatment of glaucoma. II. Clinical applications," *Ophthalmology*, 92, pp. 347-353, 1985.
- [Coo96] T.G. Cooney and L.F. Francis, "Processing of sol-gel derived PZT coatings on non-planar substrates," *Journal of Micromechanics and Microengineering*, 6, pp. 291-300, 1996.
- [Cun94] M.J. Cunningham, S.T. Cheng, and W.W. Clegg, "A differential interferometer for scanning force microscopy," *Measurement Science and Technology*, 5, pp. 1350-1354, 1994.

- [Dem06] A.J. DeMello, "Control and detection of chemical reactions in microfluidic systems," *Nature*, 442, pp. 394-402, 2006
- [Des07] J.P. Desbians and P. Masson, "ArF excimer laser micro machining of Pyrex, SiC and PZT for rapid prototyping of MEMS components," *Sensors and Actuators A: Physical*, 136, pp. 554-563, 2007.
- [Die90] C.J. Diederich and K. Hynynen, "The development of intracavitary ultrasonic applicators for hyperthermia: A design and experimental study," *Medical Physics*, 17, pp. 626-634, 1990.
- [Die99] C.F. Diederich, W.H. Nau, and P.R. Stauffer, "Ultrasound applicators for interstitial thermal coagulation," *IEEE Transactions on Ultrasonics, Ferroelectrics and Frequency Control*, 46, pp. 1218-1228, 1999.
- [Dod00] G.D. Dodd III, M.C. Soulen, R.A. Kane, T. Livaghi, W.R. Lees, Y. Yamashita, A.R. Gillams, O.I. Karahan, and H. Rhim, "Minimally invasive treatment of malignant hepatic tumors: At the threshold of a major breakthrough," *Radio Graphics*, 20, pp. 9-27, 2000
- [Dom88] J.M. Domek and D.T. Johnson, "Demonstration of semiochemically induced aggregation in green June beetle, *cotinis nitida*," *Environmental Entomology*, 17, pp. 147-149, 1988.
- [Dur01] F. Durand, J.M. Regimbeau, J. Belghiti, A. Sauvanet, V. Vilgrain, B. Terris, V. Moutardier, O. Farges, and D. Valla "Assessment of the benefits and risks of percutaneous biopsy before surgical resection of hepatocellular carcinoma," *Journal of Hepatology*, 35, pp. 254-288, 2001.
- [Dur99] F.M. Durville, R.R. Rediker, R.J. Connolly, S.D. Schwaitzberg, and J. Lantis, "Diode laser for abdominal tissue cauterization," *SPIE Conference on Gastrointestinal Surgery*, San Jose, pp. 420-424, 1999.
- [Dut90] N.R. Dutta, A.K. Bose, H.K. Kapoor, and S. Gupta, "Head and neck cancers: results of thermoradiography and radiography," *International Journal of Hyperthermia*, 6, pp. 479-486, 1990.
- [Ecc00] P.C. Eccardt and K. Niederer, "Micromachined ultrasonic transducers with improved coupling factors from a CMOS compatible process," *Ultrasonics*, 38, pp. 744-780, 2000.
- [Eer01] E.P. Eernisse and R.B. Wiggins, "Review of thickness shear mode quartz resonator sensors for temperature and pressure," *IEEE Sensors Journal*, 1, pp. 79-87, 2001.
- [Eic99] F. Eichelbaum, R. Borngraber, J. Shroder, and R. Lucklum, "Interface circuits for quartz crystal microbalance sensors," *Review of Scientific Instruments*, 70, pp. 2537-2545, 1999.

- [Ek107] E.J. Eklund and A.M. Shkel, "Glass blowing on a wafer level," *Journal of Microelectromechanical Systems*, 16, pp. 232-239, 2007.
- [Ene72] Energy Conversion Systems, Inc, *Ultrasonic cooking apparatus*, US Patent 3636859, 1972
- [Erg02] A.S. Ergun, H. Yongli, C.H. Cheng, O. Oralken, J. Johnson, H. Jagannathan, U. Demirci, G.G. Yaraliogiu, M. Karaman, and B.T. Khuri-Yakub, "Broadband capacitive micromachined ultrasonic transducers ranging from 10 KHz to 60 MHz for imaging and more," *Proceedings of IEEE Ultrasonics Symposium*, Munich, pp. 1039-1043, 2002.
- [Ezh06] S. Ezhilvalavan, Z. Zhang, J. Loh, and J.Y. Ying, "Microfabrication of PZT force sensors for minimally invasive surgical tools," *International MEMS Conference*, Singapore, pp. 979-984, 2006
- [Fan11] X.Z. Fan, N. Siwak, and R. Ghodssi, "An adaptive feedback circuit for MEMS resonators," *Journal of Micromechanics and Microengineering*, 21, 045008, 2011.
- [Fan96] C.A. Fandrich, R.P. Davies, and P.M. Hall, "Small gauge Gelfoam plug liver biopsy in high risk patients: safety and diagnostic value," *Australasian Radiology*, 40, pp. 230-234, 1996.
- [Fal99] J.K. Falstrom, M.M. Moore, S.H. Caldwell, A.H. Matsumoto, R.D. Abbott, and W.D. Spotnitz, "Use of fibrin sealant to reduce bleeding after needle liver biopsy in an anticoagulated canine model: work in progress," *Journal of Vascular and Interventional Radiology*, 10, pp. 457-462, 1999.
- [Fer96] V. Ferrari, D. Marioli, and A. Taroni, "Thick film resonant piezo layers as new gravimetric sensors," *Measurement Science and Technology*, 8, pp. 42-48, 1996.
- [Fos70] N.F. Foster, "Handbook of Thin Film Technology," *McGraw-Hill*, 1970.
- [Fry55] W.J. Fry, J.W. Barnard, F.J. Fry, R.F. Krumins, and J.F. Brennan, "Ultrasonic lesions in the mammalian central nervous system," *Science*, 122, pp. 517-518, 1955.
- [Fry60] W.J. Fry and F.J. Fry, "Fundamental neurological research and human neurosurgery using intense ultrasound," *IRE Transactions on Medical Electronics*, ME-7, pp. 166-181, 1960.
- [Gar89] T. Garino and M. Harrington, "Residual stress in PZT thin films and its effect on ferroelectric properties," *Proceedings of Materials Research Society (Ferroelectric Thin Films II)*, Boston, pp. 341-347, 1989.
- [Go100] R.L. Goldberg, S.W. Smith, J. Mottley, and K.W. Ferrara, "The Biomedical Engineering Handbook," *CRC Press*, 2000.

- [Go192] O. Goletti, M. Chiarugi, P. Buccianti, and P. Macchiarini, "Subcutaneous implantation of liver metastasis after fine needle biopsy," *European Journal of Surgical Oncology*, 18, pp. 636-637, 1992.
- [Gra08] C.F. Graetzel, V. Medici, N. Rohrseitz, B.J. Nelson, and S.N. Fry, "The cyborg fly: A biorobotic platform to investigate dynamic coupling effects between a fruit fly and a robot," *IEEE/RSJ International Conference on Intelligent Robots and Systems*, Nice, pp. 14-19, 2008.
- [Gre99] D. Greek, "Prototype for a micro air vehicle," *Professional Engineering*, 12, pp. 26, 1999.
- [Guc98] H. Guckel, "High-aspect-ratio micromachining via deep X-ray lithography," *Proceedings of the IEEE*, 86, pp. 1586-1593, 1998.
- [Gul04] P.J. Gullan and P. Cranston, "The Insects: An Outline of Entomology", *Blackwell Publishing*, pp. 85-111, 2004.
- [Guo06] S. Guo, Y. Ge, L. Li, and S. Liu, "Underwater swimming micro robot using IPMC actuator," *IEEE International Conference on Mechatronics and Automation*, Luoyang, pp. 249-254, 2006.
- [Guo08] S. Guo, L. Shi, and K. Asaka, "IPMC actuator-based an underwater microrobot with 8 legs," *IEEE International Conference on Mechatronics and Automation*, Luoyang, pp. 551-556, 2008.
- [Haa62] F.R. Haase and J.T. Noguera, "Hemostasis in tonsillectomy by electrocautery," *Archives of Otolaryngology*, 75, pp. 125-126, 1962
- [Har82] K.H. Hardtl, "Electrical and Mechanical losses in ferroelectric ceramics," *Ceramics International*, 8, pp. 121-127, 1982.
- [Hau89] K. Hausen and C. Wehrhahn, "Neural circuits mediating visual flight control in flies. I. Quantitative comparison of neural and behavioural response characteristics," *Journal of Neuroscience*, 9, pp. 3828-3836, 1989.
- [Hau90] K. Hausen and C. Wehrhahn, "Neural circuits mediating visual flight control in flies. II. Separation of two control systems by microsurgical brain lesions," *Journal of Neuroscience*, 10, pp. 351-360, 1990.
- [He02] Z. He, J. Ma, R. Zhang, and T. Li, "Fabrication and characterization of bilayered Pb(Zr,Ti)O₃-based ceramics," *Materials Letters*, 56, pp. 1084-1088, 2002.
- [Hen05] M. Hennig and D. Braun, "Convective polymerase chain reaction around micro immersion heater," *Applied Physics Letters*, 87, 183901, 2005.

- [Heo07] S. Heo and Y.Y. Kim, "Optimal design and fabrication of MEMS rotary thermal actuators," *Journal of Micromechanics and Microengineering*, 17, pp. 2241-2257, 2007.
- [Ho197] R. Holzer and I. Shimoyama, "Locomotion control of a bio-robotic system via electric stimulation," *IEEE/RSJ International Conference on Intelligent Robots and System*, Grenoble, pp. 1514-1519, 1997.
- [Hua96] G.T. Huang, J.C. Sheu, P.M. Yang, H.S. Lee, T.H. Wang, and D.S. Chen, "Ultrasound-guided cutting biopsy for the diagnosis of hepatocellular carcinoma: a study based on 420 patients," *Journal of Hepatology*, 25, pp. 334-338, 1996.
- [Hwa11] W.J. Hwang, K.S. Shin, J.H. Roh, D.S. Lee, and S.H. Choa, "Development of micro-heaters with optimized temperature compensation design for gas sensors," *Sensors*, 11, pp. 2580-2591, 2011.
- [Hyn92] K. Hynynen, "The feasibility of interstitial ultrasound hyperthermia," *Medical Physics*, 19, pp. 979-987, 1992.
- [Iee87] *IEEE standard on Piezoelectricity*, 1987.
- [Ifj02] P.G. Ifju, D.A. Jenkins, S. Ettinger, Y. Lian, W. Shy, and M.R. Waszak, "Flexible wing based micro air vehicle," *Proceedings of the American Institute of Aeronautics and Astronautics*, AIAA 2002-0705, 2002.
- [Ike96] T. Ikeda, "Fundamentals of Piezoelectricity," *Oxford Science Publications*, 1996
- [Izm99] E.A. Izmailov, M.M. Kolesnik, A.M. Osipov, and A.V. Akimov, "Hemispherical resonator gyro technology. Problems and possible ways of their solutions," *RTO SCI International Conference on Integrated Navigation Systems*, 1999.
- [Jar96] B.J. Jarosz, "Feasibility of ultrasound hyperthermia with waveguide interstitial applicator," *IEEE Transactions on Biomedical Engineering*, 43, pp. 1106-1115, 1996.
- [Joh87] R.G. Johnson and R.E. Higashi, "A highly sensitive silicon chip microtransducer for air flow and differential pressure sensing application," *Sensors and Actuators*, 11, pp. 63-72, 1987.
- [Joh82] J.H. Johnston, D.M. Jensen, and W. Mautner, "Comparison of endoscopic electrocoagulation and laser photocoagulation of bleeding canine gastric ulcers," *Gastroenterology*, 82, pp. 904-910, 1982.
- [Kel02] J. Kellogg, C. Bovais, J. Dahlburg, R. Foch, J. Gardner, D. Gordon, R. Hartley, B.K. Parsi, H. McFarlane, F. Pipitone, R. Ramamurthi, A. Sciambi, W. Spears, D. Srull, and C. Sullivan, "The NRL micro tactical expendable (MITE) air vehicle," *Aeronautical Journal*, 106, pp. 431-441, 2002.

- [Khu00] B.T. Khuri-Yakub, C.H. Cheng, F.L. Degertekin, S. Ergun, S. Hansen, X.C. Jin, and O. Oralkan, "Silicon micromachined ultrasonic transducers," *Japan Journal of Applied Physics*, 39, pp. 2883-2887, 2000.
- [Kim00] S.H. Kim, H.K. Lim, W.J. Lee, J.M. Cho, and H.J. Jang, "Needle-tract implantation in hepatocellular carcinoma: frequency and CT findings after biopsy with a 19.5-gauge automated biopsy gun," *Abdominal Imaging*, 25, pp. 246-250, 2000.
- [Kim92] M. Kimura and K. Komatsuzaki, "Microheater made of heavily boron doped single crystal silicon beam," *Technical Digest of the 11th Sensor Symposium*, Japan, pp.169-172, 1992.
- [Kim93] E.H. Kim, K.K. Kopecky, O.W. Cummings, R.G. Dreesen, and D.C. Pound, "Electrocautery of the tract after needle biopsy of the liver to reduce blood loss: Experience in the canine model," *Investigative Radiology*, 28, pp. 228-230, 1993.
- [Kis04] M.Z. Kiss, T. Varghese, and T.J. Hall, "Viscoelastic characterization of *in vitro* canine tissue," *Physics in Medicine and Biology*, 49, pp. 4207-4218, 2004.
- [Kla97] E.H. Klaassen and G.T.A. Kovacs, "Integrated thermal-conductivity vacuum sensor," *Sensors and Actuators A: Physical*, 58, pp. 37-42, 1997.
- [Koc03] C. Koch, T. Friedrich, F. Metternich, A. Tannapfel, H.P. Reimann, and U. Eichfeld, "Determination of temperature elevation in tissue during the application of the harmonic scalpel," *Ultrasound in Medicine and Biology*, 29, pp. 301-309, 2003
- [Kol96] M.C. Kolios, M.D. Sherar, and J.W. Hunt, "Blood flow cooling and ultrasonic lesion formation," *Medical Physics*, 23, pp. 1287-1298, 1996.
- [Kro41] A. Krogh and E. Zeuthen, "The mechanism of flight preparation in some insects," *Journal of Experimental Biology*, 18, pp. 1-10, 1941.
- [Kuw94] Y. Kuwana, N. Watanabe, I. Shimoyama, and H. Miura, "Behavior control of insects by artificial electrical stimulation," *Distributed Robotic Autonomous Systems*, pp. 291-302, 1994.
- [Kuw99] Y. Kuwana, N. Ando, R. Kanzaki, and I. Shimoyama, "A radiotelemetry system for muscle potential recordings from freely flying insects," *Proceedings of 1st Joint BMES/EMBS Conference Serving Humanity, Advancing Technology*, Atlanta, 1999.
- [Laf02] C. Lafon, D.M. de Lima, Y. Theillière, F. Prat, J.Y. Chapelon, and D. Cathignol, "Optimizing the shape of ultrasound transducers for interstitial thermal ablation," *Medical Physics*, 29, pp. 290-297, 2002.

- [Lec98] S. Leclerc, R. Antaki, and J.F. Currie, "Novel simple and complementary metal oxide semiconductor compatible membrane release design and process for thermal sensors," *Journal of Vacuum Science and Technology A*, 16, pp. 876-880, 1998.
- [Lee02] B.Y. Lee, C.I. Cheon, J.S. Kim, K.S. Bang, J.C. Kim, and H.G. Lee, "Low temperature firing of PZT thick films prepared by screen printing method," *Materials Letters*, 56, pp. 518-521, 2002.
- [Lee99] R.J. Lee, M. Buchanan, L.J. Kleine and K. Hynynen, "Arrays of multielement ultrasound applicator for interstitial hyperthermia," *IEEE Transactions on Biomedical Engineering*, 46, pp. 880-890, 1999.
- [Les96] G.A. Lesieutre, L. Fang, G.H. Koopmann, S.P. Pai, and S. Yoshikawa, "Heat generation of a piezoceramic induced-strain actuator embedded in a glass/epoxy composite panel," *Proceedings of SPIE Smart Structures and Materials*, 2717, pp. 267-275, 1996.
- [Leu97] A.M. Leung, J. Jones, E. Czyzewska, J. Chen, and M. Pascal, "Micromachined accelerometer with no proof mass," *International Electron Device Meeting (IEDM'97)*, Washington DC, pp. 899-902, 1997.
- [Li06] T. Li and Y.B. Gianchandani, "A micromachining process for die-scale pattern transfer in ceramics and its application to bulk piezoelectric actuators," *Journal of Microelectromechanical Systems*, 15, pp. 605-612, 2006.
- [Li07] T. Li, R.Y. Gianchandani, and Y.B. Gianchandani, "Micromachined bulk PZT tissue contrast sensor for fine needle aspiration biopsy," *Lab on a Chip*, 7, pp. 179-185, 2007.
- [Li09] T. Li, "Ultrasonic batch mode micromachining and its application to piezoelectric sensors for fine needle aspiration biopsy," *Ph. D. Thesis, University of Michigan*, 2009
- [Li10] T. Li and Y.B. Gianchandani, "A high speed batch mode ultrasonic machining technology for multi-level quartz crystal microstructures," *IEEE International Conference on Micro Electro Mechanical Systems*, Hongkong, pp. 398-401, 2010.
- [Lia96] C. Liang, F. Sun, and C.A. Rogers, "Electro-mechanical impedance modeling of active material systems," *Smart Material Structures*, 5, pp. 171-186, 1996.
- [Lin94] L.Y. Lin, S.S. Lee, K.S.J. Pister, and M.C. Wu, "Micro-machined three-dimensional micro-optics for integrated free-space optical system," *IEEE Photonics Technology Letters*, 6, pp. 1445-1447, 1994.
- [Liu06] L. Liu, S. Peng, X. Niu, and W. Wen, "Microheaters fabricated from a conducting composite," *Applied Physics Letters*, 89, 223521, 2006

- [Llo01] J.M. Llovet, R. Vilana, C. Bru, L. Bianchi, J.M. Salmeron, L. Boix, S. Ganau, M. Sala, M. Pages, C. Ayuso, M. Sole, J. Rodes, J. Bruix, and Barcelona clinic liver cancer group, "Increased risk of tumor seeding after percutaneous radiofrequency ablation for single hepatocellular carcinoma," *Hepatology*, 33, pp. 1124-1129, 2001.
- [Mad02] M.J. Madou, "Fundamentals of Microfabrication: The Science of Miniaturization," *CRC Press*, 2002.
- [Mak05] I.R.S. Makin, T.D. Mast, W. Faidi, M.R. Runk, P.G. Barthe, and M.H. Slayton, "Miniaturized ultrasound arrays for interstitial ablation and imaging," *Ultrasound in Medicine and Biology*, 31, pp. 1539-1550, 2005
- [Mas91a] C.H. Mastrangelo and R.S. Muller, "Microfabricated thermal absolute pressure sensor with on-chip digital front-end processor," *IEEE Journal of Solid-State Circuits*, 26, pp. 1998-2007, 1991.
- [Mas91b] C.H. Mastrangelo, R.S. Muller, and S. Kumar, "Microfabricated incandescent lamps," *Applied Optics*, 30, pp. 868-873, 1991.
- [Mat92] A. Matthews and F.J. Rybak, "Comparison of hemispherical resonator gyros and optical gyros," *IEEE Aerospace and Electronic Systems Magazine*, 7, pp. 40-46, 1992.
- [Mea98] P.M. Meaney, R.L. Clarke, G.R. Ter Harr, and I.H. Rivens, "A 3-D finite element model for computation of temperature profiles and regions of thermal damage during focused ultrasound surgery exposures," *Ultrasound in Medicine and Biology*, 24, pp. 1489-1499, 1998.
- [Mic98] R.C. Michelson and S. Reece, "Update on flapping wing micro air vehicle research," *13th Bristol International RPV Conference*, Bristol, 1998.
- [Min87] G.Y. Minuk, L.R. Sutherland, D.A. Wiseman, F.R. MacDonald, and D.L. Ding, "Prospective study of the incidence of ultrasound- detected intrahepatic and subcapsular hematomas in patients randomized to 6 or 24 hours of bed rest after percutaneous liver biopsy," *Gastroenterology*, 92, pp. 290-293, 1987.
- [Miz92] T. Mizutani, H. Takanari, H. Suzuki, K. Wada, T. Mizumoto, T. Sato, S. Namikawa, and M. Kusagawa, "A new instrument for pulmonary resection: the bipolar Nd-YAG laser dissector," *Journal of Clinical Laser Medicine and Surgery*, 10, pp. 223-228, 1992.
- [Moh01] P. Mohseni, K. Nagarajan, B. Ziaie, K. Najafi and S.B. Crary, "An ultralight biotelemetry backpack for recording EMG signals in moths," *IEEE Transactions on Biomedical Engineering*, 48, pp. 734-737, 2001
- [Moo98] T.E. Moore, S.B. Crary, D.E. Koditschek, and T.A. Conklin, "Directed locomotion in cockroaches: biobots," *Acta Entomologica Slovenica*, 6, pp. 71-78, 1998.

- [Mor00] R.S. Morris and M. Holden, "Design of micro air vehicles and flight test validation," *Proceedings of Fixed, Flapping and Rotary Wing Vehicles at Very Low Reynolds Numbers*, pp. 153-176, 2000.
- [Mor92] M.A. Moreland, "Engineered Materials Handbook," *ASM International*, 1992.
- [Mot94] M.E. Motamedi, "Micro-opto-electromechanical systems," *Optical Engineering*, 33, pp. 3505-3517, 1994.
- [Mur04] P. Muralt and J. Baborowski, "Micromachined ultrasonic transducers and acoustic sensors based on piezoelectric thin films," *Journal of Electroceramics*, 12, pp. 101-108, 2004.
- [Nad04] G. Nader, E.C.N. Silva, and J.C. Adamowski, "Effective damping value of piezoelectric transducer determined by experimental techniques and numerical analysis," *ABCMS Symposium Series in Mechatronics*, 1, pp. 271-279, 2004.
- [Nah00] S.N. Goldberg, G.S. Gazelle, and P.R. Mueller, "Thermal ablation therapy for focal malignancy: A unified approach to underlying principles, techniques and diagnostic imaging guidance," *American Journal Roentgenology*, 174, pp. 323-331, 2000.
- [Nak99] K. Nakajima, N. Kudo, K. Yamamoto, T. Mikami, and A. Kitabatake, "A study on frequency dependence of ultrasound attenuation of biological tissue in the frequency range of 2-40 MHz," *IEEE Ultrasonics Symposium*, pp. 1381-1384, 1999.
- [Nav04] A. Navarro, R.W. Whatmore, and J.R. Alcock, "Preparation of functionally graded PZT ceramics using tape casting," *Journal of Electroceramics*, 13, pp. 413-415, 2004.
- [Ora03] O. Oralkan, A.S. Ergun, C.H. Cheng, J.A. Johnson, M. Karaman, T.H. Lee, and B.T. Khuri-Yakub, "Volumetric ultrasound imaging using 2-D CMUT arrays," *IEEE Transactions on Ultrasonics, Ferroelectrics and Frequency Control*, 50, pp. 1581-1594, 2003.
- [Os99] P. Osbond, C.M. Beck, C.J. Brierley, M.R. Cox, S.P. Marsh, and N.M. Shorrocks, "The influence of ZnO and electrode thickness on the performance of thin film bulk acoustic wave resonators," *Proceedings of IEEE Ultrasonics Symposium*, pp. 911-914, 1999.
- [Ove96] J. Overgaard, D.G. Gonzalez, M.C.C.M. Hulshof, G. Arcangeli, O. Dahl, O. Mella, and S.M. Bentzen, "Hyperthermia as an adjuvant to radiation therapy of recurrent or metastatic malignant melanoma," *International Journal of Hyperthermia*, 12, pp. 3-20, 1996.

- [Pan06] W. Pan, P. Soussan, B. Nauwelaers, and H.A.C. Tilmans, "A surface micromachined electrostatically tunable film bulk acoustic resonator," *Sensors and Actuators A*, 126, pp. 436-446, 2006.
- [Pat00] C. Patel, H. Arya, and K. Sudhakar, "Design, Build & fly a solar powered aircraft," Indian Institute of Technology, Mumbai, India, (<http://www.casde.iitb.ac.in/Publications/pdfdoc/solar-AeSI-AGM.pdf>)
- [Pau00] E.K. Paulson, G.R. Stephenson, M.C. Neal, V. Rossin, and J.H. Lawson, "Use of fibrin sealant as a hemostatic agent after liver biopsy in swine," *Journal of Vascular and Interventional Radiology*, 11, pp. 905-911, 2000.
- [Pau06] A. Paul, A. Bozkurt, J. Ewer, B. Blossey, and A. Lal, "Surgically Implanted Microplatforms in Manduca Sexta moth," *Solid-State Sensor & Actuator Workshop*, Hilton Head, SC, pp. 209-211, 2006.
- [Pel00] A. Pelloni and P. Gertsch, "Risks and consequences of tumor seeding after percutaneous fine needle biopsy for diagnosis of hepatocellular carcinoma," *Schweiz Med Wochenschr*, 130, pp. 871-877, 2000.
- [Pen48] H.H. Pennes, "Analysis of tissue and arterial blood temperature in the resting human forearm," *Journal of Applied Physiology*, 1, pp. 93-122, 1948.
- [Per02] G. Percin and B.T. Khuri-Yakub, "Piezoelectrically actuated flextensional micromachined ultrasonic transducers II: Fabrication and experiments," *IEEE Transaction on Ultrasonics, Ferroelectrics and Frequency Control*, 49, pp. 585-595, 2002.
- [Pic86] F. Piccinino, E. Sagnelli, G. Pasquale, and G. Giusti, "Complications following percutaneous liver biopsy: a multicentre retrospective study on 68,276 biopsies," *Journal of Hepatology*, 2, pp. 165-173, 1986.
- [Po96] D.L. Polla and L.F. Francis, "Ferroelectric thin films in microelectromechanical systems applications," *MRS Bulletin*, 21, pp. 59-65, 1996
- [Por01] T.N. Pornsin-sirirak, Y.C. Tai, H. Nassef and C.M. Ho, "Titanium alloy MEMS wing technology for a micro aerial vehicle application," *Sensors and Actuators A: Physical*, 89, pp. 95-103, 2001.
- [Pri04] W.F. Pritchard, D.W. Cahen, J.W. Karanian, S. Hilbertand, and B.J. Wood, "Radiofrequency cauterization with biopsy introducer needle," *Journal of Vascular and Interventional Radiology*, 15, pp. 183-187, 2004.
- [Put74] A.F.P. Van Putten and S. Middelhoek, "Integrated silicon anemometer," *Electronic Letters*, 10, pp. 425-426, 1974.

- [Qiu95] L. Qiu, E. Obermeier, and A. Schubert, "A microsensor with integrated heat sink and flow guide for gas flow sensing applications," *Transducers 95and Eurosensors IX*, pp. 520-523, 1995.
- [Que01] L. Que, J.S. Park, and Y. B. Gianchandani, "Bent-beam electrothermal actuators - part I: single beam and cascaded devices," *Journal of Microelectromechanical Systems*, 10, pp. 247-254, 2001.
- [Ral87] P.W. Ralls, J.A. Barakos, E.M. Kaptein, P.E. Friedman, G. Fouladian, W.D. Bose, J. Halls, and S.G. Massry, "Renal biopsy related hemorrhage: Frequency and comparison of CT and sonography," *Journal of Computer Assisted Tomography*, 11, pp. 1031-1034, 1987.
- [Rey01] P. Reynolds and J.D. Fraser, "Finite element determination of effective electromechanical coupling coefficient with applications to piezoelectric and electrostatic transducers," *Ultrasonics International Conference*, 2001.
- [Ryd03] S.D. Ryder, "Guidelines for the diagnosis and treatment of hepatocellular carcinoma (HCC) in adults," *Gut*, 52, pp.1-8, 2003.
- [San07] S.P. Sane, A. Dieudonne, M.A. Willis, and T.L. Daniel, "Antennal mechanosensors mediate flight control in moths," *Science*, 315, pp. 863-866, 2007.
- [Sat08a] H. Sato, C.W. Berry, B.E. Casey, G. Lavella, Y. Yao, J.M. VandenBrooks, and M.M. Maharbiz, "A cyborg beetle: Insect flight control through an implantable tetherless microsystem," *21st IEEE International Conference on Micro Electro Mechanical Systems*, Tuscan, pp. 164-167, 2008.
- [Sat08b] H. Sato, C.W. Berry, and M. M. Maharbiz, "Flight control of 10 gram insects by implanted neural stimulators," *Solid-State Sensor and Actuator Workshop*, Hilton Head, SC, pp. 90-91, 2008.
- [Sat09] H. Sato, Y. Peeri, E. Baghoomian, C.W. Berry, and M.M. Maharbiz, "Radio controlled cyborg beetles: A radio frequency system for insect neural flight control," *22nd IEEE International Conference on Micro Electro Mechanical Systems*, Sorrento, pp. 216-219, 2009.
- [Sch01] T.G. Schuster and J.S. Wolf, "Use of bipolar electrocautery during laproscopic donor nephrectomy," *The Journal of Urology*, 165, pp. 1968-1970, 2001.
- [Sek97] T. Seki, M. Sakata, T. Nakajima, and M. Matsumoto, "Thermal buckling actuator for micro relays," *International Conference on Solid State Sensors and Actuators*, Chicago, pp. 1153-1156, 1997.

- [Shi03] Y.S. Shin, K. Cho, S.H. Lim, S. Chung, S.J. Park, C. Chung, D.C. Han, and J.K. Chang, "PDMS based micro PCR chip with parylene coating," *Journal of Micromechanics and Microengineering*, 13, pp. 768-774, 2003.
- [Shk05] A.M. Shkel, C. Acar and C. Painter, "Two types of micromachined vibratory gyroscopes," *IEEE Sensors*, pp. 531-536, 2005
- [Shu02] P.J. Shull, "Non destructive evaluation: Theory, techniques and applications," *CRC Press*, 2002.
- [Sio02] I. de Sio, L. Castellano, M. Calandra, and C. Del Vecchio-Blanco, "Subcutaneous needle-tract seeding after fine needle aspiration biopsy of pancreatic liver metastasis," *European Journal of Ultrasound*, 15, pp.65-68, 2002.
- [Ski98] M.G. Skinner, M.N. Iiuzuka, M.C. Kolios, and M.D. Sherar, "A theoretical comparison of energy sources - microwave, ultrasound and laser - for interstitial thermal therapy," *Physics in Medicine and Biology*, 43, pp. 3535-3547, 1998.
- [Smi96] T.P. Smith, V.G. McDermott, D.M. Ayoub, P.V. Suhocki, and D.J. Stackhouse, "Percutaneous transhepatic liver biopsy with tract embolization," *Radiology*, 198, pp. 769-774, 1996.
- [Sug91] S. Sugano, Y. Sumino, T. Hatori, H. Mizugami, T. Kawafune, and T. Abei, "Incidence of ultrasound-detected intrahepatic hematomas due to Tru-cut needle liver biopsy," *Digestive diseases and Sciences*, 36, pp. 1229-1233, 1991.
- [Suh97] J.W. Suh, S.F. Glander, R.B. Darling, C.W. Storment, and G.T.A. Kovacs, "Organic thermal and electrostatic ciliary microactuator array for object manipulation," *Sensors and Actuators A*, 58, pp. 51-60, 1997.
- [Sup00] *MD1213DB1 datasheet*, Supertex Inc., Sunnyvale, CA.
- [Tab85] O. Tabata, H. Inagaki, I. Igarashi, and T. Kitano, "Fast response silicon flow sensor with a thermal isolation structure," *Proceedings of the 5th Sensor Symposium, Japan*, pp. 207-211, 1985.
- [Tai88] Y.C. Tai and R.S. Muller, "Lightly doped polysilicon bridge as a flow meter," *Sensors and Actuators A*, 15, pp. 63-75, 1988.
- [Tak00] R. Takamori, L.L. Wong, C. Dang, and L. Wong, "Needle tract implantation from hepatocellular cancer: is needle biopsy of the liver always necessary?," *Liver Transplantation*, 6, pp. 67-72, 2000.

- [Tak04] S. Takeuchi and I. Shimoyama, "A radio-telemetry system with a shape memory alloy microelectrode for neural recording of freely moving insects," *IEEE Transaction on Biomedical Engineering*, 51, pp. 133-137, 2004.
- [Tan86] J. Tanaka, A. Jinda, H. Tabuchi, N. Tanaka, H. Furubayashi, Y. Inami, and M. Hijikigawa, "A micro flow sensor with a substrate having a low thermal conductivity," *Proceedings of the 6th Sensor Symposium*, Japan, pp. 125-129, 1986.
- [Tex01] Texas Instruments application report, "Analysis of Sallen-Key Architectures".
- [Tia03] W.C. Tian and S.W. Pang, "Thick and thermally isolated Si microheaters for microfabricated preconcentrators," *Journal of Vacuum Science and Technology B*, 12, pp. 274-279, 2003.
- [Tie97] N.C. Tien, "Silicon micromachined thermal sensors and actuators," *Microscale Thermophysical Engineering*, 1, pp. 275-292, 1997.
- [Tor02] M. Torndahl, M. Almgvist, L. Wallman, H. W. Persson, and K. Lindstorm, "Characterisation and comparison of a CMUT versus a piezoelectric transducer for air applications," *Proceedings of IEEE Ultrasonics Symposium*, 2, pp. 1023-1026, 2002.
- [Tsu85] J. Tsujino, T. Ueoka, and K. Kenmotsu, "Recent advance in ultrasonic welding of metal and plastics," *IEEE Ultrasonics Symposium Proceedings*, pp. 557-562, 1985
- [Tyr02] P.D. Tyreus and C.J. Diederich, "Theoretical model of internally cooled interstitial ultrasound applicators for thermal therapy," *Physics in Medicine and Biology*, 47, pp. 490-498, 2002.
- [Uch06] K. Uchino, J.H. Zheng, Y.H. Chen, X.H. Du, J. Ryu, Y. Gao, S. Ural, and S. Priya, "Loss mechanisms and high power piezoelectrics," *Journal of Material Science*, 41, pp. 217-228, 2006
- [Ume06] Y. Umehara and M.K. Kurosawa, "A micro ultrasonic scalpel using hydrothermal PZT thin film," *15th IEEE International Symposium on the Applications of Ferroelectrics*, pp. 340-343, 2006.
- [Vae97] S. Vaezy, R. Martin, U. Schmiedl, M. Caps, S. Taylor, K. Beach, S. Carter, P. Kaczkowski, G. Keilman, S. Helton, W. Chandler, P. Mourad, M. Rice, R. Roy, and L. Crum, "Liver hemostasis using high intensity focused ultrasound," *Ultrasound in Medicine and Biology*, 23, pp. 1413-1420, 1997.
- [Val95] S. Valette, "Micro-optics, a key technology in the race to Microsystems," *Journal of Micromechanics and Microengineering*, 5, pp. 74-76, 1995.

- [Ver01] J.L. Vernet, W. Steichen, R. Lardat, O. Garcia, and J.F. Gelly, "PMUTs design optimization for medical probes applications," *Proceedings of IEEE Ultrasonic Symposium*, pp. 899-902, 2001.
- [Ver98] P. Verardi, F. Craciun, M. Dinescu, and C. Gerardi, "Epitaxial piezoelectric PZT thin films obtained by pulsed laser deposition," *Thin Solid Films*, 318, pp. 265-269, 1998.
- [Vis01] K. Visvanathan, Y.B. Gianchandani, "Ultrasonic Microheaters Using Piezo-Ceramics for Cauterization and Other Applications," *IEEE International Conference on Solid-State Sensors, Actuators, and Microsystems (Transducers)*, Denver, Colorado, June 2009, pp. 2421-2424
- [Vis02] K. Visvanathan, N.K. Gupta, M.M. Maharbiz, Y.B. Gianchandani, "Flight Initiation and Directional Control of Beetles by Microthermal Stimulation," *Solid-State Sensors and Actuators and Microsystems Workshop (Hilton Head '08)*, Hilton Head Island, South Carolina, June 2008, 126-129
- [Vis03] K. Visvanathan, N.K. Gupta, M.M. Maharbiz, Y.B. Gianchandani, "Control of Locomotion in Ambulatory and Airborne Insects Using Implanted Thermal Microstimulators," *IEEE International Conference on Solid-State Sensors, Actuators, and Microsystems (Transducers)*, Denver, Colorado, June 2009, pp. 1987-1990
- [Vis04] K. Visvanathan, Y.B. Gianchandani, "Biopsy Needle Tract Cauterization Using an Embedded Array of Piezoceramic Microheaters," *IEEE/ASME International Conference on Micro Electro Mechanical Systems (MEMS 10)*, Hong Kong, Jan. 2010, pp. 987-1000
- [Vis05] K. Visvanathan, T. Li, Y.B. Gianchandani, "In Situ Monitoring of Cauterization with a Biopsy Needle Using Impedance Characteristics of Embedded Piezothermal Elements," *International Conference on Miniaturized Systems for Chemistry and Life Sciences (MicroTAS 2010)*, Groningen, The Netherlands, October 3-7 2010, pp. 1478-1480
- [Vis06] K. Visvanathan, T. Li and Y. B. Gianchandani, "3D-SOULE: A fabrication process for large scale integration and micromachining of spherical structures," *24th IEEE International Conference on Micro Electro Mechanical Systems, Cancun*, January 2011.
- [Vol07] F. Volklein and A. Meier, "Microstructured vacuum gauges and their future perspectives," *Vacuum*, 82, pp. 420-430, 2007.
- [Wan00] L.P. Wang, R. Wolf, Q. Zhou, S. Trolier-McKinstry, and R. J. Davis, "Wet-etch patterning of lead zirconate titanate (PZT) thick films for microelectromechanical systems (MEMS) applications," *Materials Science of MEMS Devices III. Symposium*, Boston, 2000.

- [Wan99] S. Wang, X. Li, K. Wakabayashi, and M. Esashi, "Deep reactive ion etching of lead zirconate titanate using sulfur hexafluoride gas," *Journal of American Ceramic Society*, 82, pp. 1339-1341, 1999.
- [Wat84] H.A. Waterman, "Measurement of the dynamic shear modulus of surface layers," *Journal of Colloid and Interface Science*, 101, pp. 377-383, 1984
- [Web01] http://en.wikipedia.org/wiki/Laser_ultrasonics, as referenced on 11th August 2009.
- [Web02] <http://www.ndt-ed.org/EducationResources/CommunityCollege/Ultrasonics/Equipment/Trans/emats.htm>, as referenced on 11th August 2009
- [Web03] <http://www.ndt-ed.org/EducationResources/CommunityCollege/Ultrasonics/Equipment/Trans/piezotransducers.htm>, as referenced on 11th August 2009.
- [Web05] <http://www.morganelectroceramics.com/pdfs/tp226.pdf>, as referenced on 23rd August 2009.
- [Wei08] J. Wei, T.C. Duc, G.K. Lau, and P.M. Sarro, "Novel electrothermal bimorph actuator for large out-of-plane displacement and force," *IEEE 21st International Conference on Micro Electro Mechanical Systems*, pp.46-49, 2008.
- [Wen00] H. Wensink, J.W. Berenschot, H.V. Jansen, and M.C. Elwenspoek, "High resolution powder blast micromachining," *IEEE International Conference on Micro Electro Mechanical Systems (MEMS)*, pp. 769-774, 2000.
- [Wen02] H. Wensink and M.C. Elwenspoek, "Reduction of sidewall inclination and blast lag of powder blasted channels," *Sensors and Actuators A*, 102, pp. 157-164, 2002.
- [Wis81] K.D. Wise, M.G. Robinson, and W.J. Hillegas, "Solid-state process to produce hemispherical components for internal fusion targets," *Journal of Vacuum Science Technology*, 16, pp. 1179-1182, 1981.
- [Wu06] J.Z. Wu, R.G. Dong, and D.E. Welcome, "Analysis of the point mechanical impedance of fingerpad in vibration," *Medical Engineering and Physics*, 28, pp. 816-826, 2006.
- [Yag97] D.D. Yager and H.G. Spangler, "Behavioral response to ultrasound by the tiger beetle *Cicindela marutha* dow combines aerodynamic changes and sound production," *The Journal of Experimental Biology*, 200, pp. 649-659, 1997.
- [Yan00] Z. Yang, H. Goto, M. Matsumoto, and R. Maeda, "Active micromixer for microfluidic systems using lead-zirconate titanate (PZT)-generated ultrasonic vibration," *Electrophoresis*, 21, pp. 116-119, 2000

- [Yu01] H.G. Yu, R. Wolf, K. Deng, L. Zhou, S. Tadigadapas, and S.T. McKinstry, "Fabrication and performance of d33-mode lead-zirconate titanate (PZT) MEMS accelerometers, " *MEMS Components and Applications for Industry, Automobiles, Aerospace, and Communication. Conference*, San Francisco CA , pp. 130-137, 2001.
- [Za103] M. Zalalutdinov, K.L. Aubin, R.B. Reichenbach, A.T. Zehnder, B. Houston, J.M. Parpia, and H.G. Craighead, "Shell type micromechanical actuator and resonator," *Applied Physics Letters*, 83, pp. 3815-3817, 2003.
- [Zha06] F.T. Zhang, Z. Tang, J. Yu, and R.C. Jin, "A micro-Pirani vacuum gauge based on micro-hotplate technology," *Sensors and Actuators A*, 126, pp. 300-305, 2006.
- [Zhe96] J. Zheng, S. Takahashi, S. Yoshikawa, and K. Uchino, "Heat generation in multilayer piezoelectric actuators," *Journal of American Ceramics Society*, 79, pp. 3193-3198, 1996.
- [Zho95] S.W. Zhou and C.A. Rogers, "Heat generation, temperature, and thermal stress of structurally integrated piezo-actuators," *Journal of Intelligent Material Systems and Structures*, 6, pp. 372-379, 1995.
- [Zim95] J.E. Zimmer, K. Hynynen, D.S. He, and F. Marcus, "The feasibility of using ultrasound for cardiac ablation," *IEEE Transaction on Biomedical Engineering*, 42, pp. 891-897, 1995.
- [Zin92] M. Zins, V. Vilgrain, S. Gayno, Y. Rolland, L. Arrive, M.H. Denninger, M.P. Vullierme, D. Najmark, Y. Menu, and H. Nahum, "US-guided percutaneous liver biopsy with plugging of the needle track: a prospective study in 72 high-risk patients," *Radiology*, 184, pp. 841-843, 1992